Automated Extraction of Road Information from Mobile Laser Scanning Data

by

Haiyan Guan

A thesis
presented to the University of Waterloo
in fulfillment of the
thesis requirement for the degree of
Doctor of Philosophy
in
Geography

Waterloo, Ontario, Canada, 2013

AUTHOR'S DECLARATION

I hereby declare that I am the sole author of this thesis. This is a true copy of the thesis, including any required anal revisions, as accepted by my examiners.

I understand that my thesis may be made electronically available to the public.

Abstract

Effective planning and management of transportation infrastructure requires adequate geospatial data. Existing geospatial data acquisition techniques based on conventional route surveys are very time consuming, labor intensive, and costly. Mobile laser scanning (MLS) technology enables a rapid collection of enormous volumes of highly dense, irregularly distributed, accurate geo-referenced point cloud data in the format of three-dimensional (3D) point clouds. Today, more and more commercial MLS systems are available for transportation applications. However, many transportation engineers have neither interest in the 3D point cloud data nor know how to transform such data into their computer-aided model (CAD) formatted geometric road information. Therefore, automated methods and software tools for rapid and accurate extraction of 2D/3D road information from the MLS data are urgently needed.

This doctoral dissertation deals with the development and implementation aspects of a novel strategy for the automated extraction of road information from the MLS data. The main features of this strategy include: (1) the extraction of road surfaces from large volumes of MLS point clouds, (2) the generation of 2D geo-referenced feature (GRF) images from the road-surface data, (3) the exploration of point density and intensity of MLS data for road-marking extraction, and (4) the extension of tensor voting (TV) for curvilinear pavement crack extraction. In accordance with this strategy, a RoadModeler prototype with three computerized algorithms was developed. They are: (1) road-surface extraction, (2) road-marking extraction, and (3) pavement-crack extraction. Four main contributions of this development can be summarized as follows.

Firstly, a curb-based approach to road surface extraction with assistance of the vehicle's trajectory is proposed and implemented. The vehicle's trajectory and the

function of curbs that separate road surfaces from sidewalks are used to efficiently separate road-surface points from large volume of MLS data. The accuracy of extracted road surfaces is validated with manually selected reference points.

Secondly, the extracted road enables accurate detection of road markings and cracks for transportation-related applications in road traffic safety. To further improve computational efficiency, the extracted 3D road data are converted into 2D image data, termed as a GRF image. The GRF image of the extracted road enables an automated road-marking extraction algorithm and an automated crack detection algorithm, respectively.

Thirdly, the automated road-marking extraction algorithm applies a point-density-dependent, multi-thresholding segmentation to the GRF image to overcome unevenly distributed intensity caused by the scanning range, the incidence angle, and the surface characteristics of an illuminated object. The morphological operation is then implemented to deal with the presence of noise and incompleteness of the extracted road markings.

Fourthly, the automated crack extraction algorithm applies an iterative tensor voting (ITV) algorithm to the GRF image for crack enhancement. The tensor voting, a perceptual organization method that is capable of extracting curvilinear structures from the noisy and corrupted background, is explored and extended into the field of crack detection.

The successful development of three algorithms suggests that the RoadModeler strategy offers a solution to the automated extraction of road information from the MLS data. Recommendations are given for future research and development to be conducted to ensure that this progress goes beyond the prototype stage and towards everyday use.

Acknowledgements

First and foremost, I would like to express the greatest gratitude to my supervisor, Professor Dr. Jonathan Li, for providing me this opportunity and keeping a faith from beginning to end of this process. Without his continuous support and encouragement, positive remarks, and intellectual guidance, it was difficult to complete this thesis. I feel very fortunate having the chance to work with him in the past three years. Many opportunities he gave me to practice have stimulated many of my interests and enabled me to gain more experiences in my research field.

Special thanks are given to my co-supervisor, Professor Dr. Michael Chapman, Ryerson University, for his financial support and his constructive suggestions.

I would like to thank the PhD Thesis Examining Committee, which includes Dr. Derek Lichti (external examiner), Professor and Head of the Department of Geomatics Engineering, University of Calagary; Dr. Liping Fu (internal/external examiner), Professor of the Department of Civil and Environmental Engineering, University of Waterloo; Dr. Richard Kelly (thesis committee member), Professor and Associate Dean of Research of the Faculty of Environment, and Dr. Su-Yin Tan (thesis committee member), Department of Geography and Environmental Management, University of Waterloo. Their useful comments and suggestions increase the readability of this thesis and make a much better way to present my research findings.

I was fortunate to travel this road with many other graduate students, and needless to say, it is a road best shared. I wish to acknowledge the important role their encouragement in the completion of this thesis. Many thanks go to Que Ren, and her husband for sharing their time and helping me go through the first year in Waterloo. Sincere thanks also go to Jiao Jin, Qing Xiang, Linlin Xu, Yuanming Shu, Aijuan Chen for creating a friendly working environment. A special thank to Weifang Yang and Haowen Yan, for providing suggestions and supports. I also deeply appreciate the past and present members of the

Haiyan Guan

November 29, 2013

Table of Contents

List of Figures

List of Tables

List of Abbreviation

ALS	Airborne laser scanning
Boresight	A very small angular error in vertical alignment between the IMU system and the sensor
Curb	A nearly vertical surface is served as a boundary between road and sidewalk or green space
DEM	Digital elevation model
DMI	Distance measurement indicator
DOT	Department of Transportation
Geo-referencing	The association of ground coordinates for objects
GNSS	Global navigation satellite system
GPS	Global positioning system
GRF	Geo-referenced feature
IDW	Inverse distance weighted
IMU	Inertial measurement unit
Intensity	Strength of reflectivity of returning pulse, recorded as a numerical value and converted to 8-bit image
ITV	Iterative tensor voting
LAS	Lidar native file format
Lever-arm	A distance offset between two sensors
LiDAR	Light detection and ranging
MLS	Mobile laser scanning
MLS data	Point clouds collected by a MLS system
MMS	Mobile mapping system

MMT	Mobile mapping technology
MTLS	Mobile terrestrial laser scanning
MTO	Ministry of Transportation of Ontario
Point cloud	XYZ points captured with lidar sensor
PRR	Pulse repetition rate
RMSE	Root mean square error
RTK	Real time kinemic
SM	Score measure
SNR	Signal-to-noise ratio
STLS	Stationary terrestrial laser scanning
Tensor voting	An algorithm for perceptual grouping
TIN	Triangulated irregular network
TLS	Terrestrial laser scanning
Trajectory	The path of the vehicle along the road
WID	Weighted intensity difference

Chapter 1 Introduction

1.1 Background

Road transportation plays a vital role in people's daily lives in all countries because it brings people together for business or pleasure by connecting small and large cities, urban and rural communities, as well as connecting a country with its neighbors to enable the safe movement of goods, people, and services. To safely keep people on the move, transportation departments in cities or countries have to periodically perform road surveys. The documentation of road infrastructure includes both road surface geometry (e.g., lane width, number of lanes, longitudinal slopes, and transverse slopes) and road environment (e.g., road markings, pavement cracks, street signs, trees, vegetation, and traffic light poles). The surveyed data are used not only for transportation departments to maintain, rehabilitate, and reconstruct the current roadways and bridges, and to manage traffic and parking infrastructure, but also for administration to assess policies and practices affecting roadways. However, transportation-related road features are manually collected by involving an engineer annotating a digital map or manually classified based on spatially referenced videos (Kumar et al., 2010). These methods for inspecting transportation-related road features on a large scale are very time consuming, labor intensive, and costly.

Transportation infrastructure, an important component of land use, is constantly evolving with social and economic developments. The road network is a large part of transportation infrastructure in urban areas, making a critical contribution to population growth and increasing mobility of our society. A transportation agency needs road geo-

spatial information for a variety of applications, such as regular road maintenance (e.g., crack sealing, patching, edge repairing, surface dressing, and spot rehabilitating), driver-assistance systems, and road safety analysis. The significance of road information for planning, building and maintaining road infrastructure has stimulated an increase in producers of specialized technologies and software for road asset inventory (McCarthy et al., 2007).

The recent two decades have witnessed a technically transformative change for transportation agencies over the world. The change is from 2D paper-based world to 3D digital technology. Compared to 2D road information, semantically-tagged 3D models of urban road environments are crucial to understand the complete structure of a city and provide contextual cues for recognizing small street-scene objects such as overpasses, bridges, traffic signs, and even roadside high power lines. With proper practices, 3D road models can link a variety of other data such as traffic or crash data for transportation management. Traditionally, to collect 3D road data, a design project needs lane closures, leading to an enormous safety risk for surveyors working along the road and a high degree of low production rates. Efficient and inexpensive techniques for data acquisition in the field of remote sensing have been gaining popularity in the extraction of roads and street-scene objects.

MLS, a widely used technology since 2003 when the first commercial MLS system was developed, has attracted much attention to mainly transportation-related surveys (Jacobs, 2005; Toth, 2009). It is a data revolution. With a MLS system, mobile mapping crew can drive on a highway, rural road, and railroad, by a river or lake, or along a shoreline. Along the way, the system captures trees, bridges, streetlights,

2

buildings, power lines, other street-scene small objects (e.g., pavement cracks, road markings), virtually anything visible to the eyes in 3D. The collected data are a totally immersive 3D view of objects and surroundings (Rybka, 2011).

Today's major trend in mapping and GIS is an increasing demand for not only accuracy of geospatial data but efficiency and low cost. MLS systems can meet this demand and provide the end results with increased productivity (Hutton, 2008). Moreover, MLS is a much safer mapping technique than traditional highway survey methods, where surveyors wearing orange vests measure the land boundaries and understand the terrain via total stations, TMLS, and so on, as well as the requirement of extensive traffic management or road closures.

Given MLS advantages including improved safety, faster turnaround, and more complete and accurate survey data, a growing number of transportation agencies have considered MLS for road inventory and outlined guidelines for transportation applications. For example, according to the latest figures published by the U.S. Bureau of Statistics in 2010, the U.S. national transportation network consists of 601,392 highway bridges and overpasses intermittently placed within 46,934 miles of interstate highway and 116,837 miles of national highway system roads. To maintain and manage the national transportation network, a few states Department of Transportation (DOT), such as Tennessee DOT, Hawaii DOT, Nevada DOT, Ohio DOT, and Texas DOT, have contracted with MLS service providers for road asset management.

Note that MLS certainly will not replace more conventional methods of topographic data collection. The MLS data, in most cases, may need to be supplemented by data collected from the existing methods such as conventional surveying, GPS,

photogrammetry, and ALS (Gordon, 2010). MLS, integrated a navigation solution, laser scanners, and a number of high-resolution cameras with even more powerful computer systems, is still in its infancy and has only been commercially available for five years (Stauth and Olsen, 2013*)*. Thus, studies on MLS as a reliable and cost-effective alternative, is worthwhile for carrying out road inspections along the route corridor.

However, the data collected by MLS systems are very large and require upgrading not only the entire computing infrastructure (software, workstations, servers, data storage, and network backbone) but also data post-processing packages for road-information extraction. Manually processing the significant volumes of MLS data for road-information extraction are very time consuming. Current software packages are incapable of modelling and utilizing point clouds for design. Thus, advanced sensor technologies and current data-processing situations provide the underlying motivations for this thesis to research automated road-information extraction algorithms.

1.2 Motivations

Data post-processing is the key to a complete solution for the end-users. Hardware manufactures continue to build advanced MLS systems. For example, RIEGL VMX-250 system that can collect 0.5 million points per second was developed into the current RIEGL VMX-450 system that collects 1.1 million points per second. Data post-processing software capabilities need to catch up with the hardware development for transforming the significant volumes of data into the deliverables, such as DEM and contour maps. However, managing such massive points has presented a new challenge to software industries.

Although post-processing methods for laser scanning data, particularly ALS data, have made great progress a few short years ago, no reliable, robust, and stable theoretical frames exist for MLS data processing, and most algorithms or methods still stay at the stage of research and development. Several well-known companies provide companion software packages along with their laser scanning systems, such as Riegl's Ri-SCAN PRO for TLS data and Ri-PROCESS for MLS data. However, these packages are focusing on some fundamental operations, such as data control, calibration, adjustment, registration, and visualization. As for road-information extraction and 3D road modelling, most companies allow exporting multiple file format types or providing an interface to further post-processing tools to execute data classification, triangulation or 3D modelling by third-party software packages.

Currently, the advanced third-party point-cloud post-processing software includes Leica Cyclone®, InnovMetric PolyWorks®, GeoCue software suite, TerraSolid software suite, PHOCAD PHIDIAS®, Bentley Pointools, and Virtual Geomatics software suite (Yen et al., 2011). Most third-party software packages can deal with only small volumes of 3D points. The Terrasolid® software suite that includes TerraScan, TerraModeler, TerraMatch, TerraPhoto, TerraControl, and TerraOffice modules, is suited for processing large volumes of points in a reasonable time based on the platform of Microsation®. However, the Terrasolid® software suite was originally developed for ALS data, whose data size for each strip probably is at megabyte levels. The Terrasolid® software suite is sometimes limited to MLS data at gigabyte or terabyte levels.

Academic research on road features using MLS data is now motivated by the increasing demands for road network update and 3D city modelling. Most current studies

on road extraction applied geometrical models such as RANSAC, Hough Transform, and Least Square Linear fitting to MLS data. However, these mathematical estimation algorithms are limited to large volumes of MLS data because of their intensive computation. Some studies extracted road points in an object-classification way, where both road and data characteristics such as road width, intensity information, were used. These algorithms are efficient, but not very reliable because of occlusion. Extensive work is required for radiometric calibration.

The extraction of road marking and crack has been widely researched on digital images. However, precise geometrical information is limited by the following environmental factors: (1) road surface materials, such as light pavement, dark pavement, or a combination of different pavements, (2) weather conditions and time of day that can have a great impact on the visibility of road surfaces, and (3) complex shadowing from trees and moving vehicles.

Given the rapid development of MLS hardware and the urgent need for software tools that can handle huge volumes of 3D point clouds, this research aims to develop an automated road information extraction system by taking advantage of the MLS data.

1.3 Objectives of the Study

The specific objectives of this thesis can be described as follows:

The first objective is to develop an automated algorithm for extracting road edges from MLS data. Separating road points from off-road points is a difficult task for gigabyte-level MLS data. The purpose of this study is to make use of the vehicle trajectory for partitioning MLS data and detect curbs for extracting road edges without any data management structures being involved.

The second objective is to develop an automated algorithm for identifying road markings. Although road markings are painted by high-reflective materials, the magnitudes of the reflected data highly depend on the scanning distance from a scanner to illuminated objects, the incident angle of a laser pulse, and the material properties of road surfaces. The purpose of this study is to explore point density to segment road markings and further extract road markings via a morphological operation.

The third objective is to explore the potential of MLS data for pavement-crack extraction. To simplify post-processing procedures, the classified road points are interpolated into 2D GRF images similar to range images for ALS. The purpose of this study is to explore the applicability of tensor voting for pavement-crack extraction from noisy 2D GRF images.

1.4 Structure of the Thesis

The thesis consists the following six chapters. Chapter 2 reviews fundamental knowledge of the MLS technology and a variety of previous studies on the extraction of road surfaces, road markings, and pavement cracks using MLS data. Chapter 3 explains the designed method framework of road-information extraction, describes RIEGL VMX-450 system, analyzes the collected MLS data, and presents the study area. Chapters 4, 5, and 6 detail the road-information extraction algorithms developed for the automated extraction of road surfaces, road markings, and pavement cracks, respectively. Chapter 7 concludes this research with a summary of four contributions and details future research directions.

Chapter 2 Literature Review

2.1 Description of MLS

2.1.1 Introduction

MMS refers to a means of collecting 3D geospatial data using mapping sensors that are mounted on a land-based vehicle for corridor mapping (Schwarz and El-Sheimy, 2007; GIM 2013; Lemmens, 2011). In terms of sensors, MMS is normally categorized as: image-based and laser-based.

Image-based MMS has a major impact on conventional transportation surveying and mapping, such as modelling and estimation of road boundaries in road safety assistance (Tao and Li, 2007; Dickmanns and Mysliwetz, 1992; Bertozzi, et al., 1997; Pomerleau and Jochem, 1996). This significant impact is because images contain rich color and texture information which benefits road extraction. Commercial image-based road extraction systems have been widely available (Liu et al., 2013). However, image-based MMSs are incapable of dealing with situations where road features such as lane markings are missing / ambiguous and visibly restricted due to weather conditions (Tsogas et al., 2011). The technology of 3D laser scanning has emerged and further been fuelled to a wide variety of transportation applications, such as model-based road design and automated machine guidance.

Laser scanning systems that use a laser beam to scan a visible surface and record the beam travelling time and the reflected energy from the surface to obtain its geometry and intensity information, have been used for a broad spectrum of applications, such as route planning and preliminary highway design (Road Talk, 2013). Compared to

photogrammetry and field surveys, laser scanners capture very highly accurate 3D point clouds with a high point density in a relatively short amount of time (Haala et al., 2008; Chehata et al., 2009; Ussyshkin, 2009). Note that MLS systems emerged from 2003 can collect topographic data more accurately with a higher resolution than the data collected by their counterparts, such as airborne laser scanning systems. More terms, such as TMLS, land-based MLS, or mobile LiDAR, are interchangeably used in the field of laser scanning. The feasibility of MLS for transportation-related road surveys continues to be proven in safety, cost, efficiency, and data confidence. Besides collecting explicit highly-accurate elevation information, MLS systems also provide other implicit information, such as intensity, vehicle trajectory, scanning patterns, and pulse information, all of which contribute to road-information extraction.

Compared to traditional survey methods, such as conventional surveying (using total stations), global positioning system (GPS), and photogrammetry, MLS offers many advantages: high accuracy, high point density, rapid data collection, and unprecedented details (Babic et al., 2012). For example, for a Trimble MX-8, the data accuracy is within 4-5 cm in planimetric and within 2-3 cm in elevation (Guan et al., 2013). The Trimble MX-8 MLS system integrates two Riegl VQ-250 laser scanners that can produce 600,000 points per second. As a result, the system can collect data up to 35 Gigabytes within twenty minutes, plus images from four high-resolution cameras, at the speed of around 30~50 km/h. Therefore, MLS is a more feasible 3D measurement technology for large-scale mapping projects than the legacy methods (Schrock, 2013). Specifically speaking, a 10-km-long highway would have taken at least 20 nights to survey and a week to process the resultant measurements by a traditional highway survey method, while the highway,

9

would take, from start to finish, less than a week using a MLS system, (LiDAR News, 2013).

2.1.2 System Components

Most MLS systems are composed of four major components: (1) laser scanner(s), (2) camera(s), (3) a navigation system that integrates a Global Navigation Satellite System (GNSS), an Inertial Measurement Unit (IMU), and a wheel-mounted Distance Measurement Indicator (DMI), and (4) a control system that synchronizes all sensors and manages data storages and communication.

(1) A navigation solution- an integration of GNSS, IMU, and DMI.

Rather than one of these components alone, an integration of an IMU, more than one GNSS antenna, and a DMI allows exploiting the complementary nature of those sensors. GNSS receivers provide three primary observations: time, position, and velocity (speed and direction) measurements. Position and velocity are used for logging to computers and IMU.

Although GNSS receivers can provide highly accurate positional information in an open environment, it suffers when satellite signals are blocked by high-rise buildings, vegetation, tunnels, and other obstacles. On the other hand, IMU provides attitude information of the vehicle (roll, pitch, and heading), and does not require satellite signals to sense 3-axis accelerations and 3-axis angular rotations; however, the accuracy of position and orientation degrades with the time. Thus, GNSS and IMU are integrated to provide precisely positioning information. GNSS positions are augmented by IMU in periods of poor satellite conditions, while GNSS provides updated positioning information to IMU. Compared to ALS and TLS systems, MLS systems have DMIs that

can constrain the error drift, especially during vehicle stoppages in areas of intermittent GNSS coverage.

DMI is placed on one of the vehicle wheels to measure tire rotation, directly estimating a travelled distance. DMI is referred to as the Instrumented Wheel. Its output pulses represent fractional revolutions of the Instrumented Wheel. These pulses are converted into incremental distance, providing a measure of the distance travelled by the vehicle. The measure, termed as DMI scale factor, can be calculated by the following two formulas: (1) Pulse and Direction DMI (Type 1): $S = n/d\pi$, and (2) Quadrature DMI (Type 2): $S = 4n/d\pi$. Where, n is the number of DMI pulses per revolution, and d is the Instrumented Wheel diameter in metres. The number of DMI pulses per revolution is typically stamped on a DMI nameplate. DMI usually supplements GNSS and IMU with additional positioning information. Wheel rotation data constrain drift, especially during vehicle stoppages in areas of intermittent GNSS coverage.

A Kalman Filter compares the inertial solution with the corresponding data from the primary GNSS receiver, GPS Azimuth Measurement Subsystem (GAMS), and DMI, estimating inertial navigation errors. A tightly coupled ambiguity resolution algorithm is in use when real-time GNSS corrections data are available. The navigation software then adjusts the inertial navigation solution by the estimated navigation errors. This process of inertial navigation, navigation error estimation, and error correction forms a closed error regulation loop that requires the inertial navigation data to be consistent with the aiding sensor data (Petri, 2010; Zarchan and Musoff, 2009). When Real Time Kinematic (RTK) corrections are provided to the system, errors are regulated to centimetre-level accuracy, while velocity and attitude errors are controlled to similarly small values. Based on aided

inertial technology, the system provides continuous and accurate vehicle positional and orientation information when it runs through areas of poor or no satellite service, such as urban canyons, full tree canopy, tunnels, and bridges.

In order to obtain highly accurate GNSS data, approximately 5-min of static GNSS logging at the beginning and end of each survey is required for calculation of the Best Estimate Trajectory (BET) of the vehicle. The trajectory is then used to transform laser scanning data into geo-referenced point clouds. Thus, the main function of the navigation solution is to provide real-time navigation data, including position (latitude, longitude, and altitude); geographic velocity - North, East and Down (NED); attitude (roll, pitch, and heading); acceleration (xyz in reference frame); angular rate; distance travelled; and RMSE measures (position, velocity, attitude, angular rates). Those data can be also applied to other user-supplied sensors (e.g., cameras).

(2) Digital camera(s)

Most MLS systems incorporate camera(s) to provide ancillary information. For example, for visualization, points collected by laser scanners can be colored by true-color information in the real world. Different MLS systems configure different number of digital cameras in many deployed patterns. The specific deployment of cameras is customized by users and projects. This additional color information contributes to road-information extraction because it provides a great level of details of features.

(3) Laser scanner(s)

Similar to digital cameras, the number and the arrangement pattern of laser scanners vary with different MLS systems. Laser scanners emit continuous waves/ pulses at a fixed or user-defined angular increment to measure the ranges to objects. In current

MLS systems, two techniques are mainly used for range measurements: time-of-flight and phase shift (Lichti, 2010). Time-of-flight (TOF) scanners send a short laser pulse to the illuminated target, and the time difference between the emitted and received pulses determines the range. The time-of-flight mode is commonly used for the majority of current commercially-available MLS systems. In contrast, phase shift based laser scanners use phase difference between the emitted and received backscattered signals of an amplitude modulated continuous wave (AMCW) to determine the range. Phase shift laser scanners are more accurate, but their measurement range is relatively shorter, smaller than ~ 100 m (Petrie and Toth, 2008; Beraldin et al., 2010).

Moreover, there are two kinds of modes in terms of scanning head:

(a) Fixed scanning head laser scanners: some MLS systems configure a number of fixed scanning head laser scanners with internal rotating mirrors. Those fixed scanning head laser scanners are normally used in TLS. In order to obtain 360° scanning coverage, multiple laser scanners are typically deployed into a MLS system. For example, Topcon IP-s2 compact+ system consists of five SICK LMS 291 laser sensors, each of which has 180° horizontal field of view (FOV) and 90° vertical FOV.

(b) Rotating scanning head laser scanners: some MLS systems such as Trimble MX-8, RIEGL VMX-250 and VMX-450, have a fixed number of rotating scanning head laser scanners which are deployed slightly tilted. For example, in Trimble MX-8 system, two RIEGL VQ-250 laser scanners are symmetrically configured on the left and right sides, pointing toward the rear of the vehicle at an angle heading of approximately 145°. Such a configuration is called "Butterfly" or "X" pattern. Each RIEGL VQ-250 scanner generates its own 360° "full circle" profile scan owing to the motorized mirror scanning

mechanism, as shown in Figure 2.1(a). Thus, the scanned data of two scanners form a slant grid-like pattern, as shown in Figure 2.1(b).

<table>
<tr><td>(a)</td><td>(b)</td></tr>
</table>
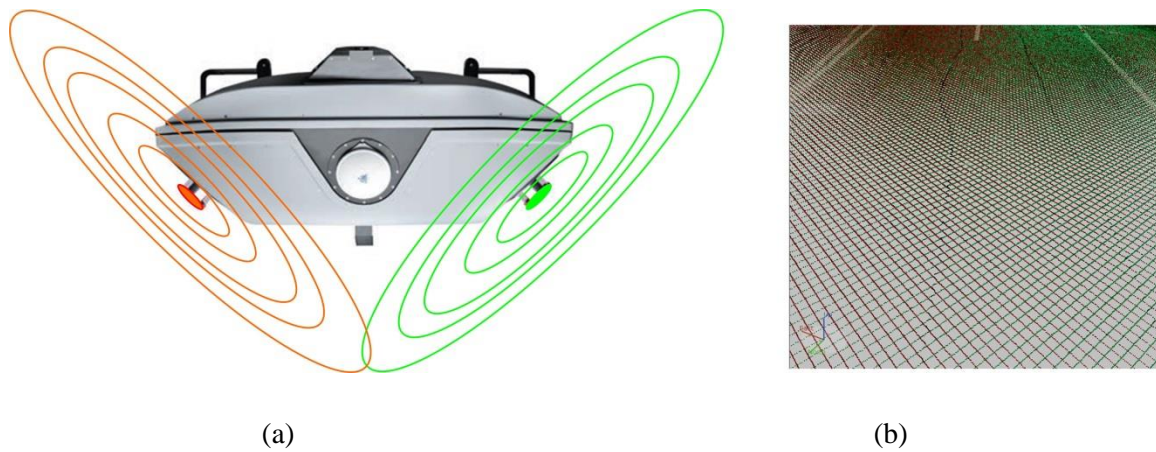
Figure 2.1: An example of scanning pattern of a mobile laser scanning: (a) an illustration of two rotating scanning head laser scanners, and (b) the scanned data.

The quality of laser scanners is determined by the following factors: eye safety, accuracy, field-of-view, resolution, and scan rate (Iavarone, 2007). Laser scanners use Class 1 eye safety rating, that is, the beam is invisible and safe to the human eyes in both aided and unaided conditions. The accuracy of MLS systems directly determines the accuracy of final deliverable products. A field-of-view dictates the extent of area that can be covered in a single pass of the collection vehicle. The resolution of MLS data depends on several factors, including vehicle speed, laser mirror scanning speed, beam width, and system measurement rate.

(4) A control unit

A control unit is a synchronizer that integrates all data from sensors such as cameras, laser scanners, and the navigation solution.

(5) Rigid platform

The set of rigid platform is a device firmly attaching laser scanners, digital cameras, GNSS receivers, IMU, and other ancillary devices into a compact unit. The offsets between each sensor have to be strictly measured to remain stable for MLS systems. Usually, these offset parameters are provided by manufacturers, no concerns of users are needed.

2.1.3 Commercial MLS Systems

More recently, a number of MLS systems have been developed and appeared in the market because laser scanning-related component technologies (e.g., scanning, imaging, and positioning devices) continued to advance. This section covers only several main MLS suppliers that integrate major components and offer a complete solution for sale to users. Table 2.1 lists the current commercially-available MLS systems, and Figure 2.2 shows their configurations. The MLS system suppliers list in the table have been well-established as suppliers of surveying instrument, ALS, TLS, or laser scanners to the surveying and mapping industries. For example, Leica, a well-known surveying supplier that produces numerous surveying instruments, released its newest MLS solution: Leica Pegasus: One.

Table 2.1: Commercially-available MLS systems.

Company		RIEGL	RIEGL	Trimble	Optech	TOPCON	3D laser mapping Ltd.& IGI mbH	Dynascan	SITECO
MLS system		VMX-250	VMX-450	MX8	Lynx –M1	IP-S2 Compact+	StreetMapper	S250	ROAD SCANNER
Laser Scanner	Laser Type	RIEGL VQ-250 (2)	RIEGL VQ-450 (2)	RIEGL VQ-250 (2)	Lynx laser scanner (2)	SICK LMS 291(5)	VQ180 or VQ250	MDL scanner	Faro Focus 3D (3)
	Measuring Principle	Time-of-flight measurement; Echo signal digitalization; Online waveform processing;				Time-of-flight	Time-of-flight measurement; Echo signal digitalization; Online waveform processing;	Time-of-flight	Phase difference
	Maximum range	500 m (to 80% reflectivity target)	800 m (to 80% reflectivity target)	500 m (to 80% reflectivity target)	200 m (to 20% reflectivity target)	80 m (to 10% reflectivity target)	500 m (to 80% reflectivity target)	250 m	120 m (to 90% reflectivity target)
	Minimum range	1.5 m	1.5 m	1.5 m		0.7 m	1.5 m		
	Measure precision	5 mm (1 sigma)	5 mm (1 sigma)	5 mm (1 sigma)	8 mm (1 sigma)	10 mm at range of 1 to 10	5 mm (1 sigma)	±1 cm (1 sigma)	1 mm (at 25 m)
	Absolute accuracy	10 mm	8 mm	10 mm	5 cm (at 100 km/h at good GPS data)	±35 mm	10 mm	±5 mm	±2 mm (at 25 m)
	Field of view	360 °	360 °	360 °	360 °	180 °/90 °	360 °	360 °	H360 ° V320 °
	Scan rate	Up to 100 Hz	Up to 200 Hz	80-200 Hz	100 Hz	75-100 Hz	100 Hz	Up to 30 Hz	48 Hz
	Measurement rate / pulse repetition rate (PRR)	50-300 KHz	Up to 550 KHz	50-300 KHz	75-500 KHz	40 KHz	50-300 KHz	36 KHz	122-976 kHz
	Echoes per pulse	Practically unlimited			Up to 4 echoes		Practically unlimited		

	Angle measurement resolution	0.001 °	0.001 °	0.001 °	0.001 °	0.667 °	0.001 °	0.01 °	H0.00076 ° V0.009 °
	Laser wavelength	near infrared			1550 nm (near infrared)	905 nm (near infrared)	Near infrared		785 nm (near infrared)
Navigation solution		LV-510	LV-510	LV-510	LV-410	40 channels, dual constellation, dual frequency GPS + GLONASS L1/L2; Fiber Optic Gyro	IGI's TERRAcontrol : NovAtel GNSS receiver +IGI's IMU-IId fiber optic gyro IMu	Dual GNSS	LANDINGS navigation system & IXSEA inertial system
	Roll/Pitch	< 5 cm	< 5 cm	< 5 cm	± 5 cm (@ 30 m)	0.5 m -2 m	5 cm	2 cm	7 cm
	Heading	< 5 cm	< 5 cm	< 5 cm			5 cm		5 cm
Camera subsystem		500 MP (4 or 6)	500 MP (4 or 6)	Point Gray Grasshopper ® GRAS - 50S5C (4)	200 / 500 MP (2)	Sony progressive scan color CCDs (6)	12 MP SLR (single-lens reflex)		BASLER Scout cameras (8)
	Lens Size	2/3" CCD	2/3" CCD	2/3" CCD	1/1.8" or 2/3" CCD	1/3" CCD			
	Lens types	5 mm	5 mm	4 mm	F 1.8/ 4.8 mm	2.5 mm			
	Field of view	80 °× 65 °	80 °× 65 °		57 °× 47 °	>80% of full sphere, 360 ° Panorama			
	Exposure (#/s)	8	8	4	3	15	2		Max. 30
Reference		(RIEGL VMX-250, 2013)	(RIEGL VMX-450, 2013)	(Trimble MX-8, 2013)	(Optech Lynx –M1, 2013)	(Topcon IP-S2, 2013)	(StreetMapper, 2013)	(Dynascan S250, 2013)	(Road Scanner, 2013)

(a) Riegl MX-450

(b) MX-8

(c) Lynx

(d) IP-S2

(e) Street Mapper

(f) Dynascan S250

(g) Leica Pegasus:One

(h) Road Scanner

Figure 2.2: Current commercially-available MLS systems: (a) RIEGL VMX-450, (b) Trimble MX 8, (c) Optech Lynx, (d) Topcon IP-S2 Compact+, (e) StreetMapper, (f) Dynascan S250, (g) Leica Pegasus: One (Leica Pegasus: One, 2013), and (h) Road Scanner.

Among the MLS systems listed in Table 2.1 and Figure 2.2, FARO PHOTON 120 scanner in Road Scanner is the most accurate system because it uses the phase shift measuring technology, while the SICK and MDL scanners show the worst accuracies. However, due to with time-of-flight measuring technology, RIEGL, MDL and LYNX scanners can achieve measurement ranges greater than 200 m. RIEGL VQ-450 scanner even can reach up to 800 m.

VQ-250/450, MDL and LYNX scanners provide full 360° coverage, but the FARO and SICK scanners do not. To the quick inventory and inspection of road features Topcon IPS2 uses three SICK LMS291 scanners, and the new generation of SITECO is equipped with three FARO scanners.

As for system portability, as Topcon and MDL systems are very compact and highly integrated without extra control unit, they are easily moved from one platform to another. Although RIEGL, StreetMapper and Optech systems have a portable control unit normally placed at the rear of the vehicle, they are relatively easily moved; however, SITECO and Trimble systems are the less portable because of the large size of the control unit.

Point density is important for a number of applications including road inspections, asset management, landside assessment, and maintenance of bridges, vegetation, power lines, and drainages. For some scanners such as VQ-250/450 and LYNX, point density can be changed by the selectable scan rate pertain to parameters of scan line incremental, and driving speed. Puente et al. (2013) illustrated the relationships of point density with scan rate and driving speed.

Point density varies with measurement range. All MLS systems produce very high cloud densities and a huge amount of data for short scanning distances, such as the distance to the road pavement. Comparably, the Road Scanner, Optech LYNX Mobile Mapper, VMX-250/450, MX8, and StreetMapper produce higher point densities than the Topcon and MDL mobile systems. Different MLS systems are configured with different number of laser scanners. For example, VMX-250/450, StreetMapper, and MX8 employ two VQ-250 laser scanners each; Optech LYNX Mobile Mapper employs two LYNX scanners; the Topcon's IP-S2 employs three SICK laser scanners; and Road Scanner uses a single FARO Photon120, and MDL employs a single Dynascan scanner.

Driving speed is a key factor to determine point density during a survey. As a result, users can adjust the driving speed and incremental angle (scan rate) to determine data volumes with a desired measurement resolution. For example, for Optech LYNX Mobile Mapper, the scan rate is up to 200 rotations per second, the scan-line-to-scan-line spacing ranges 3-17 cm with the ground speed of 20 - 120 km/h. Compared to Optech LYNX Mobile Mapper, VQ-450 scanner from RIEGL can achieve the best specifications of point density. Thus, such high point density enables the use of this laser scanner for evaluating conditions of pavements (potholes, ruts and cracks) during road inspections. However, Dynascan with the scan-line-to-scan-line spacing of 1.1 m at a driving speed of 120 km/h, clearly represents the worst option.

Other than these well-established MLS suppliers for the mapping industry, there are numerous small and large companies in the more highly developed countries that operate individual mobile mapping vehicles, offering their services especially to those agencies that are concerned with highway management and maintenance. Those

companies include Tele Atlas (s-Hertogenbosch, Netherlands), NAVTEQ (Chicago, USA), Google (Mountain View, USA), Immersive Media (Calgary, Canada), Earthmine (Berkeley, USA), TerraPoint (Ottawa, Canada), and Mandli Communications (Madison, USA) (Gordon, 2010a).

2.1.4 Geo-referencing and Scanning Parameters

Calculation of ground coordinates for illuminated objects, termed as "geo-referencing", from a MLS system can be found in the literature (Glennie, 2007). The laser scanner is referenced when its position and orientation relative to the mapping coordinate system is known by a set of navigation system. The navigation data must be precisely time stamped for sensor integration and determination of the exact coordinates of mapping points (Barber et al., 2008).

The coordinates of a target P can be calculated by:

$$
\begin{bmatrix} X_P \\ Y_P \\ Z_P \end{bmatrix}^M = \begin{bmatrix} X_{GPS} \\ Y_{GPS} \\ Z_{GPS} \end{bmatrix}^M + R_{IMU}^M(\omega,\varphi,\kappa) \cdot \left(R_S^{IMU}(\Delta\omega,\Delta\varphi,\Delta\kappa) \cdot r_P^S(\alpha \quad d) + \begin{bmatrix} L_X \\ L_Y \\ L_Z \end{bmatrix}_S^{IMU} - \begin{bmatrix} L_X^{G/I} \\ L_Y^{G/I} \\ L_Z^{G/I} \end{bmatrix}_{IMU}^{GPS} \right)
$$

$$(2.1)$$

where, parameters in Eq. (2.1) and their descriptions are listed in Table 2.1.

Table 2.2: Parameters of the geo-referencing equation.

Parameters	Description
X_P, Y_P, Z_P	The location of the target P in the mapping frame.
$X_{GPS}, Y_{GPS}, Z_{GPS}$	The location of GNSS antenna in the mapping frame.

$r_P^S(\alpha \quad d)$	Relative position vector of Point *P* in the laser scanner coordinate system, α and d for scan angle and range measured and returned by the laser scanner.
L_X, L_Y, L_Z	The lever arm offsets from the navigation origin (IMU origin) to the measurement origin of the laser scanner. These values must be determined by system calibration or measurement.
$L_X^{G/I}, L_Y^{G/I}, L_Z^{G/I}$	The lever arm offsets from the IMU origin to the GPS origin. These values must be determined by system calibration or measurement.
$R_{IMU}^M(\omega, \varphi, \kappa)$	Rotation matrix between IMU and mapping frame, (ω, φ, κ) are the roll, pitch and yaw of the sensor with respect to the local mapping frame. These values are given by the IMU system.
$R_S^{IMU}(\Delta\omega, \Delta\varphi, \Delta\kappa)$	Rotation matrix between the laser scanner and IMU, ($\Delta\omega, \Delta\varphi, \Delta\kappa$) are the boresight angles which align the scanner frame with IMU's body frame. Those values must be determined by a system calibration.
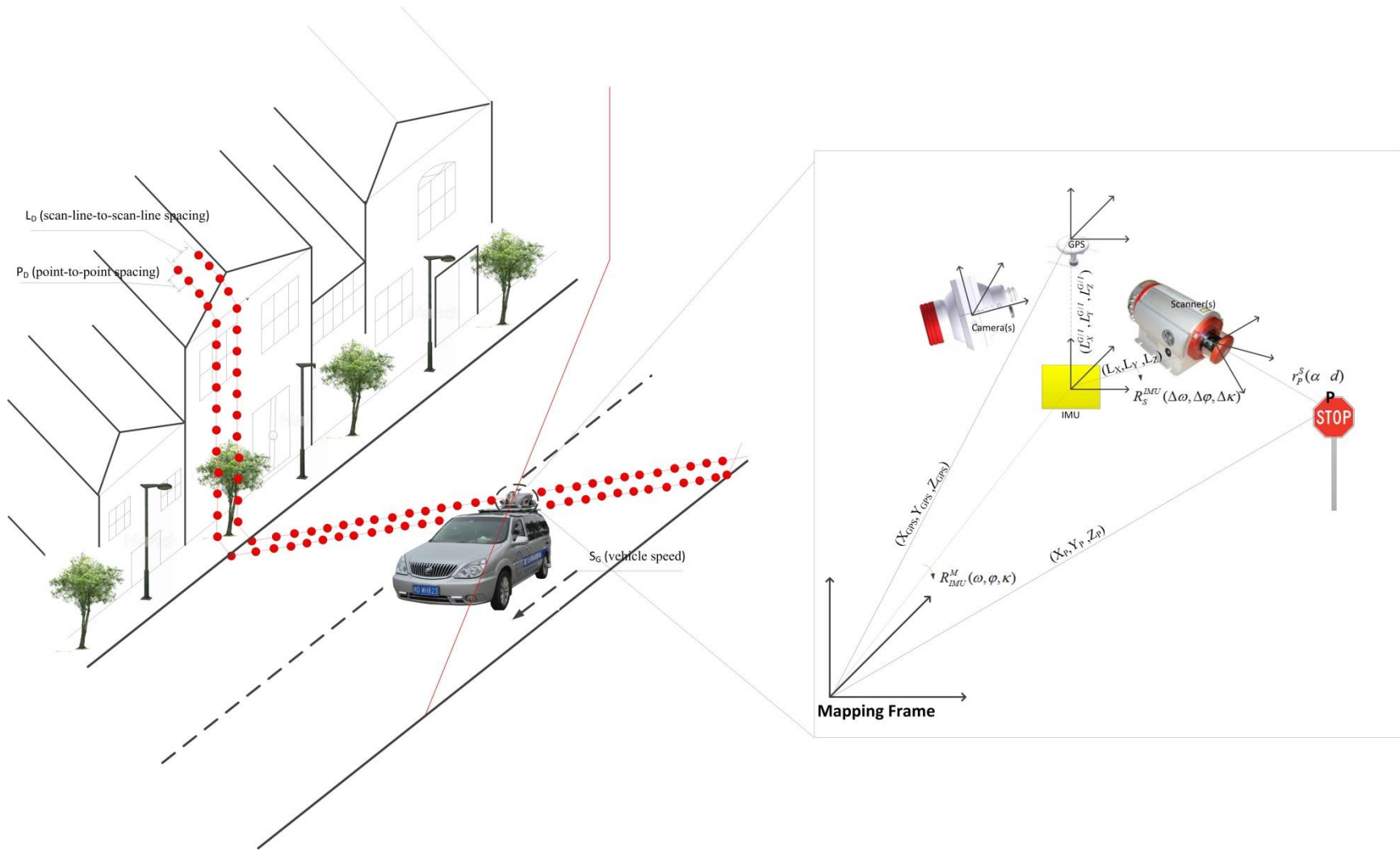
Figure 2.3: An illustration of Geo-referencing.

For a laser scanner, the following parameters can be calculated:

$$S_s[lines/s] = \frac{L_{increment}[\text{deg}] \times PRR[Hz]}{360°} \tag{2.2}$$

$$L_{Dist}[m/line] = \frac{S_G[m/s]}{S_s[lines/s]} \tag{2.3}$$

$$P_{Dist}[m] = \tan(L_{Increment}[\text{deg}]) \times T_{Dist}[m] \tag{2.4}$$

$$P_{Density}[pts/m^2] = \frac{1}{P_{Dist}[m] \times L_{Dist}[m]} \tag{2.5}$$

where, parameters in the equations and their descriptions are listed in the Table 2.3.

Table 2.3: Scanning parameters.

S_s	Scan speed/scan rate
S_G	vehicle speed
L_{Dist}	scan-line-to-scan-line spacing
P_{Dist}	point-to-point spacing
T_{Dist}	Target distance
$L_{increment}$	Scan line incremental
$P_{Density}$	Average point density

From Eqs. (2.2) - (2.5), the average point density of the collected data depends on the scan speed S_s, vehicle speed S_G, and system effective measurement rate /*pulse repetition* rate (PRR). Scan speed S_s is determined by *PRR* and scan line incremental. Scan-line-to-scan-line spacing L_{Dist} is proportional to S_G and inversely proportional to S_s, indicating that the higher the vehicle speed related, the lower the scan-line-to-scan-

line spacing in the running direction, while the higher the scan speed related, the higher the scan-line-to-scan-line spacing. For example, for a RIEGL VMX-450 system, the minimum scan-line-to-scan-line spacing of 8 cm can be observed with a vehicle speed of 50 km/h, a scan angular increment of 0.1143∘, and a system effective measurement rate of 550 KHz. However, point-to-point spacing P_{Dist} in a single scan line varies much with scan angles and scan counts but very little with vehicle speeds. The point density within the scans varies greatly with both the vertical orientation of the features being scanned and the distance from the scanner (Lim et al., 2013). Puente et al. (2013) illustrated the relationships of point density with scan rate and driving speed. Although the maximum range of the scanner is approximately 800 m for RIEGL VMX-450, in the scans the point density dropped significantly beyond 30 m because of the flatness of the terrain and lack of tall vertical features.

2.1.5 Error Analysis

Eq. (2.1) defines the relationship among all seventeen observation parameters for producing geo-referenced point clouds. To examine final point accuracy, we discuss typical errors of those observations.

1) IMU attitude errors: The IMU component of a MLS system provides roll, pitch and heading angles that represent the rotation relationship between IMU and mapping frames. An IMU consists of two main parts: (1) three orthogonal accelerometers, each of which measures the acceleration along a specific axis, and (2) three orthogonal gyroscopes, each of which measures and maintains orientation, based on the principles of conservation of angular momentum. Accordingly, systematic errors of the sensor include accelerometer biases and

25

gyro drifts. Typically, as IMU components are supplied by 2 or 3 different system manufacturers, their accuracies can be examined from the manufactures' technical specifications. For example, RIEGL VMX-450 is configured a set of Applanix® POS LV 510, whose typical accuracy can be found on the manufacturer's technical specification (www.applanix.com). Applanix® POS LV 510 can deliver 0.005 ° in roll and pitch and 0.015 ° in heading (at 1 sigma).

2) Positioning errors: The positioning accuracy of a GNSS subsystem is influenced by the following factors: multipath, atmospheric errors, baseline length, poor satellite geometry, and loss of lock; therefore, the absolute level of the positioning accuracy for MLS survey is difficult to quantify. Ideally, the positioning accuracy is expected 1cm +1 ppm horizontally and 2cm +1 ppm vertically within a relatively short kinematic baseline (< 30 km) (Bruton, 2000).

3) Laser scanner errors: Most laser producers provide two main error components: errors in distance and errors in angles. The error in distance is caused by the internal accuracy of the clock that measures the time of flight and the width of the output laser pulse; the error in angle is due to the angular resolution of the laser scanner angle encoder and the uncertainty of beam divergence. For example, REIGL VQ-450 scanner delivers the ranging and angular measurement accuracies of 5 mm and 0.044 °, respectively.

4) Boresight errors: The boresight errors result from the misalignments between IMU and laser scanner measurement axes. To process laser scanning data, the location of the scanner and its orientation in relation to IMU must be precisely known because alignment errors will be propagated over the distance between the

sensor and the object being scanned. Boresighting is a very precise measurement process that attempts to correct any mounting misalignments between IMU and laser scanners (Rieger et al., 2010; Lim et al., 2013).

5) Lever-arm offset errors: Usually, the origins of laser scanners and IMU cannot be collocated; the lever-arm offsets thus must be known in order to obtain accurately geo-referenced MLS point clouds. There are two methods to measure the lever-arm offsets: calibration and physical measurement. The second one is widely used because it is simple to implement. Accordingly, the measurement errors are also introduced because of the assumption of the alignment of two sensors 'axes.

The above discussion of error sources for a MLS system demonstrates that the accuracy of MLS point clouds depends on the underlying accuracy of GNSS/IMU navigation solution and laser scanners. Among those errors, two possible error sources (boresight and lever-arm) can be recovered by system calibration. In fact, the overall accuracy of MLS point clouds is mainly affected by the navigation solution because multi-path effects and signal shading that are caused by high-rise buildings and trees along the street deteriorate GNSS conditions in a moving vehicle (Haala et al., 2008; Barber et al., 2008). Compared to a long distance from an aircraft to the ground in ALS, GNSS positioning errors of a MLS system have a much greater impact on the overall error budget, owing to a short distance between a laser scanner and a scanned object, even about several to ten metres. To improve MLS data accuracy, a post-processing procedure of navigation trajectory is indispensable. For example, a post-processing package of Applanix POS LV 510 is used to process GNSS/IMU data for RIEGL VMX-450 data.

2.2 Road Information Extraction Techniques: An Overview

2.2.1 Road-surface Extraction

Researchers have developed a variety of methods to extract roads from satellite and aerial images based on geometrical, radiometric, topological, functional and contextual characteristics (Vosselman and Knecht, 1995). Normally, common strategies are grouped into two categories: semi-automatic and automatic road extraction algorithms. The former mainly includes least squares matching (Vosselman and Knecht, 1995; Kim et al., 2004), dynamic programming (Gruen and Li, 1997; Dal Poz and Do Vale, 2003), and active contours (Peng et al., 2010). Mena (2003) summarized several automatic road extraction methods, including road tracking methods, morphological analysis, dynamic programming and snakes, multi-scale and multi-resolution analysis, stereoscopic analysis, multi-temporal analysis, and other knowledge representation and fuzzy modeling techniques for road extraction. Although road extraction from satellite and aerial images has been researched over four decades, good and stable performance has not been achieved due to image sources, image resolution, and landscape complexity. Meanwhile, bad situations, such as poor illumination and bad weather, cause limitations to compute vision and image interpretation.

Although much effort has been made to extract road features from MLS data, efficient interpretation methods are still in a state of early development. Most algorithms roughly follow the common steps when interpreting MLS point clouds: (1) detection of planar or smooth surfaces, and (2) classification of points or point clusters using data features such as local point patterns, intensity, and pulse return information (Pu et al., 2011; Darmawati, 2008).

In the first category, Takashi and Kiyokazu (2006) directly identified road lanes with curvature, yaw angles, and offsets derived from point clouds by Hough Transform. However, applying Hough Transform to large volumes of MLS data is time consuming. Yuan et al. (2010) detected roads by employing a fuzzy cluster method based on maximum entropy theory to segment points and a weighted least-square linear fitting algorithm to differentiate linear and nonlinear distributed point segments. Similarly, any computational methods for extracting roads from MLS data are time consuming.

Smadja et al. (2010) suggested a two-step road-surface extraction algorithm based on local road shape. RANSAC is first applied to each scan line individually for roughly estimating road sides. And then, the curb candidates are selected for road extraction by a multi-frame accumulated map. Yang et al. (2013) also classified road points by detecting curbs scan-line by scan-line. Although processing MLS data scan-line by scan-line could improve computational efficiency, classifying roads by detecting curbs from single scan-lines may fail or be inaccurate when curbs are hidden behind other cars on the road or parked cars.

In the second category, Zhao and Shibasaki (2002) conducted a scan-line based classification, where points on the scan lines are first segmented into linear patches by a height variance, and then the linear patches are classified as the groups of vertical building surface, road surface, other surface, window, tree and others, and unknown objects by comparing with other neighboring linear segments.

Moreover, Manandhar and Shibasaki (2001) used point-density histogram analysis to extract road surfaces from MLS data, as a result of road surfaces near to the laser scanner. Li et al. (2004) also introduced a point-density criterion for road extraction by calculating

the density of projected points (DOPP). However, these methods may fail when erroneous points exist in MLS data.

Recently, intensity is another factor considered in road-information extraction (Chen et al., 2009). Clode et al. (2007) presented a progressive classification method for separating road from off-road points regarding intensity and elevation information. However, intensity values are faded towards two edges of a road because of the longer scanning distance from the laser scanner and the larger incidence angle. Calibrated intensity could give added values for laser scanning data processing in object recognition and classification.

As curbs represent boundaries of roads in an urban environment, some researchers detected curbs to identify road regions and calculate obstacle-free areas (Liu et al., 2013). Zhou and Vosselman (2012) extracted curbstones for separating the road surface from the adjacent pavement. Zhang (2010) combined a prior knowledge about the minimal width of roads with elevation information for classifying road regions and edges. These methods are time saving; however, the quality of curbs to be detected could be unreliable because of occlusion.

To compensate for the limitations of MLS data, some researchers integrated MLS data with other data sources. Yu et al. (2007) studied the integration of laser scanning data, video data, and scanning profiles to create detailed models of road surfaces. Some researchers merged ALS data with MLS/TLS data for road extraction (Boyko and Funkhouser, 2011; Zhou and Vosselman, 2012). Although fusing different data sources with MLS data can improve the accuracies and correctness of road extraction, registering these data sources into a uniform coordinate system requires much work.

Most reviewed methods which use mathematical estimations for such large volumes of MLS data, are time consuming and computationally intensive. As reviewed, detecting curbs from MLS data is efficient for separating road points from off-road points. In addition, most urban roads are designed with curbs for separating them from pedestrian sidewalks. As a result, there is a need to develop a road extraction algorithm which will provide an accurate estimation of road edges based on road features such as curbs and other implicit MLS data characteristics. Besides geometric information, other implicit MLS data information such as trajectory can be obtained from MLS systems. However, little research has been carried out to extract roads based on the trajectory that record precise and real-time positioning information of the vehicle.

2.2.2 Road-marking Extraction

Road markings on paved roadways, as critical features in traffic management systems, have important functions in providing guidance and information to drivers and pedestrians. For example, driver-assistance systems require reliable environmental perception to improve traffic safety by informing motorists and preventing accidents. Along with pavement condition and road topography, the visibility of road markings is a key element in accidents where the road itself is the cause. Especially, in highly populated urban environments, high accident rates are caused by the absence of clearly-presented road signals (Carnaby, 2005). In order to maintain high technical standards for perfect visibility, highway maintenance departments need a practical system for monitoring road markings.

Generally, road markings are highly retro-reflective surfaces capable of reflecting the incident light back to its energy source. Based on this retro-reflectivity, many studies

have been conducted to distinguish road markings from digital images or videos (Charbonnier et al., 1997; Rebut et al., 2004; McCall and Trivedi, 2006; Li et al., 2007; Wang et al., 2009; Kheyrollahi and Breckon, 2010; Danescu and Nedevschi, 2010). Most algorithms commonly consist of the following two steps: candidate extraction and road-marking classification. Regarding the highly retro-reflective property of road markings, many methods, such as multi-level-threshold segmentation (Kheyrollahi and Breckon, 2010), scan line (Charbonnier et al., 1997), and histogram analysis (Wang et al., 2009), first identify road-marking candidates. To recognize road markings, the candidates are classified by fuzzy reasoning (Li et al., 1997), K-Nearest Neighbor (Rebut et al., 2004), support vector machines (Wang et al., 2009), artificial neural network (Kheyrollahi and Breckon, 2010), and decision tree (Danescu and Nedevschi, 2010).

When it comes to road-marking extraction from either digital photographs or videos, precise geometrical information is limited by the following environmental factors: (1) the shape and type of road markings, such as solid continuous lines , arrows, and words, (2) the road surface material, such as light pavement, dark pavement, or a combination of different pavements, (3) weather conditions and the time of day that has the greatest impact on the visibility of road surface, and (4) complex shadowing from trees and moving vehicles (McCall and Trivedi, 2006). Although work on road-marking extraction from digital photographs and videos has been pursued for years, fully automated road-marking extraction has remained a challenge.

To extract road markings from MLS data, the first step is to identify points belonging to the road surfaces. On the road surfaces, road markings are highly retro-reflective surfaces painted on roads; as a result, the reflectance of the target in the form of intensity

can be used to identify road markings (Chen et al., 2009). Based on intensity differences between road surfaces and pavement markings, Toth et al., (2008) extracted road markings as the ground control for quality assessment (QA) or quality control (QC) of the image data. Smadja et al. (2010) applied a simple threshold to intensity data for extracting road markings. Yang et al. (2012) outlined solid-edge-line and broken-lane-line markings by first applying an interpolation method to MLS points, and then segmenting the GRF image using intensity and elevation-difference information. Finally, road markings were estimated by integrating their semantic knowledge (e.g., shape, size). However, as most of these algorithms have applied a global threshold-based segmentation algorithm to the intensity data of MLS point clouds, much noise is introduced, making this method less effective in road-marking extraction. The intensity data highly depend on the ranges from the scanner to objects, the incidence angles of laser pulses, and the material properties of road surfaces. Thus, the intensity data need to be normalized prior to segmentation.

Jaakkola et al. (2008) modeled road markings from the intensity data acquired from an FGI Roamer system. The method is composed of (1) radiometric correction and segmentation of the intensity data, (2) performing morphological operations to obtain a set of segments, and (3) classifying these segments as crosswalks and other lines regarding their properties. However, the algorithm can be only used for parking space lines and zebra crossings. The radiometric calibration fitted a second-order curve that was performed between the peaks on both sides of the scanning centre.

Chen et al. (2009) located road-marking candidates using adaptive thresholding, where thresholds were invariant to absolute values of laser beam returns, and road

markings were extracted with Hough transform clustering, followed by a refinement step with trajectory constraint and geometry check. The use of Hough transformation for road-marking extraction is weakened by specifying the number of road markings to be detected, which is a limiting factor for complex types of road markings such as hatching and words.

Vosselman (2009) introduced distance-dependent intensity normalization and connected component analysis for identifying road markings. Although several types of road markings are identified, a close-up view of a bicycle marking shows that the extracted markings are incomplete with distinguishable noise. The pre-defined shapes used for fitting road-marking segments are considered to be the cause.

Aside from road markings, other high-reflective urban elements (e.g., traffic signs, retro-reflectors, tree, and grass) and their distortion effects (e.g., saturation and blooming) may have a negative effect on road-marking extraction. Some measures, such as height information and shape criteria, need to be taken into consideration to refine the extracted road markings (Yang et al., 2012). Moreover, besides of intensity information, other implicit information, such as scanning data pattern, where MLS point density nominally drops perpendicular to the vehicle running direction, will facilitate to extract road markings efficiently.

2.2.3 Pavement-crack Extraction

Research on asphalt concrete-surfaced pavement distress measurement is an indispensable part of pavement management systems to cost-effectively maintain and rehabilitate roads. Cracking, as the most common type of the asphalt concrete-surfaced pavement distress, is caused by fracture due to excessive loading, fatigue, thermal

changes, moisture damage, slippage or contraction. Usually, cracking is grouped into: fatigue, longitudinal, alligator, edge, reflection, block, and transverse types, regarding shape and position (Lee, 1992; McGhee, 2004). In the early period, the inspection and evaluation of cracks was involved high degrees of subjectivity and hazardous exposure and low production rates. Currently, visual measurement techniques have been mostly explored to inspect and evaluate pavements on videos or digital images collected from a specially equipped vehicle.

The growing demand for transportation service motivates to cost-effectively maintain a modern transportation system as safe, secure and supportive road networks. It is indisputable to develop an automated pavement inspection system that provides an intelligent strategy for pavement management. To this end, it is significantly important to obtain accurate and reliable crack extraction results. Over the years, much effort has been made on this subject. Most existing algorithms of crack extraction are intuitively based on digital images and videos.

Tsai et al. (2010) summarized six common segmentation and classification methods for pavement distress, and quantitatively compared those six methods with the ground-truth cracks visually identified by pavement engineers. The reviewed segmentation methods include regression/relaxation thresholding, Canny edge detection, crack seed verification, multi-scale wavelets, iterative clipping method, and dynamic optimization-based method.

Koutsopoulos et al. (1993) stated that the statistical thresholding is the best thresholding method for pavement distress segmentation in terms of efficiency and

insensitivity to segmentation parameters, compared to other thresholding methods such as Otsu's method (Otsu, 1979) and the Kittler method (Kittler and IUingworth, 1986). However, thresholding-based segmentation methods have difficulties in gaining a stable performance owing to a diversity of pavement environments and materials. In contrast with the gray-scale similarity based thresholding methods, gray-scale discontinuity based edge detection techniques segment cracks by outlining their edges. Ayenu-Prah and Attoh-Okine (2008) used a sobel edge operator to detect cracks, in which a bi-dimensional empirical mode decomposition was applied to smooth crack images and remove salt and pepper noise Among conventional edge detection algorithms, the Canny edge operator is capable of detecting weak edge and is robust to the presence of noise (Canny, 1986). Unfortunately, this advantage is weakened by a problem that the optimum parameters used in the algorithm vary with each image. Accordingly, false edges or boundaries can be generated, resulting in poor effectiveness in crack extraction (Tsai et al., 2010). Aiming to automatically find a threshold value, Yoshida and Tanaka (2009) used a fractal dimension to evaluate the fitness of binarized images, locally and globally. Rather than the use of fixed thresholds, fuzzy logic was introduced for the determination of the segmentation threshold by the brightness membership function (Cheng et al., 1999).

The wavelet transform is another common technique for crack extraction, which decomposes a pavement image into sub-bands for separating noise from the background, based on the statistical criteria derived from wavelet coefficients (Cuhadar et al., 2002; Zhou et al., 2006). According to Mallat and Zhong (1992), wavelet transform-based algorithms can detect irregular structures; thus, they are feasible for crack extraction. To overcome the difficulties of crack extraction at different scales, multi-scale wavelet

transform methods were subsequently presented to deal with pavement images with various spatial and spectral resolutions (Subirats et al., 2006). However, due to the anisotropic characteristic of wavelets, wavelet-based approaches often fail to process cracks with high curvature or poor continuity. Similarly, other transform-based methods, such as Beamlet transform (Ying and Salari, 2009; Wei et al., 2010) and Contourlet transform (Shu and Guo, 2010), were proposed for crack extraction.

The dynamic optimization-based method uses global properties of cracks such as elongated shapes to effectively handle pavement images with low Signal-to-Noise Ratio (SNR). This method has a good performance, but it is computationally intensive (Tsai et al., 2010). Nguyen et al. (2011) proposed a method that considered both spectral and shape features for segmenting cracks from a noisy background using conditional texture anisotropy. Experiments on real cracks in pavement images demonstrated that this method can achieve a good performance by 93.6% extraction rate and 13.7% false alarms. Similar to dynamic programming, an F* Seed-growing approach was presented for crack extraction (Li et al., 2011). This approach comprises the seed-aggregating using neighbouring difference histogram method and the F* seed-growing algorithm.

Other classical image processing algorithms such as mathematical morphology were employed to detect cracks in road surface images (Tanaka, 1998). Although a part of success has achieved, the mathematical morphology-based method is limited to the three structure elements (e.g., disk, line, and square) and the choice of parameters. A number of efforts on crack extraction have been made from artificial intelligence, data mining, machine learning, and neural network. Oliveira and Correia (2008) used Bayesian classification techniques to obtain tree types of cracks (e.g., longitudinal,

transversal, and miscellaneous). First, a series of training samples are interactively selected, and then a feature space that includes the average and the standard deviation of pixel intensities is defined. Finally, a Bayesian quadratic classifier is applied over the normalized feature space to label the pixels. In Gavilán et al. (2011), a linear Support Vector Machine (SVM) based classification method was employed to identify cracks based on textural-related gray-level co-occurrence matrix (GLSM) measures. It is noted that it is difficult to determine two parameters of SVM-based classifiers, in terms of variations of cracks and the quality of pavement images. Similarly, neural network techniques were applied for the automatic classification of road cracks (Bray et al., 2006; Saar and Talvik, 2010). The main drawback of those approaches is to spend much time in training considerable samples that have a good representation of real cracks.

Yu et al. (2007) inspected pavement distresses from raw MLS data using accurate depth information and concluded that the proposed two-stage automation procedure has a significant improvement over contemporary commercial video-based vision systems. However, in practice, it is challenging to process such large volumes of 3D MLS data to obtain readable and comprehensive crack information. The intensity information of MLS data is an alternative. Compared to highly-spectral-resolution digital images, a crack intensity image has a low contrast with its surroundings, low SNR owing to particle materials of asphalt concrete-surfaced roads. This results in most existing algorithms ineffective to crack extraction.

Most methods have been developed for identifying cracks based on digital images or videos, field work, and specific laser scanning equipment. Little and no research has been carried out to extract cracks from MLS data, because some researchers claim that it

is questionable whether it can support the detailed task of crack extraction since the widths of most cracks are at millimeter level, but MLS data seems too sparse for the crack extraction task. However, there is a need to develop a method that will extract cracks efficiently and accurately from MLS data because MLS technologies continue to advance for providing much denser MLS data for cracks at millimeter level in the foreseeable future. For example, laser scanners have been developed with measurement rates of up to 550 kHz and scanning rate at up to 200 Hz in the past five years. Thus, MLS data need to be thoroughly explored for crack extraction.

2.3 Fundamental Algorithms

Three automated algorithms will be developed in this research for extracting road features, such as the road surfaces, road markings, and pavement cracks, from MLS data. In order to improve computational efficiency, all 3D road data will be converted into 2D raster image data using intensity information for extracting road markings and pavement cracks. Thus, some fundamental image processing algorithms will be used in the research. Specifically, these image processing algorithms include Otsu's method, morphological operation, and tensor voting. Otsu's method will be used to segment road-markings from road data because road-markings are painted on the road surfaces with highly reflective materials and produces intensities with high values. Morphological operation will be used for road-markings. Tensor voting, a perceptual grouping method in computer vision, will be applied to the extraction of pavement cracks. The following subsections will detail the three algorithms. The usage of these algorithms in this thesis will be described in Chapters 5 and 6.

2.3.1 Otsu's Method

Otsu's method, proposed by Otsu (1979), is widely implemented as the default approach to image thresholding in some commercial or free software such as Matlab. Assume that an image contains N pixels, and can be represented in gray levels χ. The number of pixels at level i can be denoted as f_i. As a result, the pixel number N of the image can be represented as:

$$N = f_1 + f_2 + f_3 + ... f_i + ... + f_\chi \tag{2.6}$$

For a given gray-level image, the occurrence probability of gray level i is calculated by:

$$p_i = f_i / N, \quad p_i \geq 0, \quad \sum_{i=1}^{\chi} p_i = 1 \tag{2.7}$$

If an image can be divided into two classes: C_1 and C_2, that is, foreground (e.g., road markings) and background, at level t, where C_1 contains gray level from 0 to t, and C_2 contains gray level from $t+1$ to χ. Their cumulative probabilities (w_1 and w_2) and mean levels (η_1 and η_2) are calculated, respectively.

$$w_1 = \sum_{i=1}^{t} p_i$$
$$w_2 = \sum_{i=t+1}^{\chi} p_i \tag{2.8}$$

and

$$\eta_1 = \sum_{i=1}^{t} i p_i / w_1$$

$$\eta_2 = \sum_{i=t+1}^{\chi} i p_i / w_2$$

(2.9)

The mean gray-level value over the whole image is:

$$\eta = \sum_{i=1}^{t} i p_i$$

(2.10)

The variance of classes C_1 and C_2 will be:

$$\delta_1^{2}(t) = \frac{\sum_{i=1}^{t} (i - \eta_1)^2 p_i}{\sum_{i=1}^{t} p_i} = \frac{1}{w_1} \sum_{i=1}^{t} (i - \eta_1)^2 p_i$$

(2.11)

$$\delta_2^{2}(t) = \frac{\sum_{i=t+1}^{\chi} (i - \eta_2)^2 p_i}{\sum_{i=t+1}^{\chi} p_i} = \frac{1}{w_2} \sum_{i=t+1}^{\chi} (i - \eta_2)^2 p_i$$

The variance of the whole image is:

$$\delta^2 = \sum_{i=1}^{t} (i - \eta)^2 p_i$$

(2.12)

The variance can be also written as:

$$\delta^2 = w_1 \delta_1^2(t) + w_2 \delta_2^2(t) + w_1 (\eta_1 - \eta)^2 + w_2 (\eta_2 - \eta)^2 = \delta_W^2(t) + \delta_B^2(t)$$

(2.13)

Where, $\delta_W^2(t)$ is denoted as the within-class variance, and $\delta_B^2(t)$ is denoted as the between-class variance.

Otsu's method selects an optimal threshold (t) that maximizes the between-class variance $\delta_B^2(t)$ based on the discriminant analysis.

$$\delta_B^2(t) = \frac{[\mu(t) - \eta w_2]^2}{w_1 w_2} \tag{2.14}$$

where,

$$\mu(t) = \sum_{i=1}^{t} ip_i \tag{2.15}$$

As a result, an optimum bi-modal threshold can be readily selected by the discriminant criterion proposed by Otsu's method by maximizing the separability of the two classes in gray levels.

2.3.2 Morphological Operation

Morphology is a broad set of image processing operations applied on images (originally binary images, and later extended to gray-scale functions and images) (Dougherty and Lotufo, 2011). Morphological operations, by applying a structuring element to an input image and creating an output image of the same size, affect the form, structure or shape of an object to be processed. In a morphological operation, there are two important elements: a binary image and a structuring element. The structuring element is also a binary array, with an origin, size, and shape, as shown in Figure 2.4. A morphological operation compares the structuring element to the neighborhood of each pixel in the input binary image, and then determines its output. By choosing the size and shape of the structuring element, a morphological operation sensitive to specific shapes can be constructed in the input image. The morphological operations are widely used in

image pre- or post-processes (e.g., filtering, thinning, and pruning) for representing or describing the shapes of objects such as boundaries or skeletons. The most basic morphological operations are dilation and erosion. Dilation adds pixels to the boundaries of objects in an image, while erosion removes pixels on object boundaries.
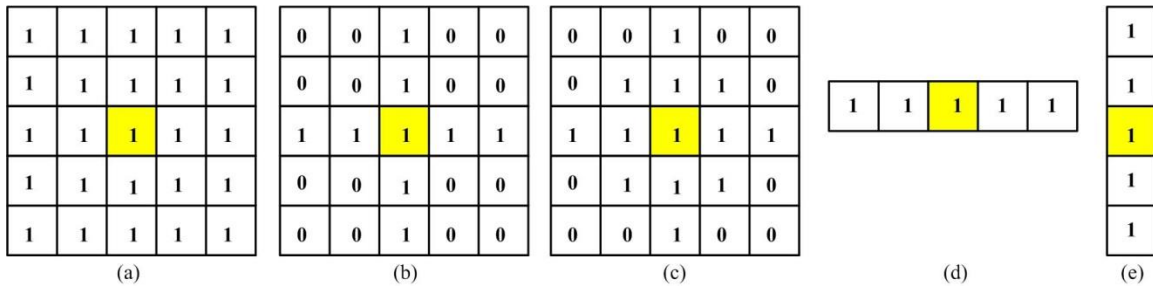
Figure 2.4: Several examples of the structuring element with different shapes (yellow cells means origins): (a) 5×5 square shaped, (b) 5×5 cross shaped, (c) 5×5 diamond shaped, (d) 1×5 horizontal linear shaped with direction =0°, and (e) 5×1 vertical linear shaped (or 1×5 horizontal linear shaped with direction θ=90°).

2.3.3 Tensor Voting

Perceptual grouping, introduced in Lowe (1985), is a well-known tool that extracts significant image relations from lower-level primitive image features and groups them to obtain meaningful higher-level structures (Medioni et al., 2000). According to the Gestalt Laws of perceptual grouping, grouping principles, such as proximity, similarity, good continuation, closure, and symmetry, are combined into a cost function called saliency and employed to infer salient structures from data. Perceptual grouping approaches have been evolved from symbolic methods, clustering, and local interactions to human visual system. Perceptual grouping became attractive in the human vision system because it reduces the complexity of the object recognition task, as well as the necessity for prior knowledge when inferring salient structures.

43

As an approach to perceptual grouping, tensor voting is capable of inferring salient features (such as curves, regions, junctions, endpoints, and boundaries in 2D) based on proximity and continuation constraints. Input data are first encoded as elementary tensors. The support information of the proximity and continuation constraints propagates from tensor to tensor in a neighbourhood through a voting process, by which the saliencies of perceptual structures can be estimated from noisy and corrupted data in the form of votes. The more votes received at each tensor, the stronger the probability of a salient feature being present at a certain location (Guy and Medioni 1996, 1997; Tang and Medioni , 1998, 2002; Tong and Tang, 2005; Park et al., 2012; Dinh et al., 2010).

The tensor voting framework comprises two elements: a tensor representation, which is expressed by means of a symmetric, non-negative definite matrix, and a linear tensor voting mechanism, which is similar to linear convolution. Oriented and unoriented input is encoded into tensor-form representations and exchanges their information with their neighbours through pre-calculated tensor voting fields. Afterwards, according to the prevailing orientation, a generic second order, symmetric, non-negative definite tensor is produced to encode the local orientation of features (tensor orientation) and magnitude (tensor saliency). It can be decomposed into stick and ball tensors. Finally, geometric features are inferred after tensor analysis.

(1) Tensor Representation

A second order symmetric tensor is equivalent to a 2×2 matrix in 2D. Through eigenvalue decomposition, the 2×2 matrix is decomposed into two eigenvalues (λ_1, λ_2 ($\lambda_1 >$

λ_2)) and their associated eigenvectors (e_1, e_2). Therefore, an arbitrary second order, symmetric, non-negative definite tensor can be described as:

$$T = (\lambda_1 - \lambda_2)e_1 e_1^T + \lambda_2 (e_1 e_1^T + e_2 e_2^T).$$ (2.16)

The first term in Eq. (2.16) corresponds to a 2D stick tensor that indicates an elementary curve element with e_1 as its curve normal. The second term corresponds to a ball tensor which indicates that a perceptual structure has no orientation preference. The second order tensor is graphically represented as an ellipse in 2D, where eigenvectors e_1 and e_2 give the ellipse orientation, and eigenvalues λ_1, λ_2 give its shape and size. As for the curve element, the size of the stick tensor ($\lambda_1 - \lambda_2$) thus indicates the curve saliency.

(2) Voting in 2D

Based on the tensor representation in 2D, an input is first encoded with tensors. If the input has no orientation, it is encoded as a ball tensor with eigenvalues of $\lambda_1 = \lambda_2 = 1$, as a form of an 2 $\times$2 identity matrix $T = \begin{bmatrix} 1 & 0 \\ 0 & 1 \end{bmatrix}$. If the input has an orientation $n(n_x, n_y)$, it is encoded as a stick tensor with eigenvalues of $\lambda_1 = 1$ and $\lambda_2 = 0$, as a form of a 2 $\times$2 symmetric matrix $T = \begin{bmatrix} n_x n_x & n_x n_y \\ n_x n_y & n_y n_y \end{bmatrix}$.

After the input has been encoded with tensors, it information is propagated to their neighbors following the Gestalt principles of smoothness, proximity, and good continuation, which is termed as tensor voting. As presented in Figure 2.5, two tensors, positioned at O with an orientation $\bar{N}$ parallel to the y-axis and P , are named as the voter and receiver, respectively. The arc length s and the curvature κ are given by

45

$s = \theta L / \sin(\theta)$ and $\kappa = 2\sin(\theta) / L$, respectively. Thus, the path from O to P, defined by an osculating circle, is the most likely smooth path since it maintains constant curvature given the assumption of the voter and the receiver belonging to the same perceptual structure. Thus, the vote at position P cast from position O is defined as:

$$V(P) = DF(s,\kappa,\sigma)N_P N_P^T \tag{2.17}$$

where,

$$DF(s,\kappa,\sigma) = e^{-(\frac{s^2+c\kappa^2}{\sigma^2})}, \tag{2.18}$$

where $DF(s,\kappa,\sigma)$ is the saliency decay function, N_P is the normal vector perpendicular to the tangent of the same osculating circle at position P, which is given by

$$N_P = N_O[-\sin(2\theta), \cos(2\theta)]^T \tag{2.19}$$

The scale parameter σ is viewed as a measure of smoothness, and is the only free parameter for users. c controls the degree of decay with curvature, which is defined as:

$$c = \frac{-16\log(0.1)\times(\sigma-1)}{\pi^2}. \tag{2.20}$$

A notion of voting field is introduced to store pre-computed votes cast from stick or ball voters to receivers at various distances and angles. A voting field is used to look up the orientation and magnitude of the votes cast. The tensor voting framework provides two forms of voting fields: stick voting field (see Figure 2.5 (b)) and ball voting field (see Figure 2.5 (c)). The extension of the voting field is controlled by the scale parameter σ. A small σ corresponds to small voting neighborhoods, and makes the voting process local, susceptible to outlier corruption and preserving details, while a large σ

corresponds to large voting neighborhoods and enforces a higher degree of smoothness, thus assisting in noise removal. Note that the stick field is limited to exist only at $|\theta| \leq 45°$, and θ is also called the field aperture. Beyond the angle scope, the smoothest path from O to P cannot be represented by the osculating circle formed by the tensors at O and P. To compute a vote cast from a tensor, first, the voting field is aligned to the tensor. Second, the magnitude and orientation of the receiver can be looked up from the voting field.
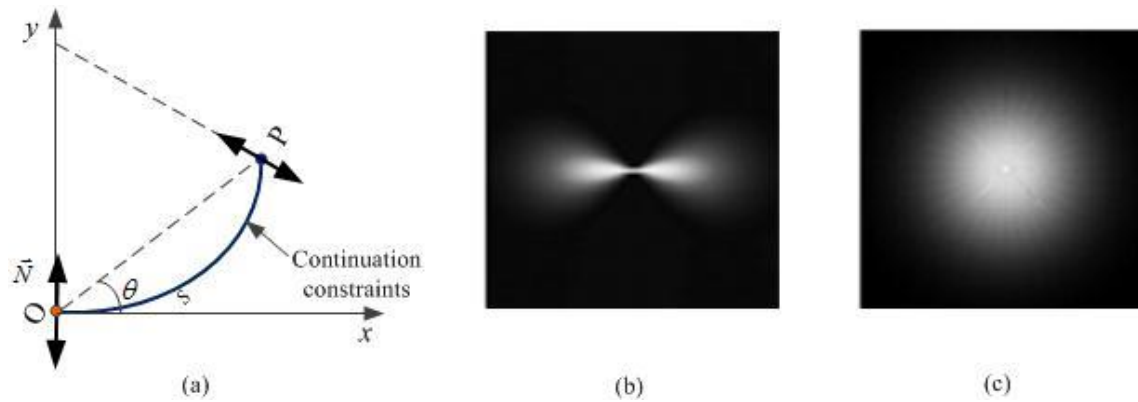
Figure 2.5: Tensor vote generation, (a) Design of fundamental 2D stick voting field, (b) magnitude (saliency) of the fundamental 2D stick voting field, (c) magnitude (saliency) of the 2D ball voting field.

(3) Voting Analysis

Each input collects all the votes cast from the tensors in its neighborhood and integrates them into a new tensor, eventually revealing behavioral coherence among image primitives. Vote accumulation is performed by tensor addition, a summation of 2x2 matrices in 2D. For example, the resulting tensor at P can be represented by

$$T_P = \sum T_O V(P) \tag{2.21}$$

where T_P is the summation tensor by accumulating all the votes $V(P)$ from its neighbors T_O at location O. Thus, after votes cast from tensor to tensor and being accumulated by tensor addition, the new tensor at P is generated for structure extraction. Then the tensor can be decomposed into the stick and ball components, as represented in Eq. (2.16). If $\lambda_1 - \lambda_2 > \lambda_2$, this indicates certainty of one normal orientation, therefore the token most likely belongs to a curve which has the estimated normal at that location. If $\lambda_1 \approx \lambda_2 > 0$, the dominant component is the ball tensor and there is no preference of orientation, either because all orientations are equally likely, or because multiple orientations coexist at the location. This indicates either a token that belongs to a region, which is surrounded by neighbors from the same region from all directions, or a junction where two or more curves intersect and multiple curve orientations are present simultaneously. Junctions can be discriminated from region tokens since their saliency is a distinct, local maximum of λ_2, whereas the saliency of region inliers is more evenly distributed. An outlier receives only inconsistent votes, so both eigenvalues are small.

Regarding the receiver containing a token or not, there are two terms: sparse voting, which describes a pass of voting where votes are cast to locations that contain tokens only, and dense voting, which describes a pass of voting from the tokens to all locations within the neighbourhood regardless of the presence of tokens. Receivers accumulate the votes cast to them by tensor addition.

2.4 Chapter Summary

This chapter first reviewed MLS technology, including a description of main components of a typical MLS system, a statement of current commercial MLS systems,

an analysis of geo-referencing and scanning parameters, a discussion of systematic and random error analysis.

A variety of current existing methods developed for extracting road surfaces, road markings, and cracks from MLS data were reviewed and analyzed, respectively. Through literature review, road and data characteristics for road-surface extraction would be explored in the next chapter; MLS intensity data will be used for the extraction of road markings in Chapter 5; the geometric and intensity information of MLS data will be combined for crack extraction in Chapter 6.

A description of the fundamental algorithms (i.e., Otsu's method, morphological operation, and tensor voting) for extracting road markings and pavement cracks was detailed. These algorithms will be developed into the algorithms to be developed for road-information extraction in the following three chapters.

Chapter 3 Methodology of Road Information Extraction

This chapter provides an overview of three algorithms for the automated extraction of road surfaces, road markings, and pavement cracks from MLS data in Section 3.1. A RIEGL VMX-450 system and its MLS data are described in Sections 3.2 and 3.3. Section 3.4 provides a summary of this chapter.
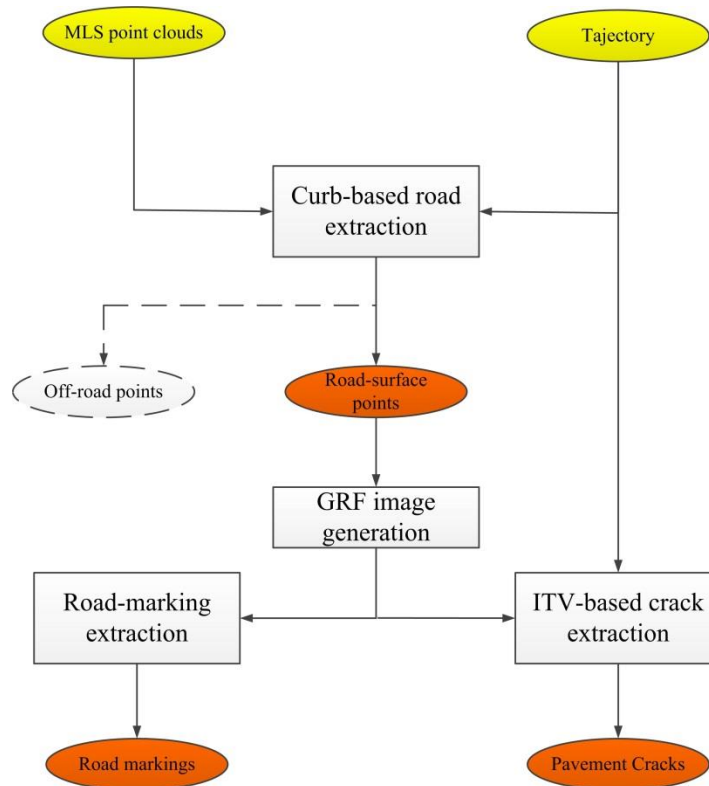
3.1 Method Framework

Figure 3.1: An overview of the method framework.

In this research the following three road information extraction algorithms are developed for road surfaces, road markings, and pavement cracks, as shown in Figure 3.1. The input to the developed road information algorithms is unorganized MLS point clouds

and trajectory data. The output includes groups of road surface points, road markings, and pavement cracks. The processes of road information are applied as follows:

- Curb-based road-surface extraction (Chapter 4)

- GRF image Generation (Chapter 5.1.2)

- Road-marking extraction (Chapter 5)

- ITV-based crack extraction (Chapter 6)

The stepwise road-surface extraction algorithm includes data profiling, pseudo scan-line generation, curb detection, and road-edge spline interpolation. The aim of the algorithm is to separate road-surface points from off-road points using the trajectory data. Vehicle trajectory data are first used to partition MLS data into a number of data blocks with a certain block length. Next, a thin profile is sliced for each block, within which all points are projected on the plane perpendicular to the line of travel to form a profile image. To detect curbs, each profile image is resampled and a pseudo scan-line is generated with a given point space. Based on slope and elevation difference, curbs are subsequently detected for finally cubic spline interpolation. With smoothed road edges, road points are separated from non-road points.

The GRF image generation algorithm aims to interpolate the extracted road-surface points into 2D GRF images, which facilitate the following road-marking and crack extraction algorithms.

The road-marking extraction algorithm involves curb-based road-surface extraction, GRF image generation, point-density-dependent multi-thresholding segmentation, and morphological closing operation. Based on the generated GRF image of road surface points, a point-density-dependent, multi-thresholding segmentation

algorithm is proposed to dynamically obtain multiple, optimal thresholds for segmenting road markings, followed by morphological operations for extracting road markings.

The ITV-based crack extraction algorithm is still based on the 2D GRF image. The ITV algorithm is developed to enhance cracks from the noisy GRF image. After that, a morphological thinning is used to extract the enhanced cracks.

3.2 RIEGL VMX-450 System

This research uses the data collected by a RIEGL VMX-450 system. The system comprises two Riegl VQ-450 laser scanners, four CCD cameras, and a set of Applanix POS LV 520 processing system containing two GNSS antennas, an IMU, and a DMI. Integrated with POS Computer System (PCS), these components are integrated and fixed within a case and mounted on the roof of a vehicle, as shown in Figure 3.2. The accuracy of the resultant position and orientation information largely determines the overall performance of RIEGL VMX-450.

The navigation solution in RIEGL VMX-450 uses two dual-frequency GNSS antennas, referred to as a primary receiver and a secondary receiver. Both receivers provide raw GNSS satellite observable information to POS LV computer system. The secondary receiver is used by the GAMS for heading aiding. Its data are used in conjunction with the information from the primary receiver for GAMS heading calculations.

In Figure 3.3, RIEGL VMX-450 uses two rotating scanning head laser scanners; thus, the scanned data of two scanners are slant grid-like pattern. The scanned data are complemented by the camera system that includes four color digital cameras. According

to the pulse per second (PPS) from the primary GNSS receiver, the scanned data and image data are synchronized with position and orientation information by POS LV 520 system.

Figure 3.2: RIEGL VMX-450 system with an inset picture of the laser scanning and navigation system mounted on the roof rack.
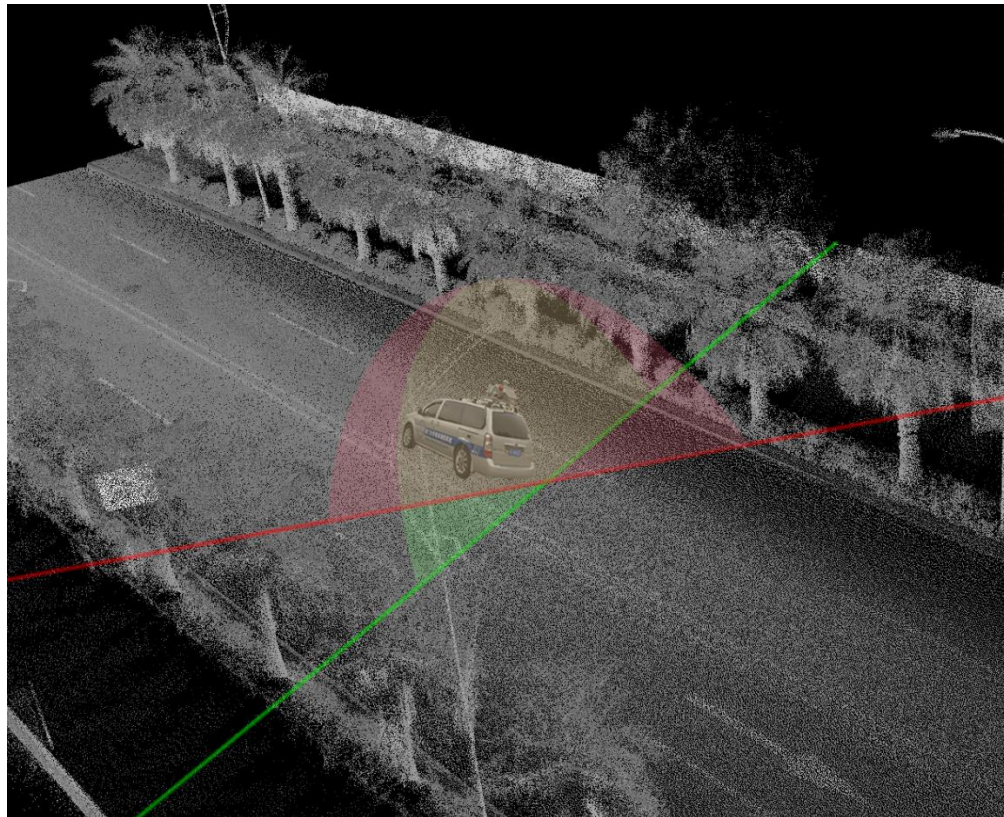

Figure 3.3: The scanning pattern.

3.3 Study Area and MLS Data

The surveyed area is within Xiamen Island (longitude 118 °04' 04" E, latitude 24 °26' 46" N), a part of the City of Xiamen, which is a major city on the southeast coast of China (see Figure 3.4). Besides of Xiamen Island, Xiamen City includes Gulang Islet, and part of the rugged mainland coastal region from the left bank of the Jiulong River in the west to the islands of Xiang'an in the northeast. On Xiamen Island, there are two districts: Huli and Siming (encompassing Gulang Islet). A complete survey was carried out back and forth on Huandao Road from Xiamen University to International Conference and Exhibition Center (ICEC). The total distance for one direction survey was around 10 km. This is a two-side, four-lane road with a greenbelt in the middle. Many high buildings, big trees (e.g., Sago cycas, palm) and shafts (e.g., light poles and traffic poles) are along the sides of the road. A part of the surveyed data were selected with straight and curve roads as the test dataset for examining the proposed algorithms. The surveyed Huandao Road, called a golden costal line, is a busy seaside green-corridor for tourism, sightseeing, leisure and recreation; as a result, moisture weather and excessive loading cause a number of cracks spreading along the road.
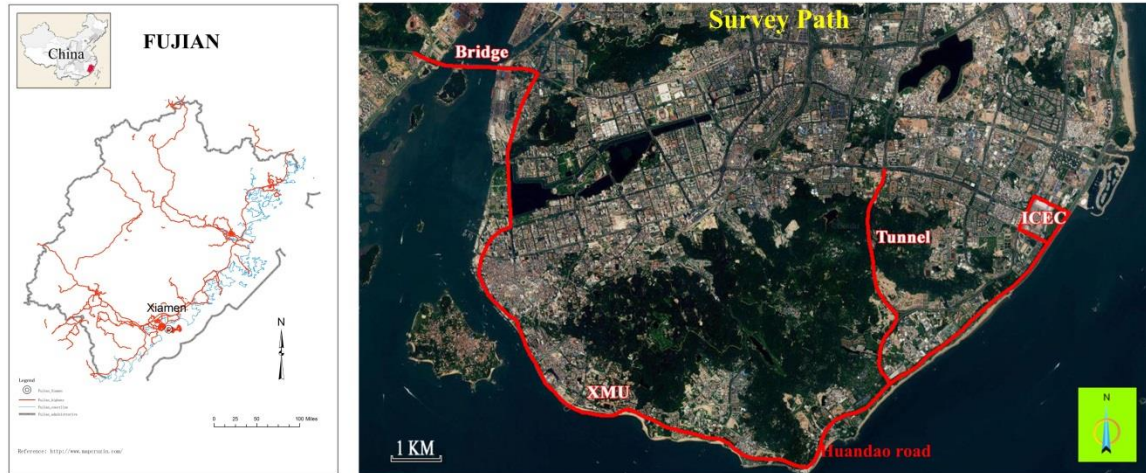
Figure 3.4: Study areas, located in Xiamen, Fujian, China.

The data were acquired on 23 April 2012 by a RIEGL VMX-450 system. As mentioned in the previous sections, the vehicle trajectory immediately affects the quality of the collected MLS point clouds. However, for a MLS system, a navigation solution has to be even more sophisticated because various obstacles on the ground, such as trees, high-rise buildings, and bridges, create periods of GPS, when satellite signals are not available to aid the navigation solution. In general, at least four satellites in view with the Positional Dilution of Precision (PDOP) = 6 or lower are required for the standard positioning service (Langley, 1999).

Actually, GPS accuracy varies with locations and the time of day. Especially in urban canyon, we may in fact not even have four satellites in view and the PDOP values may be greater than 6. The variability of actual GPS accuracy from place to place and time to time is dominated by the effects of DOP. In Figure 3.5 (a), the PDOP values during the survey are mainly under 4, and fluctuate around the value of 2.5. The corresponding number of satellites ranges from 6 to 10, as seen in Figure 3.5 (b). When the number of satellites is 5 at the GPS time of 374 000, the PDOP value is up to 6, and

55

the positioning accuracy decreases from 1.0 cm to 2.1 cm. While at the GPS time of 380 000, the vehicle was driving through an overhanging bridge, leading that the PDOP values could not be calculated, and the corresponding positioning accuracy also decreases dramatically, as shown in Figure 3.5 (c). Particularly, heading positioning errors increase by 2.0 cm and reach up to 3.8 cm. Although the positioning accuracy drops down about 2 cm when satellite signals are completely blocked, the GPS accuracy still can meet the positioning requirements for urban surveying. This is because of Applanix POS LV 520, a special solution to employ auxiliary sensors and advanced data processing solution to maintain accuracy during periods of GPS outages.

This complete survey was carried out once in a forward direction and once in a backward direction along Huandao road, thus the collected data are an integration of the data collected from four scanners (Forward direction- two RIEGL VQ-450 scanners; backward direction- two RIEGL VQ-450 scanners). Due to the existing errors analyzed in Section 2.4, there are discrepancies between the data collected from four scanners. To ensure the collected data suitable for road-information extraction, the data accuracy of the integrated point clouds is investigated.
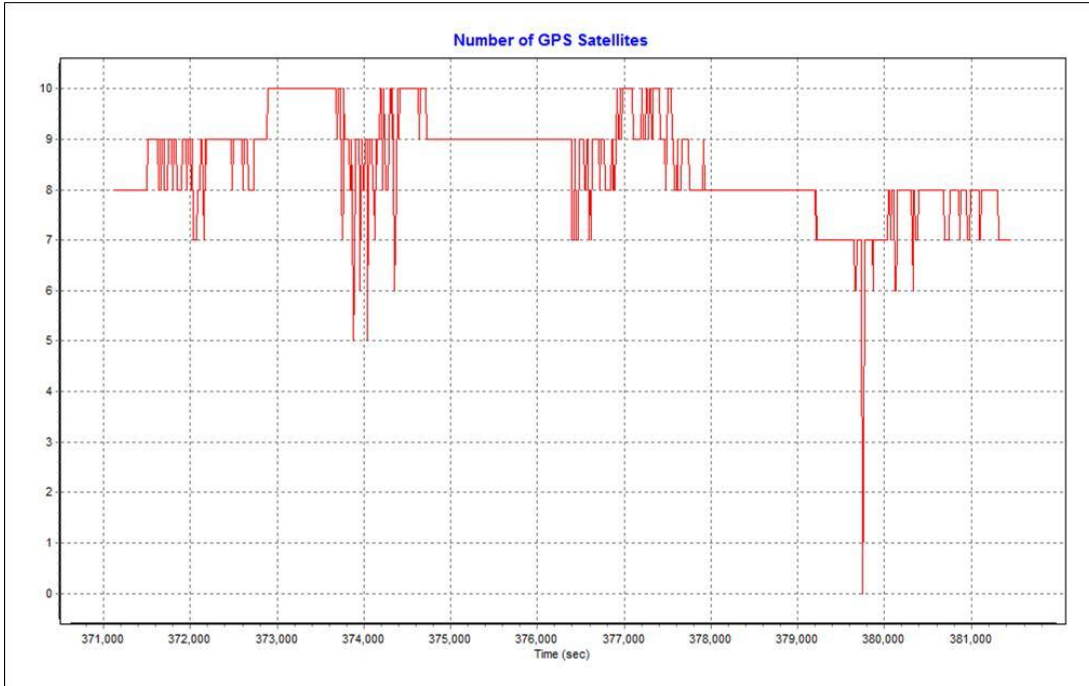
(a)
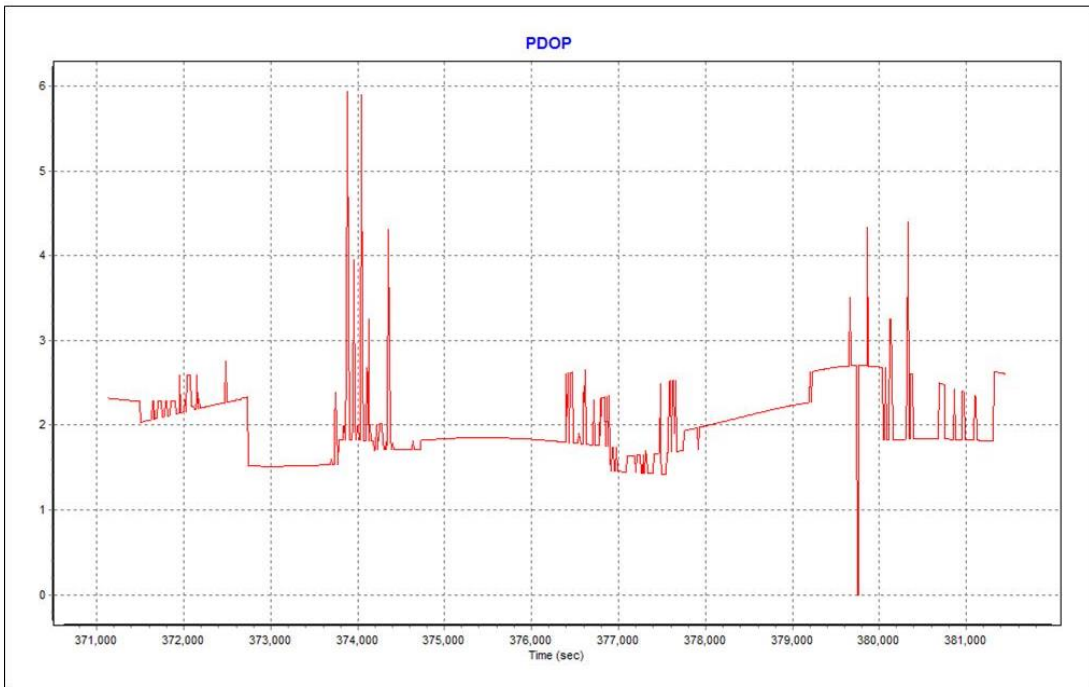
(b)
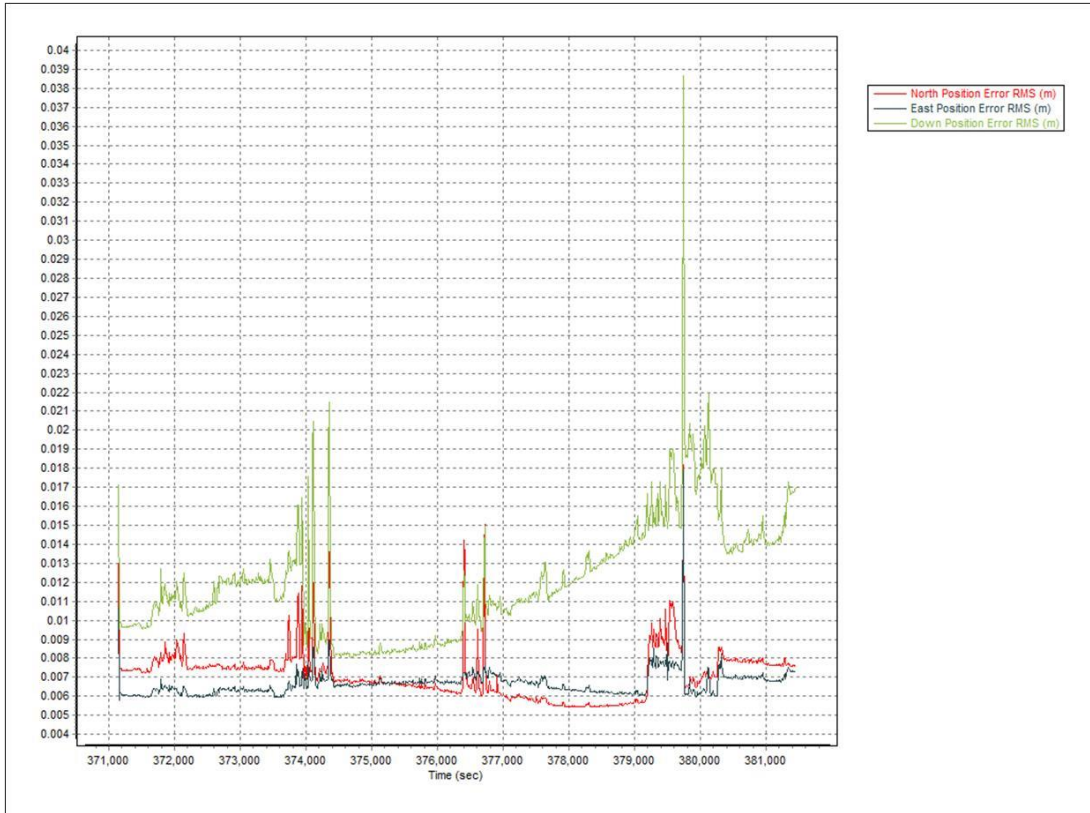
(c)

Figure 3.5: The accuracy plots of the Navigation solution: (a) the number of satellites in view, (b) the PDOP value, and (c) accuracy of GPS data in roll, pitch, and heading.

Assuming that a road within a small local area is flat, road data within a small rectangle are selected to calculate the elevation precision. The local precision can be determined by evaluating the residuals following a least square of the MLS points to the plane. For example, the yellow points shown in Figure 3.6 (a) are fitted to a plane and individually calculated the distance to the plane based on the plane parameters. As shown in Figure 3.6 (a), the minimum standard deviation is 1.477 mm, and the maximum standard deviation is close to 2 mm.
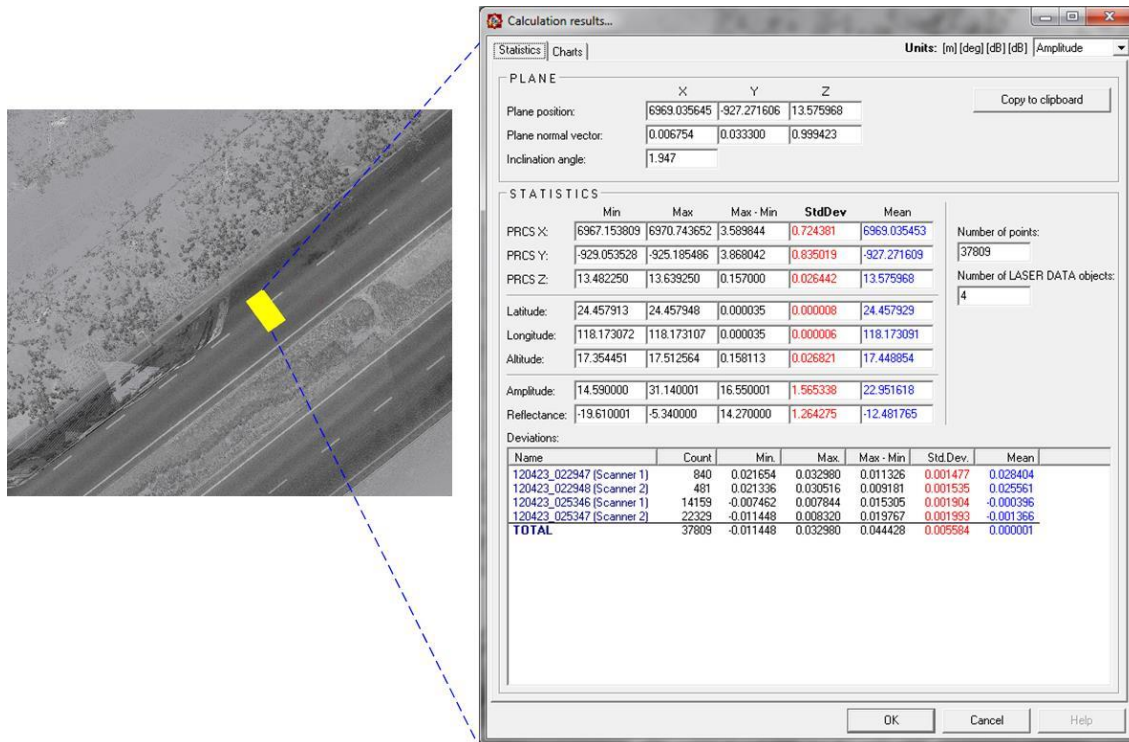
(a)

(b)

Figure 3.6: Precision of the collected MLS point clouds, (a) vertical, and (b) planimetric.

Similarly, the data on a vertical advertising board attached to a light pole are selected for the assessment of planimetric precision of the collected point clouds, as shown by the yellow points in Figure 3.6 (b). Compared to the elevation precision, the planimetric precision is a little lower; the standard deviation ranges from around 7 - 11 mm. For common transportation applications, the 3D accuracy at 95% confidence generally requires a range of 1 cm (e.g., engineering survey, DEM, pavement survey, and slope stability) to 10 cm (e.g., urban modeling and roadway condition assessment) based on the information from literature review, questionnaire, and project team experience. Thus, the data collected by a RIEGL VMX-450 system are sufficient for the transportation-related road features in both horizontal and vertical precision.

To evaluate the overall performance of RIEGL VMX-450, a set of reference data that are at least one level more accurate than the system being tested was newly collected. For example, aerial photography is often used to assess the accuracy of maps made from moderate-resolution satellite imagery (Congalton and Green, 2009). 30 reference coordinates were measured by RTK GPS at corner points of white road markings by Leica, Xiamen Staff. With those points, the performance of RIEGL VMX-450 was assessed. Most cases select corner points of objects on the street and white road markings that could be conveniently identified in the point clouds for accuracy assessment. Those points were post-processed regarding a base station with a mean base-line length of less than 6.0 km.

As shown in Table 3.1, the mean standard deviation of planimetric accuracy for the left and right laser scanners is 4.2 cm and 3.3 cm respectively. The mean standard deviation of vertical accuracy for two laser scanners is 1.7 cm and 2.1 cm, respectively.

Notice that the minimum standard deviation appears at the check points measured near the base station with a good GPS coverage. In spite of errors of check points, the accuracy of MLS points is still consistent to the accuracy of the navigation system and even outperforms the Applanix's specification. The errors are lower than ±5 cm, and meet the requirements of data accuracy for urban surveying.

Table 3.1: Positional accuracy of Laser Scanners.

	Mean standard deviation		Minimum standard deviation		Maximum standard deviation	
	Left laser scanner	Right laser scanner	Left laser scanner	Right laser scanner	Left laser scanner	Right laser scanner
Elevation accuracy (cm)	1.7	2.1	0.8	0.7	1.9	2.5
Planimetric accuracy (cm)	4.2	3.3	2.5	2.3	5.7	4.9

During this survey, two types of parameters are pre-defined, which include mission and scanner parameters. The mission parameter category includes target distance and ground speed. The surveyed Huandao road was pretty busy, the average driving speed ranged from 30 ~50 km/h. The buildings (e.g., high-rise residential apartments and commercial buildings) are located along this typical urban road. Thus, this survey kept 30 m and 30 km/h for the target distance and ground speed. As for scanner parameters, this survey used the default values for all parameters, such as the scan mode (line), scan-line start, end and increment angles (0 °, 360 °, 0.1143 °). Thus, according to Eqs.(2.2) - (2.5), at the vehicle speed of 50 km/h, the scan speed, line distance, point distance, and average point density are estimated as 200 lines/s, 0.0583 m, 0.0598 m, and 286.44 points/m^2 , respectively. The point density for MLS data strongly relies on the nominal distance to the target where the point spacing is measured as well as the incidence angle. The point

density can be also determined by dividing the number of MLS points on the plane by the total area. For example, a RIEGL VMX-450 system, at the driving speed of 30 km/h, can collect ~7,000 points/m^2 on the road surface within the range of 2.5 m, a much lower point density of 1,600 points/m^2 on the pavements 20 m away from the scanning centre, as shown in Figure 3.7. Such high point density can meet the requirement of road-information extraction for transportation applications.
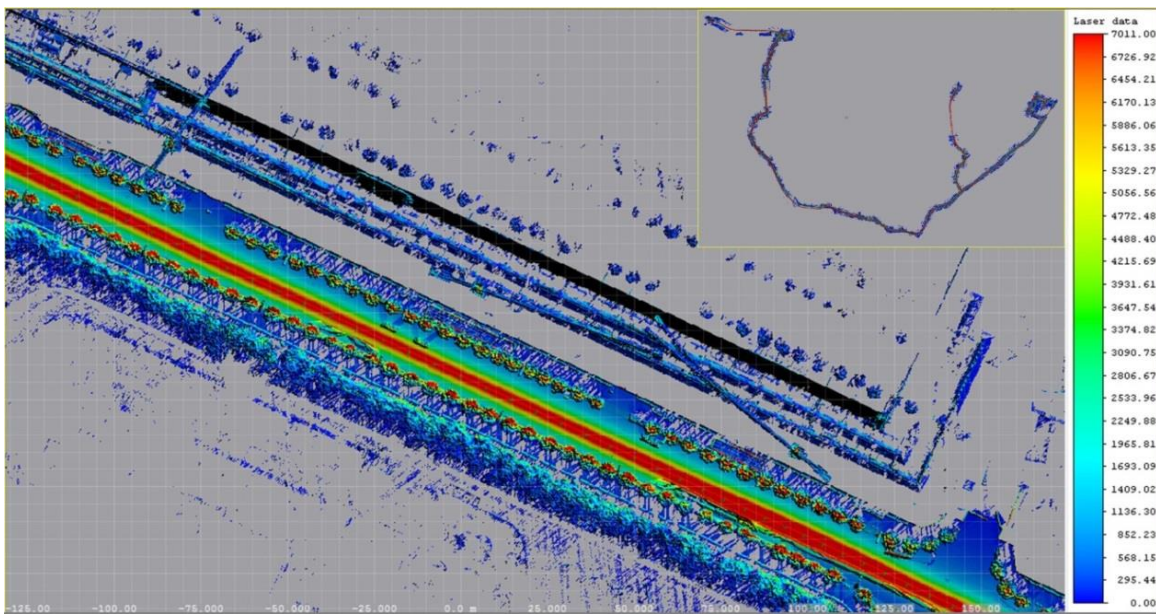

Figure 3.7: Point density distribution of RIEGL VMX-450 data.

3.4 Chapter Summary

This chapter first provided an overview of road information extraction algorithms. Second, a RIEGL VMX-450 system used in this research was introduced. Finally, MLS data collected from RIEGL VMX-450 were subsequently discussed in accuracies of the navigation solution and laser scanner.

Chapter 4 Curb-based Road Surface Extraction[1]

This chapter presents the algorithm for the automated extraction of road surface from the MLS data. Validation is presented in Section 4.2. The conducted tests are described and analyzed in Section 4.3. Discussions are presented in Section 4.4, and Section 4.5 provides a summary of this chapter.

4.1 Algorithm Description

Based on the assumption that curbs are road boundaries that separate pedestrian pavements or other green spaces from road surfaces, a curb-based road-surface extraction algorithm is designed with the assistance of vehicle trajectory. The vehicle trajectory that records the real-time positioning information of the vehicle facilitates road-surface detection. The proposed road-surface extraction algorithm is composed of four steps, as shown in Figure 4.1:

(1) "Data profiling"- based on the trajectory, MLS data are partitioned into a number of data blocks, in each of which a thin profile is sliced.

(2) "Pseudo scan-line generation"- all points in the profile are projected onto the plane perpendicular to the line of travel as a profile image. The profile image is then gridded and a principal point is selected for each grid to form a pseudo scan-line.

---

[1] The main work presented in this chapter has been submitted by: Guan, H., Li, J., Yu, Y., Chapman, M., and Wang, C. 2013. Automatic Road Information Extraction Using Mobile Laser Scanning Data. *IEEE Transactions on Intelligent Transportation Systems* (Submitted Nov. 04, 2013, under the 2nd round review).
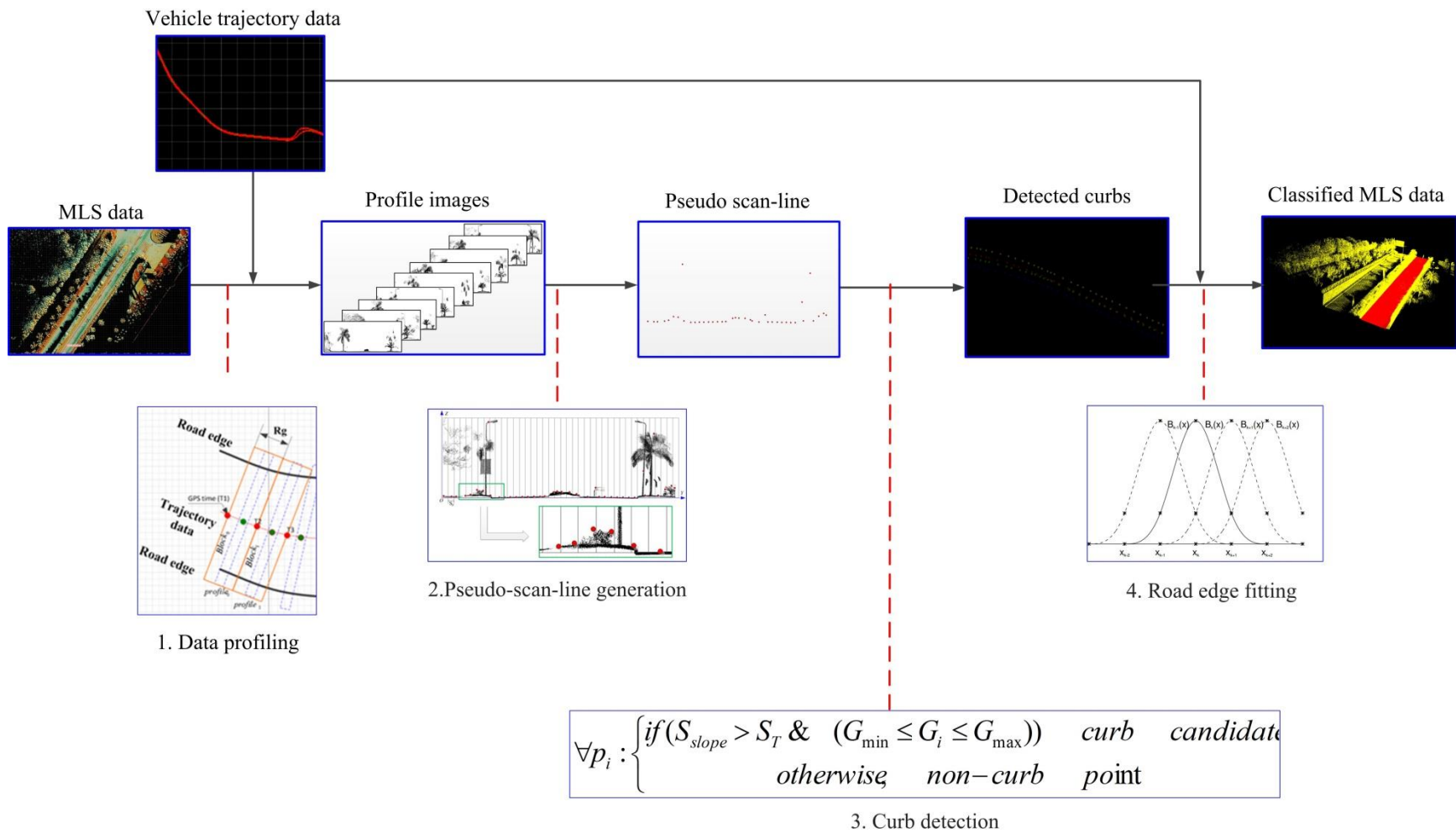
Figure 4.1: An overview of the proposed road extraction algorithm.

Vehicle trajectory data

MLS data

Profile images

Pseudo scan-line

Detected curbs

Classified MLS data

Road edge

Rg

Trajectory
data

GPS time (T1)

Road edge

1. Data profiling

2. Pseudo-scan-line generation

$$\forall p_i : \begin{cases} if(S_{slope} > S_T \ \& \ (G_{min} \leq G_i \leq G_{max})) & curb \quad candidate \\ otherwise, \quad non-curb \quad point \end{cases}$$

3. Curb detection

4. Road edge fitting

(3) "Curb detection"- curbs are detected from each pseudo scan-line using the elevation difference and slope criteria.

(4) "Road edge fitting"- Curbs detected from all pseudo scan-lines are further fitted into two smooth road edges via a cubic spline interpolation to separate road points from off-road points.

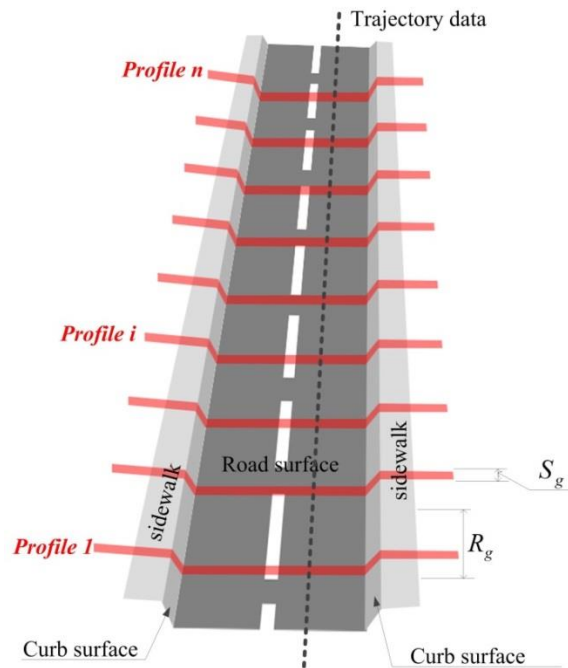### 4.1.1 Trajectory-based Data Profiling

Figure 4.2: An illustration of trajectory-based data profiling.

A vehicle trajectory, a path that a moving vehicle follows along the road as a function of time, is recorded by the integrated navigation solution while flight-of-time measurements are performed by two laser scanners. The GPS base station observations, together with the raw GNSS and inertial data are then processed in the Applanix POSPac^{TM} MMS software. Applanix's unique post mission aided inertial processing package produces the Smoothed Best Estimate of Trajectory (SBET, hereafter referred to

as trajectory). The vehicle trajectory and the predetermined calibration parameters are then used to produce geo-referenced point clouds.
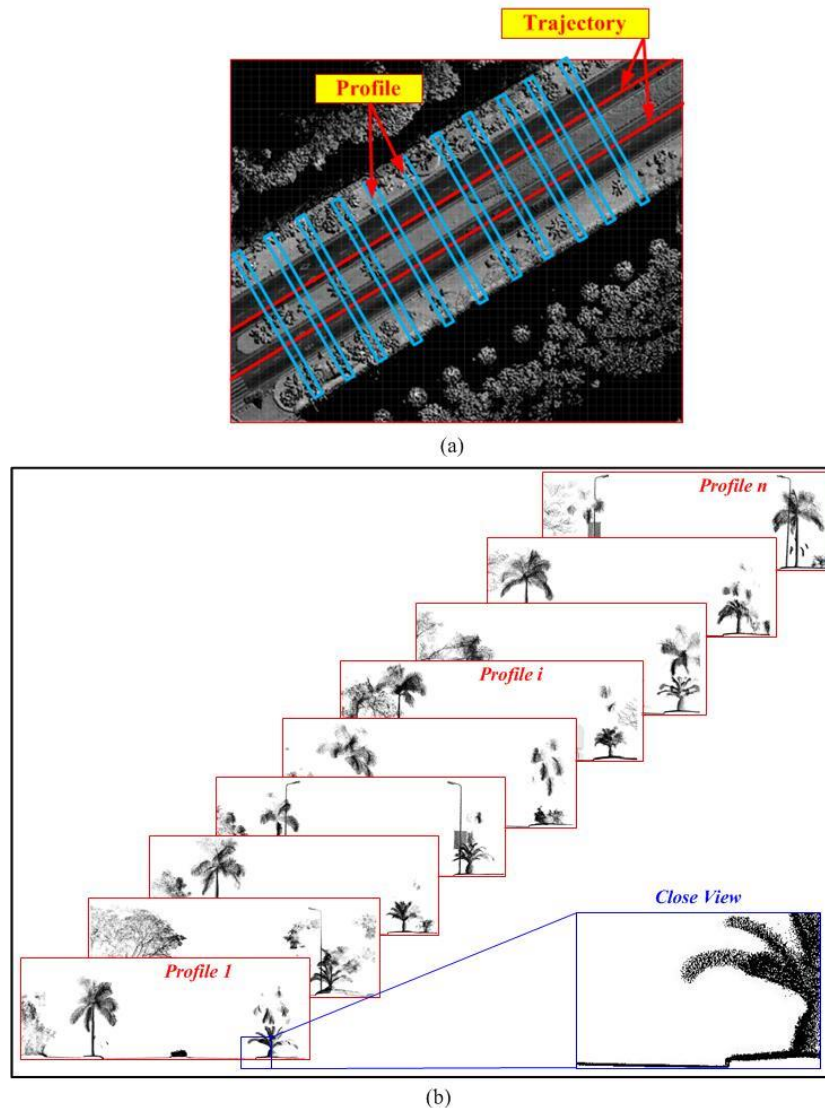

(a)

(b)

Figure 4.3: A set of profiles sliced from their corresponding data blocks: (a) a profiling process demonstrated on the real MLS data sample, and (b) a number of profiles.

Perpendicular to the vehicle trajectory, the scanned point clouds are first partitioned into a number of data blocks with a given length (R_g). A profile is then sliced for each data block with a given width (S_g). Hence, each profile has points pertaining to road surfaces and points pertaining to objects beyond the road surfaces, such as trees, cars,

and curbs. As shown in Figure 4.2, red rectangles represent profiles. Two parameters, the profile width and the block length, will be discussed in Section 4.3. Figure 4.3 (a) shows a part of real RIEGL VMX-450 data with several profiles, represented by blue rectangles. Figure 4.3 (b) shows the profile images, on which all points for each profile are projected onto the plane perpendicular to the line of travel. A close-up view demonstrates that the curb is clearly presented on the profile image.

4.1.2 Pseudo Scan-line Generation

For RIEGL VMX-450 system in this research, the vehicle frame is defined as the right-handed orthogonal coordinate system with its origin at an arbitrary, user-defined point. The orientation of the vehicle frame is fixed so that the x-axis is towards the front of the vehicle, the y-axis is towards the right of the vehicle, and the z-axis is towards the bottom of the vehicle. Figure 4.4 shows a profile image by projecting all points within the profile onto the YoZ-plane in the vehicle frame. Two close-up views demonstrate that the curbs, vertical or nearly vertical to the road surface, are sharp height jumps; therefore, curbs can be estimated by slope and elevation-difference thresholds, and road points can be finally separated from off-road points.

To this end, each profile is first gridded to form a pseudo scan-line with a cell size of S_p, also termed as point spacing. The point spacing of a pseudo scan line (S_p) depends on the point density of MLS data within the experiments. For example, RIEGL VMX-450 has an average point density of about 300 points/m² Each cell has over 4 points when the proposed algorithm keeps the profile width $S_g = 25$ cm and the cell size of $S_p = 5$ cm.

Second, a sampling is taken for each grid cell to select a principal point, as shown in Figure 4.5. To determine the principal point within a grid cell, a Quick Sort algorithm is used to sort all the points within the grid cell in elevation. Next, from the lowest point, the elevation differences $\Delta L_j (j = 1,2,3,..., N)$ of two consecutive points are calculated to group them into different layers. N is the number of the points in a grid cell. The two consecutive points are labelled into a same layer if only if the elevation difference lies below a pre-defined threshold, that is, $\Delta L_j < L_T$. Otherwise, a new layer is created to separate these two points. Usually, L_T is given 5 cm. Assume that points belonging to road surface are within the lowest layer. With this assumption, principal points within each grid are determined by selecting the point with the highest elevation within the lowest layer, as shown in Figure 4.6. With this scheme, most outliers such as tree points over the road can be removed. Those extracted points are then re-organized into a pseudo scan-line which maintains road points and critical road features with fewer disruptive noises, as shown in Figure 4.7.
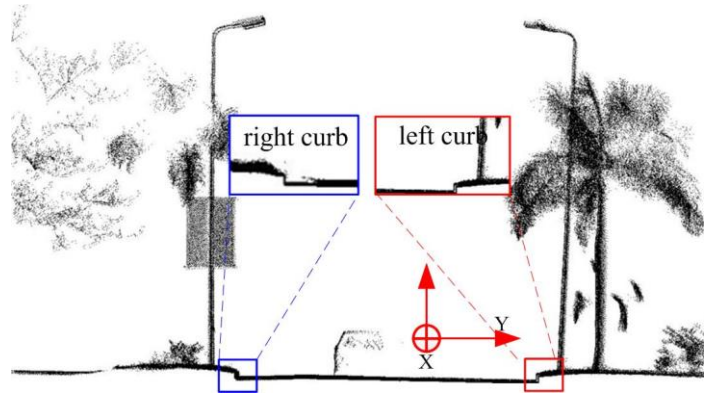

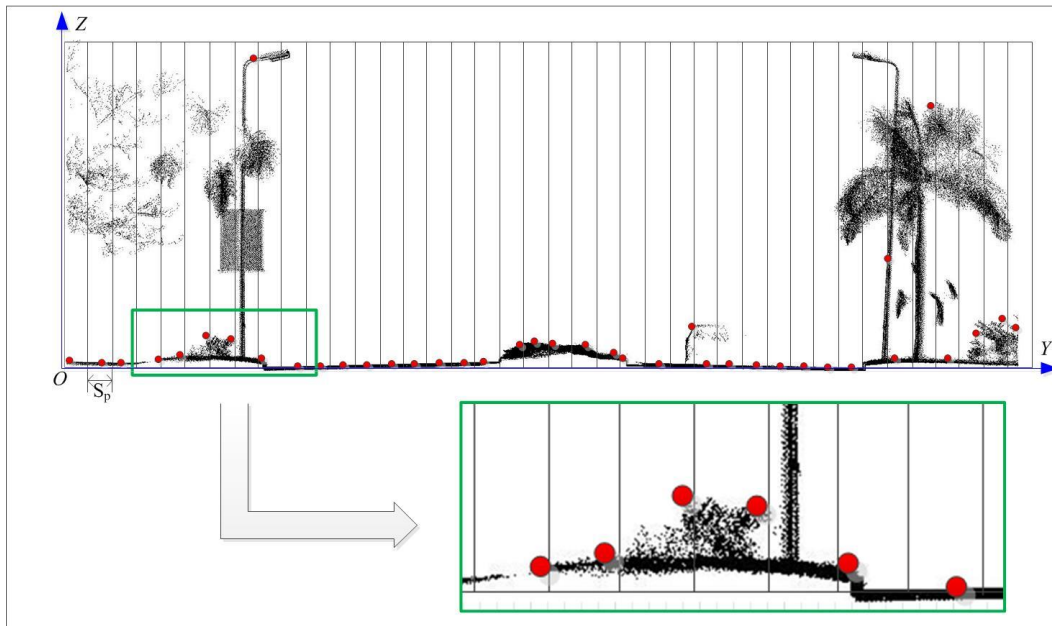Figure 4.4: Curb observation in a profile image-all points projected onto the YoZ-plane.

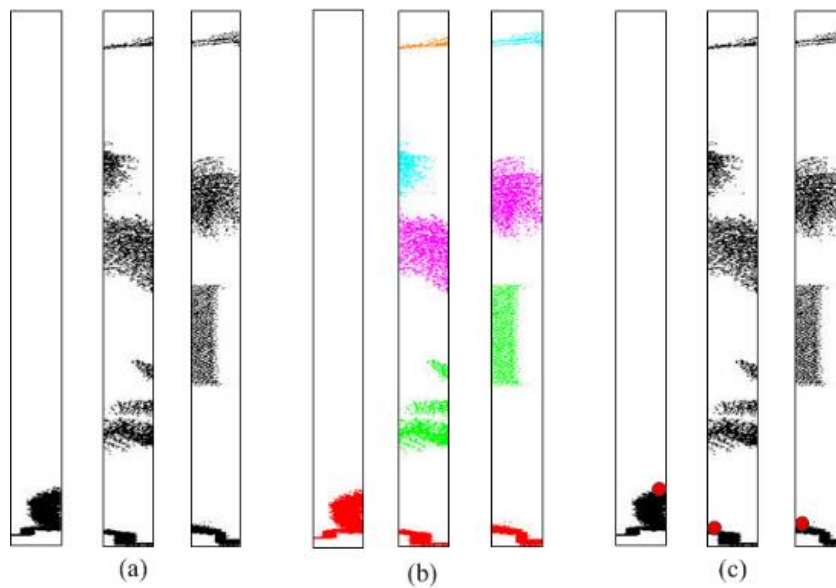Figure 4.5: A profile sample gridded to find principal points.

Figure 4.6: Selection of principal points: (a) Three grid cells of a profile, (b) layered points (different colours represent different layers), and (c) selected principal points.
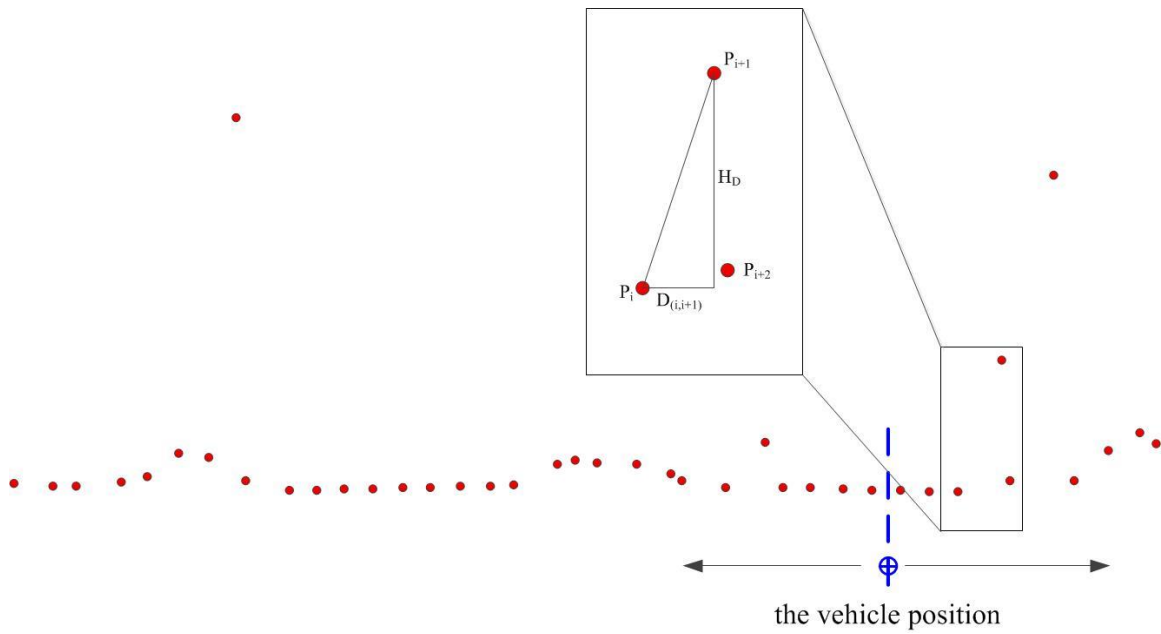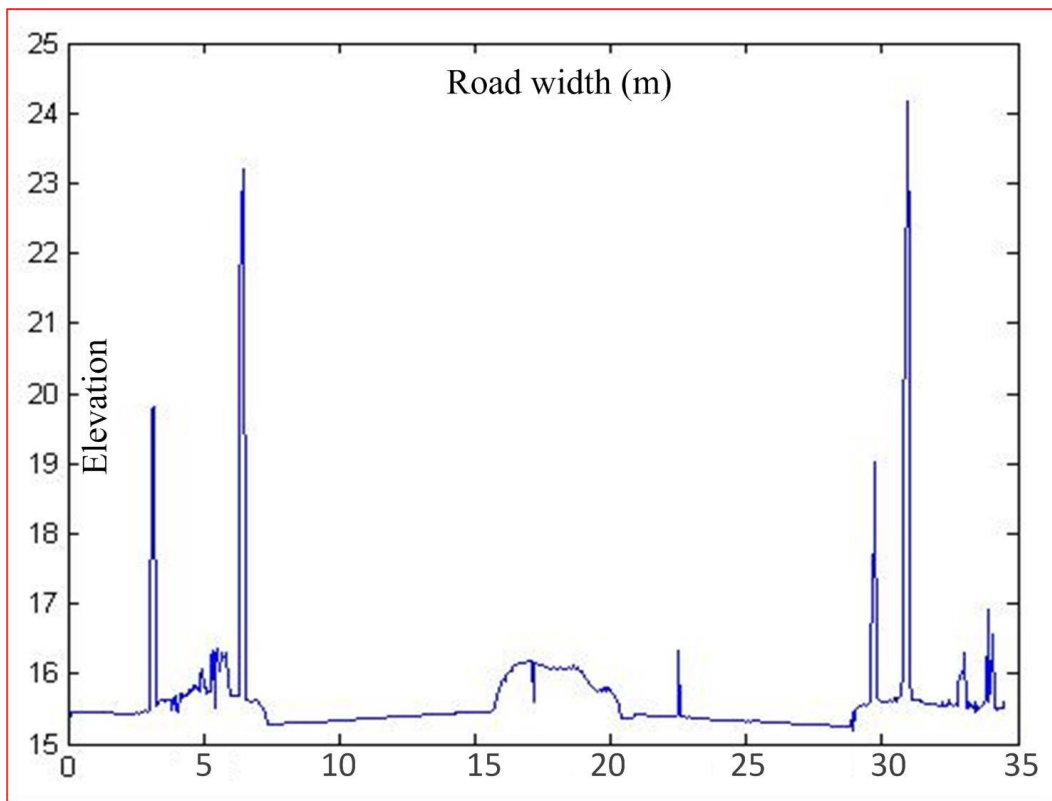
Figure 4.7: A pseudo scan-line generated from a profile image.

(c)

Figure 4.8: A pseudo scan-line presented by slope.

4.1.3 Curb Detection

In this study, the algorithm for curb detection is based on both slope and elevation evaluation and implemented at the scanning center in two opposing ways, as shown in Figure 4.7. The proposed curb-based road extraction algorithm mathematically defines the slope between two consecutive points in a generated pseudo scan-line (See Figure 4.8) and the elevation difference of a point relative to its neighborhood in the scan-line. Assume that slopes at the border of pavement and roadway are usually larger than those of the continuous points on the roadway. Moreover, pavement points have larger elevations than road points in the neighborhood. These two criteria are used to detect whether or not a point is a curb. First, the slope criterion detects off-road points, such as car and curb points. Second, the elevation difference criterion detects the curb corners from the off-road points. According to street design and construction manuals in many countries, heights of curbs generally range between 10 cm and 20 cm. These two observations are mathematically defined as:

$$\forall p_i : \begin{cases} if\ (S_{slope} > S_T\ \&\ \ (G_{min} \le G_i \le G_{max})) & curb \quad candidate \\ otherwise, \quad non-curb \quad po\mathrm{int} \end{cases} \quad (4.1)$$

where, S_{slope} denotes the slope of two consecutive points. S_T is a given slope threshold. G_i denotes the elevation difference of a point and its neighbor. G_{min} and G_{max} are the minimum and maximum thresholds. S_{slope} can be defined using the following equation:

$$S_{slope} = \arctan\left(\frac{Z_{i+1} - Z_i}{\sqrt{(X_{i+1} - X_i)^2 + (Y_{i+1} - Y_i)^2}} \right) \quad S_{slope} \in [-\tfrac{\pi}{2}, \tfrac{\pi}{2}], \quad (4.2)$$

where, (X_i, Y_i, Z_i) and ($X_{i+1}, Y_{i+1}, Z_{i+1}$) are the coordinates of two consecutive points in a pseudo scan-line with Z coordinate pointing to the elevation direction, and X and Y coordinates lying on the YoZ-plane.

According to Figure 4.7, Eq.(4.2) is represented as:,

$$S_{slope} = \arctan\left(\frac{H_D}{D_{(i,i+1)}}\right) \quad S_{slope} \in [-\tfrac{\pi}{2}, \tfrac{\pi}{2}] \tag{4.3}$$

Note that Eq. (4.3) can take both positive and negative signs. A positive slope means point sequence entering a off-road point from road at the curb boundary while a negative slope represents point sequence leaving a off-road point to road at the curb boundary. The proposed algorithm starts the labelling processing from the vehicle position that is definitely located on the road surface. In other words, the initial labelling is entering from the road into curb. Therefore, once a point p_i gets a slope S_{slope} greater than the given slope threshold S_T, it means the point reaches a possible curb. It will be labelled as a curb candidate. From all the curb candidates that include curbs or some other objects like cars over the road, their elevations are calculated to detect real curbs. If a curb candidate's elevation difference g_i at its vicinity is within the range of [G_{min}, G_{max}], the curb candidate is labelled as a curb; otherwise, it will be labelled as a non-curb point. As the survey vehicle moves along the road, with a priori knowledge of the road, the curb candidates closest to the scanning centre are selected as curbs.

4.1.4 Road Edge Fitting

All curbs detected from the profiles are sparse because MLS data are partitioned along the vehicle trajectory into a number of data blocks at a certain length. Therefore, an interpolation method is needed to generate two smooth road edges from those curb points,

and finally separate road from off-road points. The developed algorithm uses cubic spline to obtain smooth curves (road edges) using a number of extracted curb points.

Cubic spline interpolation consists of weights attached to a flat surface at the points to be connected. A flexible strip is then bent across each of these weights, resulting in a pleasingly smooth curve. Splines tend to be more stable than fitting a polynomial with the extracted curb points, with less possibility of wild oscillations between the points.

Mathematically, the essential idea is to fit a piecewise function of the form:

$$F(x) = \begin{cases} f_1(x) & if & x_1 \leq x < x_2 \\ f_2(x) & if & x_2 \leq x < x_3 \\ & \vdots & \\ f_{n-1}(x) & if & x_{n-1} \leq x < x_n \end{cases} \tag{4.4}$$

where, f_i is a third degree polynomial defined by

$$f_i(x) = a_i(x - x_i)^3 + b_i(x - x_i)^2 + c_i(x - x_i) + d_i \tag{4.5}$$

for $i = 1, 2, \ldots, n-1$.

The first and second derivatives of these n-1 equations are fundamental to this process, and they are

$$f_i^{'}(x) = 3a_i(x - x_i)^2 + 2b_i(x - x_i) + c_i \tag{4.6}$$

$$f_i^{''}(x) = 6a_i(x - x_i) + 2b_i \tag{4.7}$$

4.2 Validation

For validation, a total of 45 points were measured as references using a Leica TS15i-1/GS15 smart station that integrates a GNSS to provide the measurement accuracy at millimeter level. Positional accuracy assessment is performed in a form of root-mean

square errors (RMSE) to evaluate the performance of the developed road extraction algorithm by calculating the distances of the reference points to the extracted curb edges. For other test data, the reference points were manually selected and the distances to the extracted curb edges were calculated using the Terrasolid software suit, terrascan.

4.3 Experiments

Several parameters, values, and thresholds used in the extraction of road surfaces are listed in Table 4.1. The developed algorithm uses six parameters for road extraction. The length of a block R_g and the width of a profile S_g are used at the stage of profiling; S_p and ΔL_j at the stage of the generation of a pseudo scan-line; G_i and S_{slope} at the stage of curb detection. Thus, the automation of the road extraction algorithm is required a detailed analysis of all input parameters and their influences. According to the prior knowledge about the road, the algorithm pre-defines four thresholds L_T, G_{min}, G_{max}, and S_T, all of which have a slight impact on the performance of the proposed algorithm.

Table 4.1: Parameters in the proposed road-surface extraction algorithm.

Name	Definition	Value	Threshold
S_g	The width of a profile	To be discussed in experiments	no
R_g	The length of a block	To be discussed in experiments	no
S_p	The point spacing of a pseudo scan line	To be discussed in experiments	no
ΔL_j	The elevation difference for selecting of principal points		L_T : 5 cm.
G_i	The elevation difference for detecting curbs		G_{min}(the minimum height difference of the curb) : 8 cm, a prior knowledge; G_{max} (the mini maximum mum height difference of the curb) : 30 cm, a prior

74

			knowledge;
S_{slope}	The slope threshold for detecting curbs		$S_T : \pi/3$

Parameter R_g, the length of a block, has an impact on the performance of the road-surface extraction algorithm because it controls the size of a data block to be partitioned. That is, it decides how many blocks can be obtained for curb extraction, and how many curb points can be used for cubic spline interpolation. Parameter S_g is also critical to the proposed algorithm because it determines how many points are included for the generation of pseudo scan-lines and the presentence of curbs. Parameter S_p that controls the point spacing of the pseudo scan-lines decides the precise position of the detected curbs and the accuracy of the detected roads. Thus, three groups of experiments are designed by varying the values of parameters R_g, S_g, and S_p.

Five datasets are selected from the 2012-04-23-survey for testing the sensitivity of these parameters. The first three datasets are 25-m-long, and the other two are 50-m-long. Figure 4.9 shows the raw MLS datasets and their road extraction results.
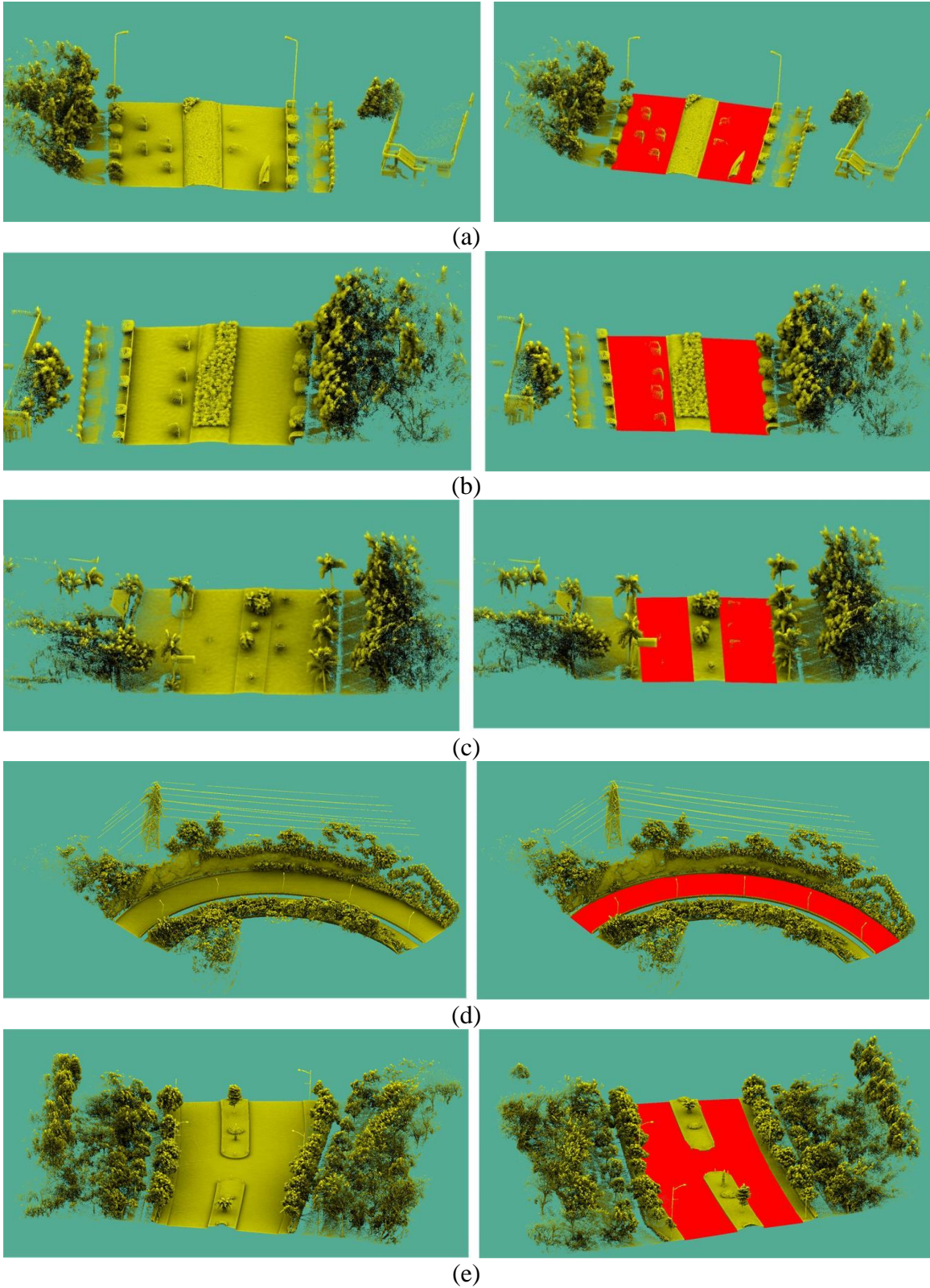
Figure 4.9: Five datasets used for the automated selection of input parameters, (a) Road 1 & its road extraction results, (b) Road 2, (c) Road 3, (d) Road 4, and (e) Road 5.

4.3.1 Analysis of Block Length

This group of experiments keep $S_g = 25$ cm and $S_p = 5$ cm, and vary R_g from 0.5 m to 5 m at six levels (0.5 m, 1.0 m, 2.0 m, 3.0 m, 4.0 m, and 5.0 m). Figure 4.10 shows the values of RMSE in horizontal and vertical accuracies at the six lengths of blocks for five test datasets. Note that the horizontal accuracies of the extracted roads are pretty stable with the block length ranging from 0.5 m to 3.0 m. However, the horizontal accuracies tend to decrease with the block length over 3.0 m. The vertical accuracies of the extracted roads have a similar tendency to the horizontal accuracies. The reason behind this phenomenon might be that with an increase of the block length, the interval of the profiles goes to be larger, and the number of the detected curbs decrease, indicating that the changes of the road could not precisely presented. Among the five datasets, the proposed curb-based road-surface algorithm achieves the worst performance for road 4 because a large curvature is presented in Road 4, which means, for a road with a large curvature, the shorter the block length is, the better the accuracy of the extracted road using the proposed algorithm. However, a straight road would be less sensitive to the block length. As seen from these five datasets, the best road could be obtained at $R_g = 3.0$ m. $R_g = 3.0$ m is used as a standard for all roads. If some roads contain turns, the algorithm can adjust the block length according to the curvature of the vehicle trajectory. For example, if a road has sharp bends, curves or turns, $R_g = 1.0$ m will be used to collect more curbs for preserving road features.
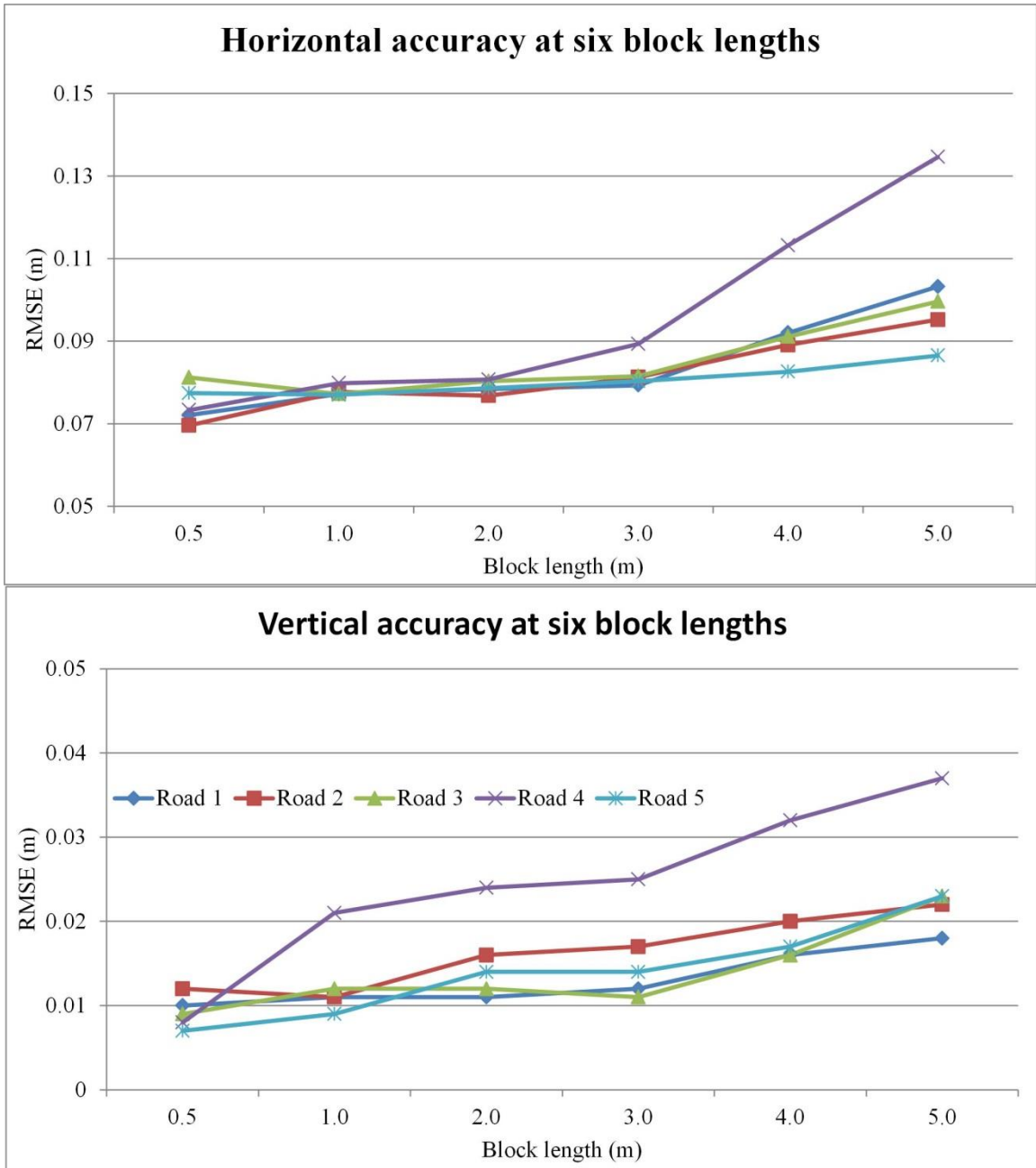
Figure 4.10: Accuracies of extracted roads at six block lengths.

4.3.2 Analysis of Profile Width

This group of experiments keep $R_g = 3.0$ m and $S_p = 5$ cm, and vary S_g from 10 cm to 100 cm at six levels (10 cm, 20 cm, 30 cm, 40 cm, 50 cm, and 100 cm). Figure 4.11 demonstrate the extracted results in horizontal and vertical accuracies.

As show in Figure 4.10, when S_g is 20 cm, the proposed curb-based road-surface algorithm achieves a stable performance with the horizontal accuracy of 7 cm and the vertical accuracy of an average of 15 cm. The accuracies decrease quickly with S_g increasing from 40 cm to 100 cm. This is because that, the thicker the profile, the more points are included to detect curbs. Too many points included for the extraction of curbs could play a negative effect on the performance of the algorithm because of the following two reasons: (1) road shape and (2) the selection of principal points at the stage of generating pseudo scan-lines. If a road is a little winded, not strictly straight, even with a smaller-angle, curbs in the thicker profile could contain more deformed points, decreasing the precise positions of curbs. Second, the thicker profile could include more points in a gridded cell for generating a pseudo scan-line, indicating that the selection of principal points for each grid could be interfered. The analysis of the five datasets shows that the best performance of the proposed extraction algorithm could be achieved at $S_g =$ 20~ 30 cm.
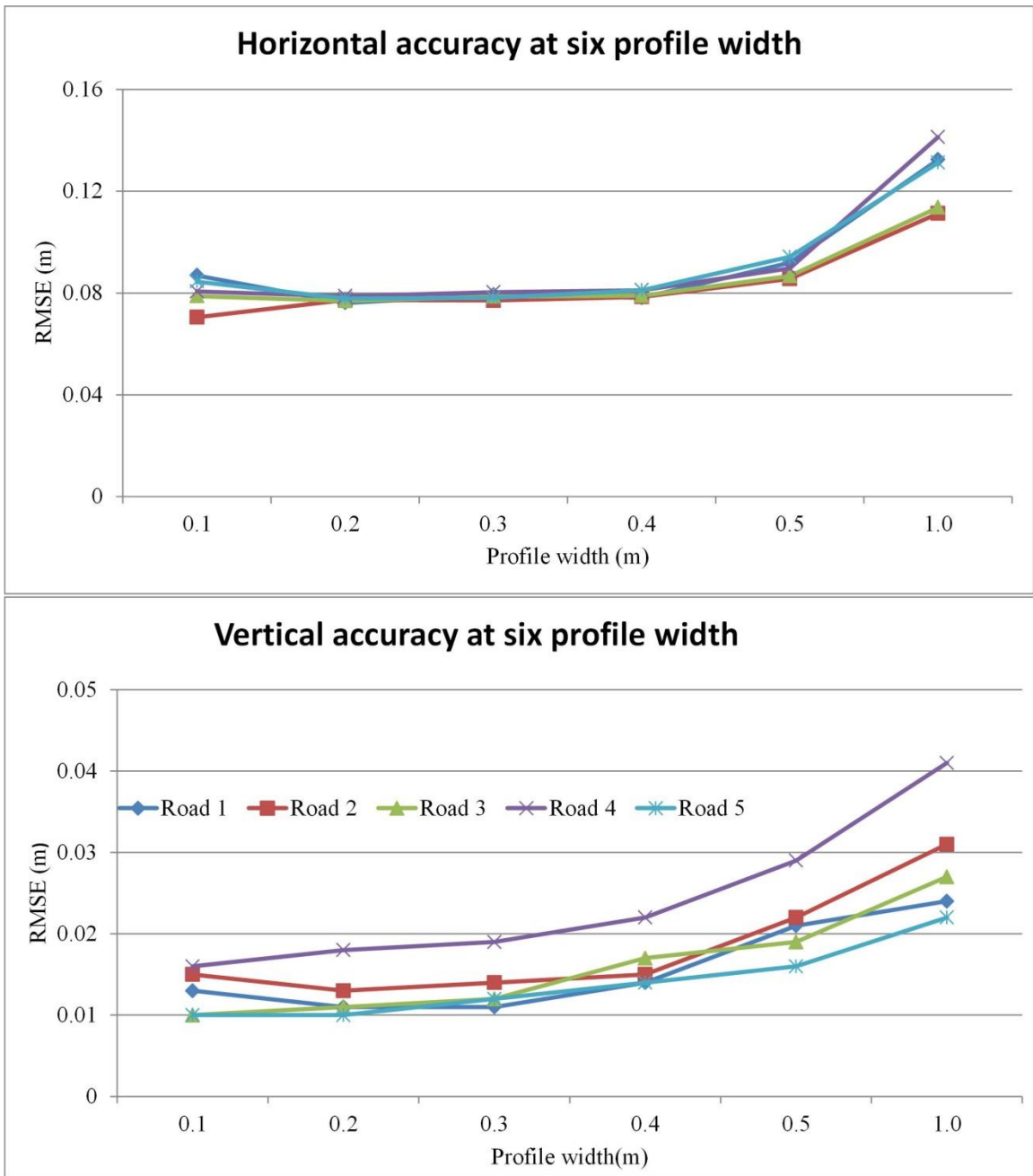
Figure 4.11: Accuracies of extracted roads at six profile widths.

4.3.3 Analysis of Grid Size

This group of experiments keep S_g = 25 cm and R_g = 3.0 m, and vary S_p from 3 to 10 cm at seven levels (3 cm, 4 cm, 5 cm, 6 cm, 7 cm, and 10 cm). The point spacing S_p determines the point resolution of the generated pseudo scan-lines. The smaller the point resolution is, the higher the accuracy of the extracted road surfaces is. However, the point density of the pseudo scan-line depends on the scanning parameters and the vehicle speed, according to the analysis in Chapter 3. For example, the scan-line-to-scan-line spacing for RIEGL VMX-450 is about 4 - 6 cm at the speed of 30 - 50 km/h. Thus, the test for the point spacing starts off 3 cm. Figure 4.12 show the horizontal and vertical accuracies of the extracted roads at seven point spacing levels. As shown in Figure 4.12, the horizontal and vertical accuracies for all roads grow with the increase of the point spacing S_p, and the algorithm shows a stable performance when S_p varies from 3 - 6 cm. The philosophy behind this phenomenon is that larger grid cells have enough points for detecting curbs. However, the horizontal and vertical accuracies quickly decrease when S_p is over 6 cm, indicating that a larger S_p can be counterproductive. Although there are adequate points for searching curbs, excessive point spacing S_p would produce a less precise positioning estimation of curbs. For this study, the developed algorithm achieves a good performance of road extraction at S_p = 4 - 5 cm.
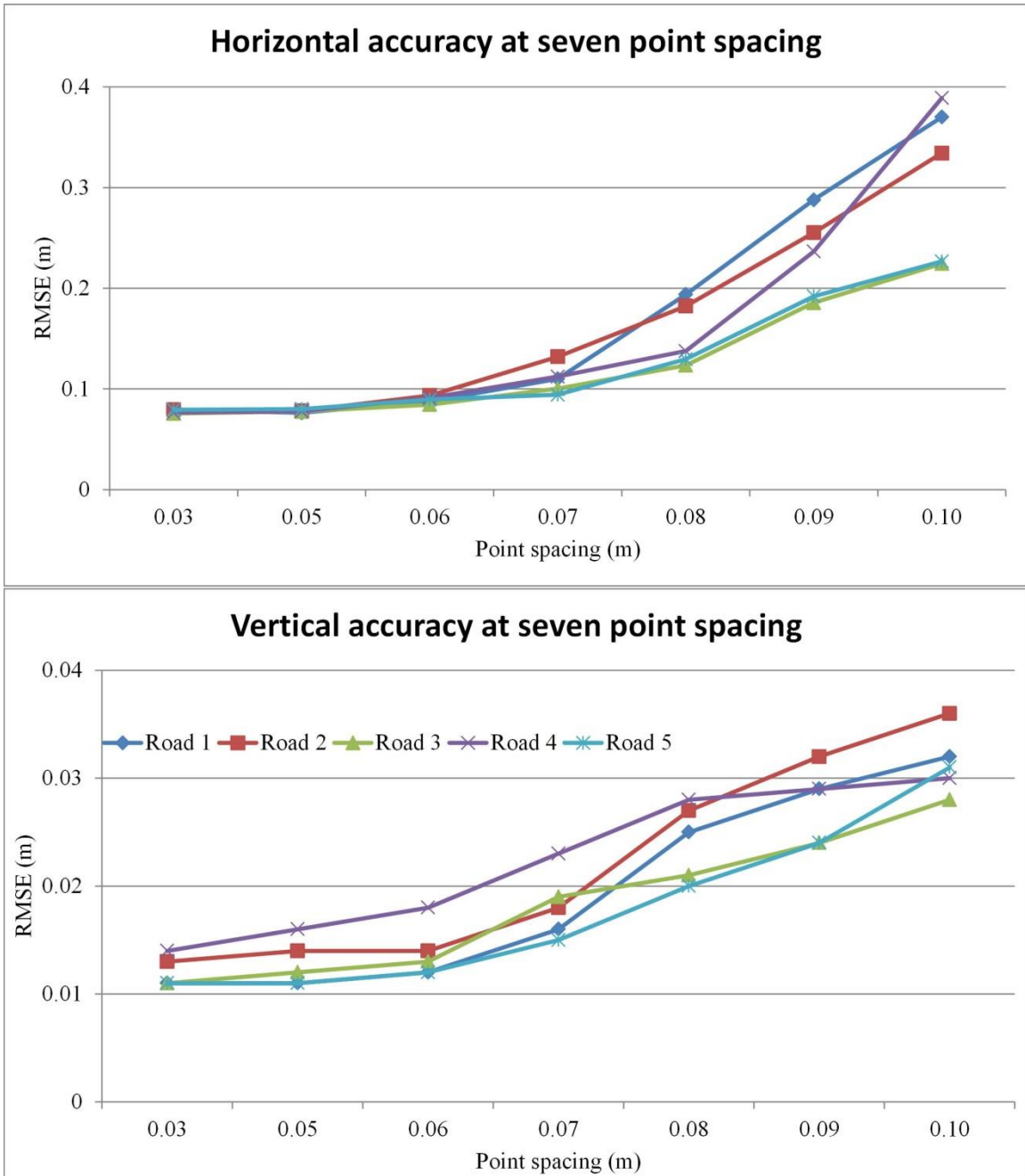
Figure 4.12: Accuracies of extracted roads at seven point spacing.

4.3.4 Computational Complexity

To further evaluate the performance of the proposed curb-based road extraction algorithm, computational efficiency is tested with the five datasets through the use of PC with a 3.30 Ghz Intel(R) Core(TM) i3-2120 CPU. According to the discussed sensitivity of parameters, the algorithm keeps $S_g = 25$ cm, $R_g = 3.0$ m, and $S_p = 5$ cm. The proposed road-surface algorithm comprises four steps: trajectory-based profiling, pseudo scan-line generation, curb detection, and road edge fitting. Thus, the average running time for the five datasets is about 30-40 seconds. The processing time of the proposed algorithm is highly dependent on the reading-and-writing speed of the hard disk due to frequent data-interaction operations. Although extracting operations for roads are mostly performed on 3D data, the processing is computationally efficient because of no data indexing structures being involved for data querying and searching. Thus, the proposed algorithm is a feasible means for transportation agencies to detect road in real time and provides a strong support to inspect road features efficiently.

4.3.5 Overall Performance

The developed algorithm is tested on two datasets: Huandao and ICEC, as shown in Figures 4.13 (a) and 4.14 (a). Due to no sharp turnings and curves on the roads, $R_g = 3.0$ m is used in this study. As a result, ICEC and Huandao datasets comprise 35 and 21 blocks, respectively. Each profile is sliced from each data block. Correspondingly, with a profile width S_g of 25 cm, there are 35 profiles for the ICEC dataset, and 21 profiles for Huandao dataset, respectively. Through experimentation, a profile is segmented into a number of grids, with each grid containing about 40 points and having a grid width Sp of 5 cm. Finally the profile is converted into a pseudo scan line using the principal points

estimated from the grid cells by the layering approach. Furthermore, the prior knowledge of curbs allows us to keep the curb height range between 8 cm and 30 cm. With those pre-defined thresholds, the curbs are extracted from the profiles and fitted into two smooth edges of the roads using the cubic B-Spline interpolation. A visual inspection demonstrates the good extraction results of the roads, as shown in Figures 4.13 (b) and 4.14 (b). 20 and 15 reference points are used for validating Huandao and IECE datasets, respectively. The following table shows that the positional accuracies of the extracted road surfaces are 8 cm and 2 cm in horizontal and vertical, respectively.

Table 4.2: Horizontal and vertical accuracies for two test datasets.

| Point No.	HuanDao Dataset (cm)		ICEC Dataset (cm)	
	Horizontal	Vertical	Horizontal	Vertical
1	8.2	1.2	5.4	1.5
2	13.7	2.5	5.7	2.8
3	8.8	1.6	6.4	1.6
4	7.3	1.1	10.4	1.3
5	9.1	1.6	8.5	1.9
6	8.6	2.8	10.3	2.4
7	5.1	2.5	4.9	2.1
8	5.5	2.3	5.7	1.3
9	7	1.8	5.3	1.8
10	1.1	1.3	5.9	3.5
11	12.1	2.4	11.1	2.2
12	7.8	2.3	9.0	2.7
13	7.2	1.9	6.8	1.1
14	9.5	2.1	6.7	1.7
15	9.1	2.5	7.5	2.3
16	10.1	1.7		
17	4.3	2.4		
18	13.4	2.3		
19	6.4	2.2		
20	6.7	2.4		
RMSE	8.6	2.1	7.6	2.1

(a)
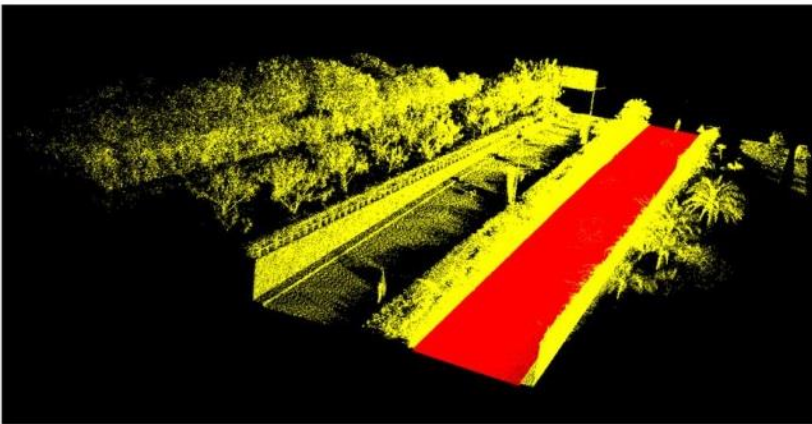
(b)

Figure 4.13: Huandao dataset and extracted results.
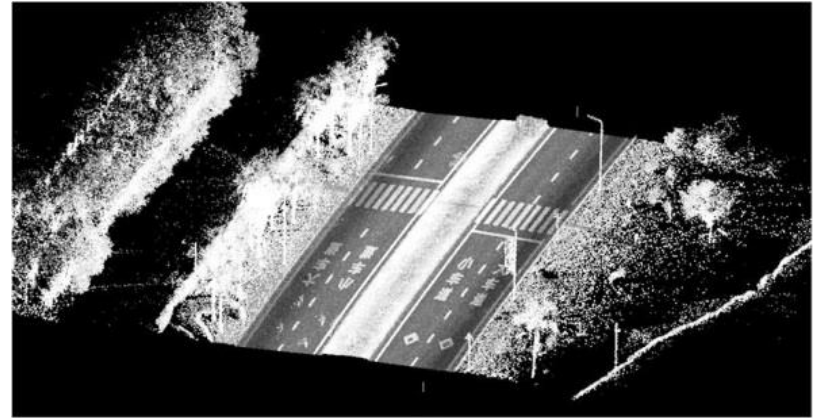
(a)
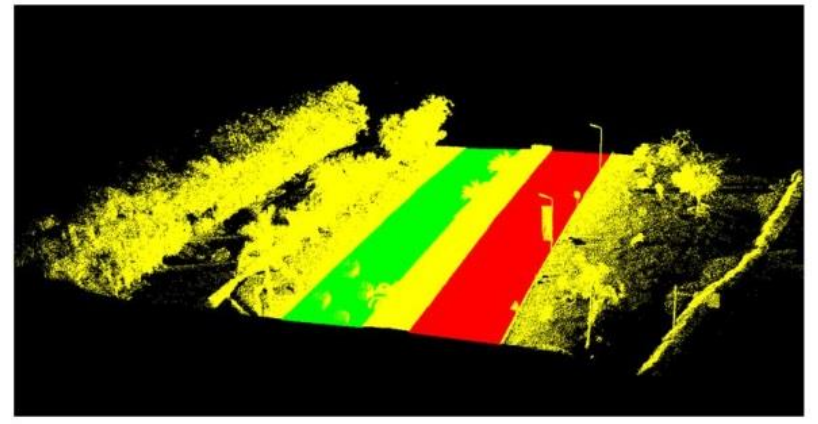
(b)

Figure 4.14: ICEC dataset and extracted results.

4.4 Discussion

The curb-based road-surface extraction method is presented with an assistance of the vehicle trajectory. The proposed algorithm was based the assumption that curb is a road boundary that separates a road from a sidewalk or a green space with a certain height. Thus, it is straightforward to detect curbs for separating road points from off-road points. Three challenges were considered for developing the algorithm.

The first challenge is how to deal with a large volume of MLS data collected by a newest RIEGL VMX-450 system. Normally, most established approaches to laser scanning data processing were developed for ALS data, whose point density is about 10-20 points per square meter. The current ALS data are at Megabyte level, while MLS data are at Gigabyte or even Terabyte level. Thus, the proposed algorithm partitioned the whole MLS data into a number of data blocks, on each of which curbs were detected without any data indexing structures involved, indicating that the developed algorithm is computationally efficient.

The second challenge is how to detect curbs from the profiles sliced from each data block. On each profile image, the curbs are clearly presented. All points within a profile were projected onto a plane perpendicular to the line of travel. However, the profile image just contains a number of irregular points. To detect curbs, those points were re-organized to a scan-line alike pattern, called pseudo scan-line, by sampling them with a given point spacing. Based on the re-organized pseudo scan-line, two criteria such as slope and elevation difference were used to detect curbs.

The third challenge is to detect curbs from pseudo scan-lines. Not only curbs but also other objects over the roads would show height jumps. To eliminate non-curb points,

two mathematical definitions were defined: (1) slope and (2) elevation difference. Specifically, the slope between two consecutive points in a pseudo scan-line and the elevation difference of a laser point relative to its neighbors in the pseudo scan-line are defined to search curbs. Basically, the curbs were completely detected from each profile with these two criteria.

The developed algorithm for road extraction was analyzed for automated selection of the input parameters. There are three parameters - the length of a block R_g, the width of a profile S_g, and the point spacing S_p-having a great impact on the performance of the proposed curb-based road-surface algorithm. The experimental results demonstrated that choosing a too large block length will decrease the horizontal and vertical accuracies. The 3.0 m block length was recommended as the most applicable value which normally produces the best performance. The experimental results also showed that choosing a too small profile width will reduce the horizontal and vertical accuracies, while choosing a too large profile width will also decrease the accuracies. The optimal value for the profile width is between 20 and 30 cm which will achieve better accuracies. The experimental results also demonstrated that choosing too large point spacing will produce a decreasing accuracies in horizontal and vertical. The optimal value is 4 or 5 cm for generating pseudo scan-lines and detecting curbs. The selected parameters were tested on two datasets: Huandao including 8.4 million points in a road length of 105 m and ICEC containing 5.4 million points covering the road length of 63 m. The average horizontal accuracies for these two datasets are 8.1 cm and 7.3 cm, the average vertical accuracies are 2.1 cm and 2 cm, respectively.

The proposed approach has a few distinctions. First, it is computationally efficient as the calculation is performed within pseudo scan-lines generated from large volumes of MLS data via a profiling strategy. Curbs are detected from a number of pseudo scan-lines instead of the whole MLS data. By taking advantage of the pseudo scan-lines, the proposed algorithm does not require a special data structure, such as triangular irregular network (TIN) and quad-tree, to facilitate the road-surface extraction process. It needs no searching or calculation within the whole MLS data.

Moreover, for the slope calculation in Eq. (4.2), only two consecutive points are needed. The local elevation and slope are updated every time a curb candidate is encountered along the profile. Because points in the pseudo scan-line are at regular interval and stored as a sequence of sampling points, the required calculations are reduced to the minimum by comparing two consecutive points along a profile. Therefore, profiling MLS data along the trajectory and detecting curbs on pseudo scan-lines substantially increase the efficiency in handling large-volume MLS data for practical applications.

Third, a combination of slope and elevation criteria can consider the complex surroundings of roads. As addressed earlier, the slope criterion essentially detects the abrupt road edge candidates while the elevation criterion identifies the curbs from objects on the roads. The selection of the local ground elevation threshold usually ranges from 10 to 30 cm according to conventional road design manuals. Each time a curb is encountered when its elevation is within the elevation range. In this way, the approach is adaptive to the complexity of road surroundings.

4.5 Chapter Summary

This chapter presented a curb-based road extraction algorithm, which was based on the vehicle trajectory, for detecting roads from MLS data. To detect roads, a stepwise procedure is proposed: (1) MLS data profiling, (2) generation of pseudo scan-lines, (3) curb detection from each pseudo scan-line based on the elevation difference and slope criteria, and (4) road edge Spline interpolation.

The automated selection of the optimal values for input parameters were discussed. The algorithm performance was evaluated on Huandao and ICEC datasets. The average horizontal and vertical accuracies for the two datasets are 8.1 cm and 2 cm, respectively. The low positioning accuracy in horizontal is partially determined by the original density of sampling points of MLS data. The denser the MLS data are, the higher the horizontal accuracies of the extracted roads. Overall, the accuracies of the detected roads meet the requirements of transportation-related road applications, such as natural terrain mapping, roadway condition assessment, GIS road inventory, and urban traffic modelling.

Chapter 5 Road-marking Extraction[2]

This chapter details the algorithm for the automated extraction of road markings from MLS data. The proposed road-surface extraction algorithm has been described in Chapter 4 for extracting road points from MLS data. After that, the classified road points are interpolated into a GRF image. Next, to reduce noise and improve road-marking completeness, a point-density-dependent, multi-threshold segmentation method is applied to the GRF image for identifying road markings using a morphological operation. Validation is described in Section 5.2. The conducted tests are described and analyzed in Section 5.3. Discussions are presented in Section 5.4. Section 5.5 provides a summary of this chapter.

5.1 Algorithm Description

This chapter presents a recognition framework for road markings used in a mobile mapping system, and analyzes its performance on a variety of road-marking types selected from RIEGL VMX-450 data. The road-marking extraction method can be seen as a stepwise procedure of interpreting MLS data, as shown in Figure 5.1. The method mainly includes the following four steps:

---

[2] The main work presented in this chapter has been published by, Guan, H., Li, J.,Yu, Y., Wang, C., Chapman, M., and Yang, B. 2014. Using mobile laser scanning data for automated extraction of road markings. *ISPRS Journal of Photogrammetry & Remote Sensing*, 87 (2014): 93-107.
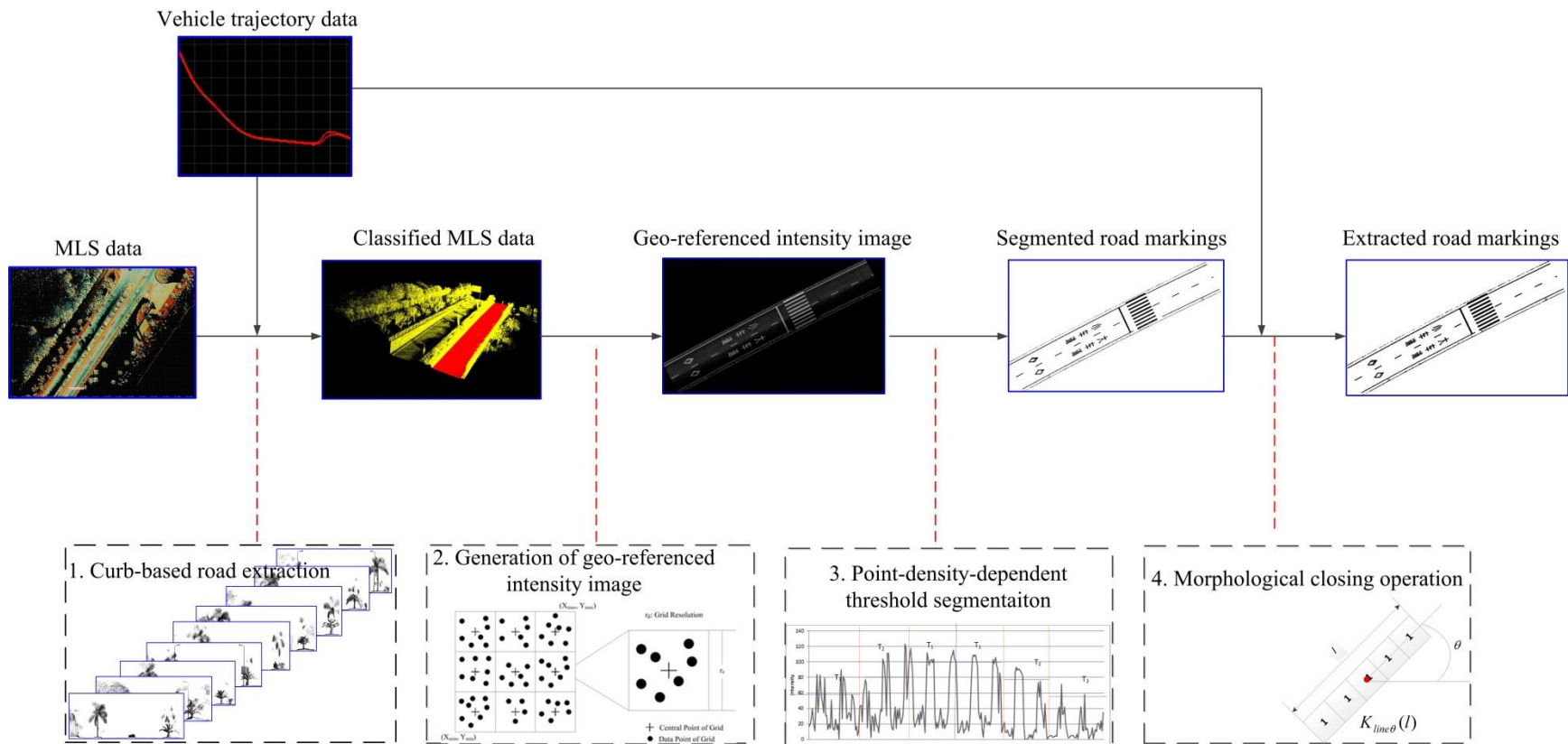
Figure 5.1: An overview of the proposed road-marking extraction algorithm.

.

(1) Curb-based road-surface extraction: the raw MLS data are partitioned, based on the vehicle trajectory, into blocks and their corresponding profiles, by which pseudo scan-lines are formed to detect small height jumps caused by road curbs.

(2) GRF image generation: the segmented road points are interpolated into a GRF image via an extended inverse distance weighted (IDW) method that combines local-global elevation and intensity data.

(3) Point-density-dependent thresholding: the GRF image is dynamically segmented to recognize road markings by the point-density-dependent multi-thresholds.

(4) Morphological operations: To remove noise and fill in holes for the extracted road markings, morphological operations are used to achieve final results.

5.1.1 Extraction of Road Surfaces

According to the vehicle trajectory, the raw MLS data are partitioned into a number of blocks and profiles, on each of which a pseudo scan-line is generated and curbs are detected based on elevation-difference and slope criteria. The principle behind this is that curb, as a nearly vertical surface, is a boundary of road surface and sidewalk with a certain height. Finally, a cubic spline interpolation fits the extracted curb points into smooth road edges with the constraint of the vehicle trajectory. The algorithm for automated road extraction was detailed in Chapter 4. Figure 5.2 shows two results of road extraction. A close-up view demonstrates that the road surfaces are well extracted along the bottoms of the curbs.
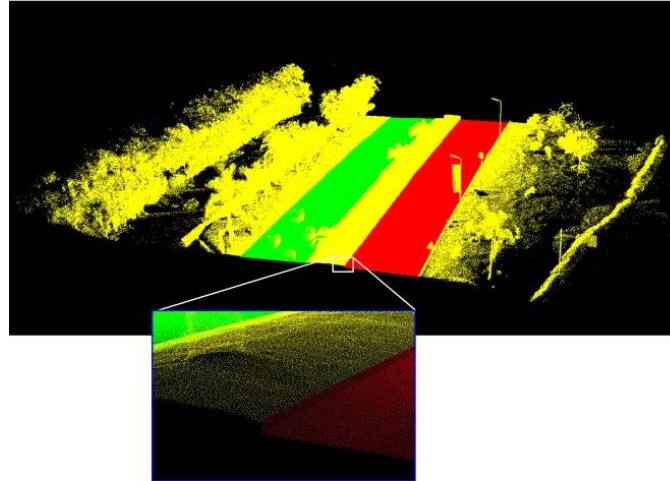
(a)
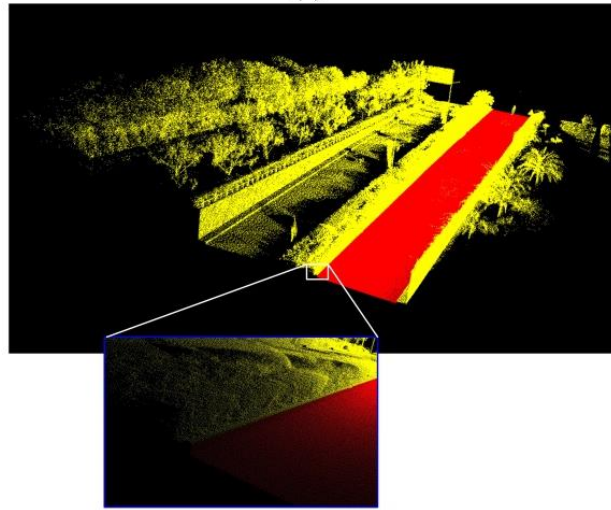
(b)

Figure 5.2: Two samples of the road extraction results, (a) Huandao dataset, and (b) ICEC dataset.
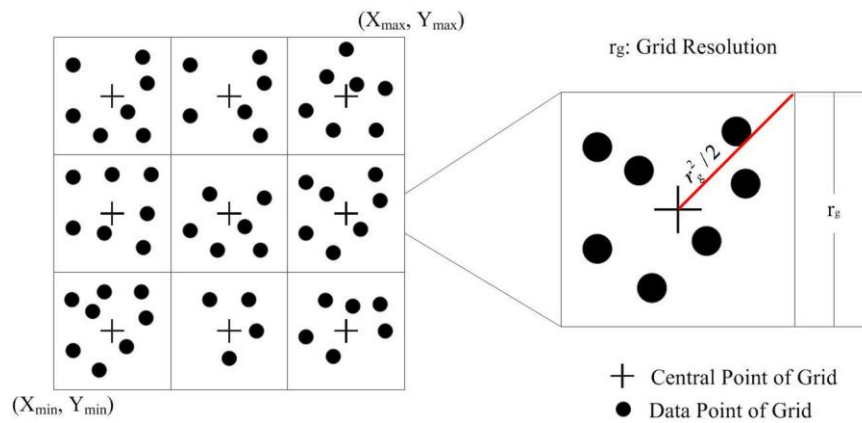
Figure 5.3: An illustration of the determination of gray values.

5.1.2 Generation of GRF Images

After extracting road points from MLS data, the extracted road points are rasterized into a GRF image, in which the gray value of a pixel is interpolated from its nearest neighbours using IDW interpolation. Although the interpolation might cause a loss of accuracy, it is computationally efficient for processing a substantially large volume of MLS data using established image processing algorithms. The IDW interpolation stated in Yang et al. (2012) is extended to generate a GRF image. The image resolution (r_g) can be referred to by point density, as shown in Figure 5.3.

In Yang et al. (2012), there are the following two rules for generating a geo-referenced intensity image:

Rule 1: a point with higher reflectivity has a greater weight;

Rule 2: a point farther away from the central point has a smaller weight.

According to the two rules, the gray value of a grid cell is calculated by:

$$
\begin{cases}
G_{ij}^{I} = \left(\sum_{k=1}^{n_{ij}} W_k^{ij} I_k^{ij} \right) \Big/ \left(\sum_{k=1}^{n_{ij}} W_k^{ij} \right) \\
W_k^{ij} = \alpha W_{k,ij}^{D} + \beta W_{k,ij}^{I} \\
\alpha + \beta = 1.0
\end{cases}
, \tag{5.1}
$$

where, W_k^{ij} is the weight of the *k-th* point within the grid cell (*i, j*), I_k^{ij} is the reflectivity of the *k-th* point, and n_{ij} is the total number of data points within the grid cell (*i, j*). α and β are the weight coefficients, $W_{k,ij}^{I}$ and $W_{k,ij}^{D}$ are the weights representing Rules 1 and 2, respectively. The two weights are calculated by the following Eqs. (5.3) and (5.4):

$$
W_{k,ij}^{D} = \frac{1}{r_g^2} \left(\frac{2+r_g^2}{1+D_{k,ij}^2} - 2 \right) \tag{5.2}
$$

where, $D^2_{k,ij} = (x_{p_k,ij} - x_{p_o,ij})^2 + (y_{p_k,ij} - y_{p_o,ij})^2$, $(x_{p_k,ij}, y_{p_k,ij})$ are the coordinates of the

k-th point within the grid cell (i,j), $(x_{p_o,ij}, y_{p_o,ij})$ are the coordinates of the central point

within the grid cell (i,j), $D_{k,ij}$ is the distance between points $(x_{p_k,ij}, y_{p_k,ij})$ and $(x_{p_o,ij}, y_{p_o,ij})$.

Eq. (5.2) defines the range of the weight $W^D_{k,ij}$ within $[0,1]$. The weight $W^D_{k,ij} = 1$ when

$D_{k,ij} = 0$, that is, point $(x_{p_k,ij}, y_{p_k,ij})$ is at the central point $(x_{p_o,ij}, y_{p_o,ij})$ of the grid cell,

indicating point $(x_{p_k,ij}, y_{p_k,ij})$ has the greatest contribution to the weight $W^D_{k,ij}$. On the

contrary, The weight $W^D_{k,ij} = 0$ when $D_{k,ij} = r_g / \sqrt{2}$ (a half of the diagonal of the grid

cell), that is, point $(x_{p_k,ij}, y_{p_k,ij})$ is far most from point $(x_{p_o,ij}, y_{p_o,ij})$, indicating point $(x_{p_k,ij},$

$y_{p_k,ij})$ has barely contribution to the weight $W^D_{k,ij}$.

$$W^I_{k,ij} = W^{I1}_{k,ij} \cdot W^{I2}_{k,ij} \qquad (5.3)$$

$$
\begin{cases}
W^{I1}_{k,ij} = \dfrac{1}{(g^{ij}_{max} - g^{ij}_{min})^2} \left(\dfrac{1+(g^{ij}_{max} - g^{ij}_{min})^2}{1+(L^L_{k,ij})^2} - 1 \right) \\[2ex]
W^{I2}_{k,ij} = \dfrac{1}{(I_{max} - I_{min})^2} \left(\dfrac{1+(I_{max} - I_{min})^2}{1+(L^G_{k,ij})^2} - 1 \right) \\[2ex]
I^L_{k,ij} = I_{p_k,ij} - g^{ij}_{min} \\[1ex]
I^G_{k,ij} = I_{p_k,ij} - I_{min}
\end{cases} ,
$$

where, I^{ij}_k is the intensity value of the k-th point, $W^{I1}_{k,ij}$ and $W^{I2}_{k,ij}$ are the weights for

the local and global information, g^{ij}_{max} and g^{ij}_{min} are local maximal and minimal intensities

within the grid (i,j), I_{max} and I_{min} are the global maximal and minimal intensities of the

entire road points, and $I^L_{k,ij}$ and $I^G_{k,ij}$ are the local and global intensity differences,

respectively. Unlike the distance weight $W^D_{k,ij}$, the intensity weight $W^I_{k,ij}$ is divided into the

following two parts: a local weight $W_{k,ij}^{I1}$ and a global weight $W_{k,ij}^{I2}$ in order to equalize the calculated pixel values of the GRF image. Similar to histogram equalization - a method in image processing for contrast adjustment using the image's histogram - the local weight $W_{k,ij}^{I1}$ is combined with the global weight $W_{k,ij}^{I2}$ to increase the global contrast of the GRF image. Through this adjustment, the intensities can be consistently distributed on the histogram, as shown in Figure 5.4.
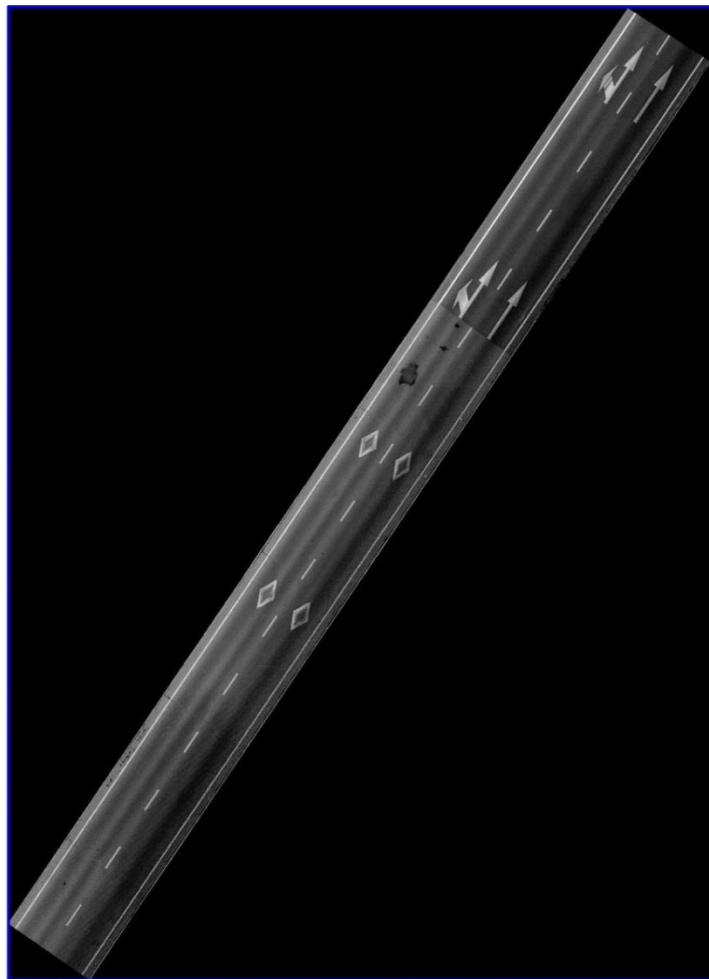
(a)

(b)

Figure 5.4: GRF images generated from MLS data: (a) Huandao dataset, and (b) ICEC dataset.

5.1.3 Determination of Multi-thresholds

In the generated GRF image, a threshold-based segmentation algorithm is normally carried out to obtain the road markings. However, although the proposed equalization strategy lessens the intensity imbalance caused by point-density differences, the intensity values of road markings are not consistent but gradually fade from the scanning center to its two sides, as shown in Figure 5.5(a). This variation is because of the reflected intensity values that depend on (1) the scanning range from the laser sensor to the target, (2) the incidence angle of the laser beam, and (3) the material properties of the target. Spontaneously, a dynamic multi-threshold segmentation algorithm is proposed based on the scanning distance change. Within different ranges of scanning distances, local optimal segmentation thresholds are adaptively estimated.

Due to the variation of the vehicle trajectory, MLS data are still processed block by block. As mentioned in Chapter 4, each block $Block_i$ has a corresponding profile $profile_i$. The point density for each $profile_i$ is statistically analyzed, as green bars shown in Figure 5.5 (b). Note that the point density approximates normality. Thus, a Gaussian

97

normal distribution (red line) can be fitted to obtain two estimated parameters: mean μ and standard deviation σ. Inspired by the "68-95-99.7" rule of a normal distribution that says about 68% of values within one standard deviation σ away from the mean, about 95% of the values within two standard deviations, and about 99.7% within three standard deviations, intensity variations of the generated GRF image follows this rule. Thus, according to the three-sigma rule, the corresponding range can be determined to vertically section data into a number of bins, on each of which an optimal threshold is calculated for segmentation.
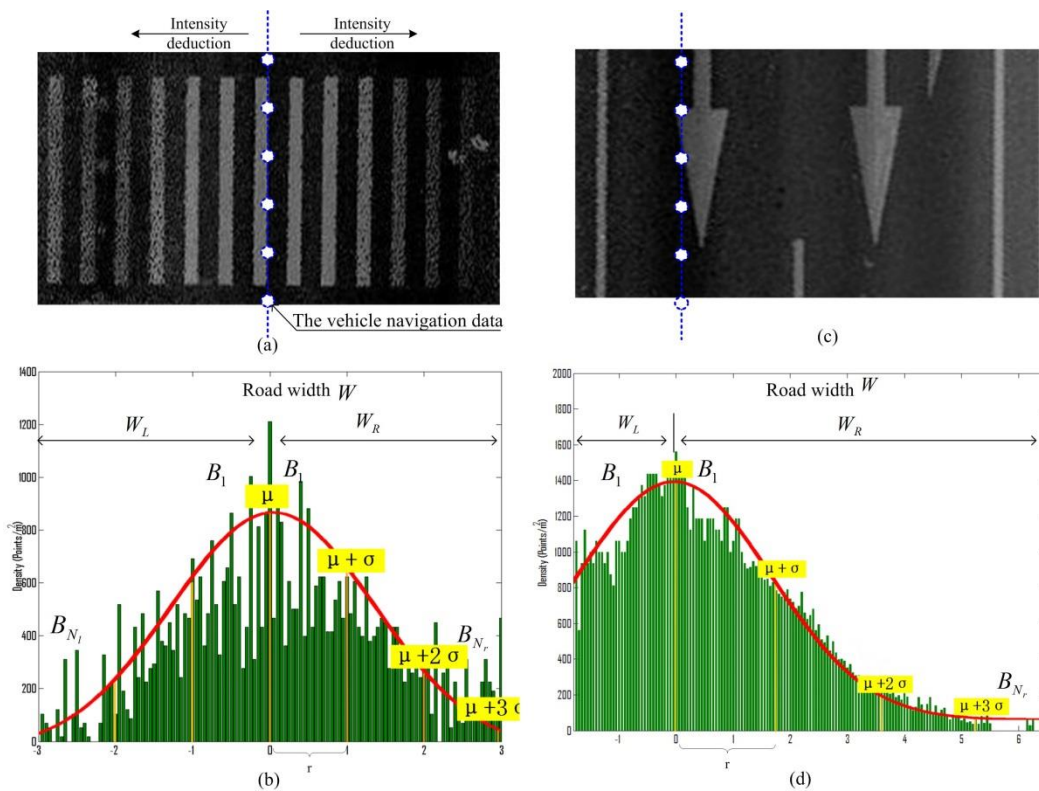
Figure 5.5: Point-density-dependent multi-threshold segmentation: (a) Sample data I (b) statistical analysis of sample data I, (c) Sample data II, and (d) statistical analysis of Sample data II.

First, according to the vehicle trajectory and the estimated road width (W) from the extracted road data, the width of the right side (W_R) and the width of the left side (W_L) of the vehicle trajectory are calculated. Then, the range (r) for one sigma of the fitted Gaussian normal distribution function is calculated by the estimated mean μ and standard deviation σ. Finally, the number of the bins is calculated as:

$$N_r = INT(W_R / r) + 1$$
$$N_l = INT(W_L / r) + 1$$

(5.4)

As a result, the number of ($N_r + N_l$) bins is obtained for each B_i. The number of bins varies with the vehicle trajectory. For example, the data block would have six bins if the vehicle was driving close to the center line of the road (see Figures 5.5(a) and (b)), while the data block would have 5 bins if the vehicle was driving along the left lane of the road (see Figures 5.5(c) and (d)). With vehicle trajectory, the fitted normal distribution of the point density determines how many bins can be sliced.

5.1.4 Multi-threshold-based Segmentation

In each bin $B_i (i = 1,2,...,(N_r + N_l))$, potential road markings are segmented by Otsu's method, proposed by Otsu (1979), which is widely implemented as the default approach to image thresholding. The principle of Otsu's method was detailed in Chapter 3. Otsu's method assumes that an image to be divided contains two classes: C1 and C2, that is, foreground (e.g., road markings) and background, and then calculates their cumulative probabilities and mean levels, respectively. As a result, Otsu's method can select an optimal threshold (t) that maximizes the between-class variance based on the discriminant analysis. Figure 5.6 shows the results of multi-threshold segmentation.
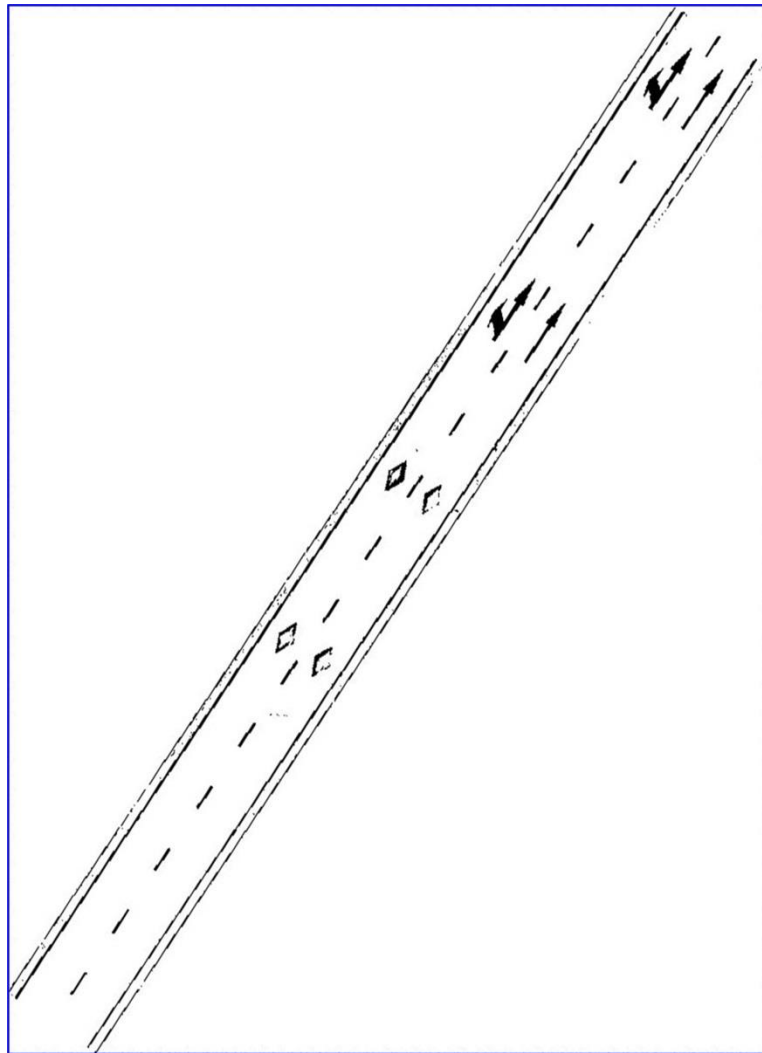
(a)
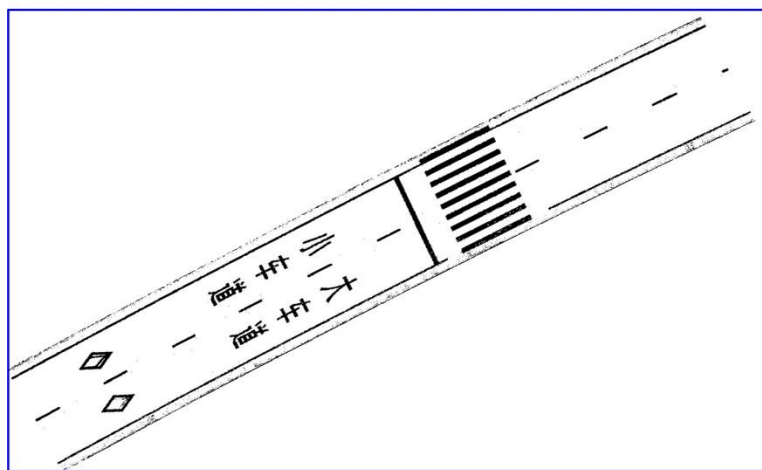
(b)

Figure 5.6: Road-marking segmentation results for (a) Huandao dataset, and (b) ICEC
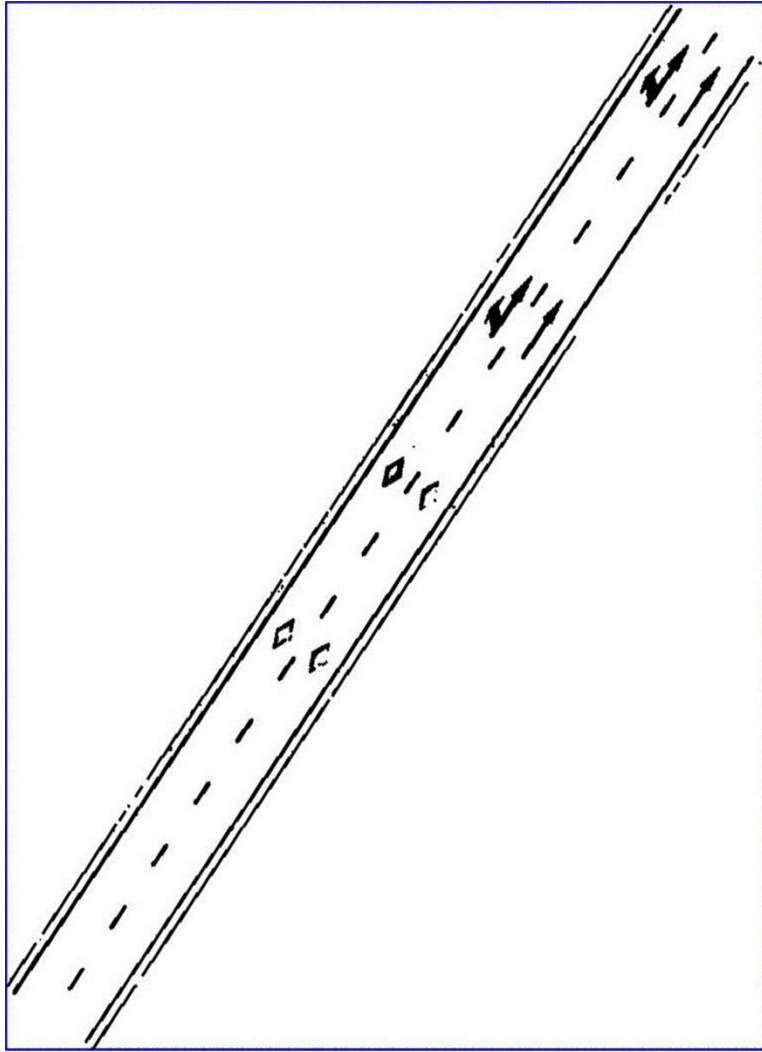
dataset.

(a)
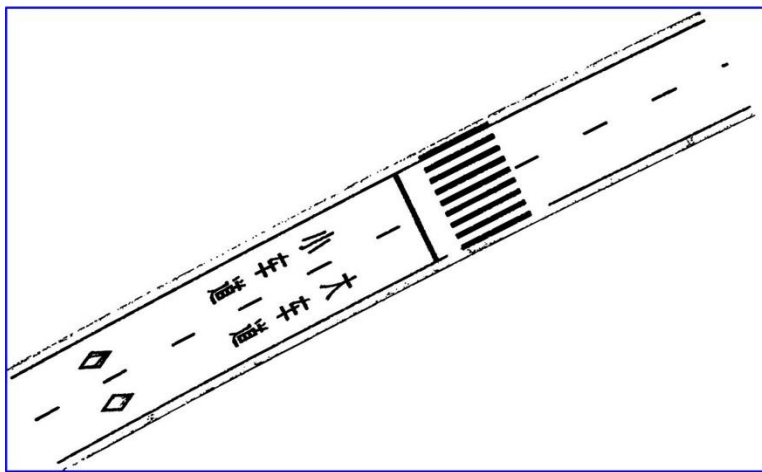
(b)

Figure 5.7: Road-marking extraction results for (a) Huandao dataset, and (b) ICEC

dataset.

5.1.5 Morphological Operation

In spite of the use of the proposed segmentation algorithm, the extracted road markings still contain noise and are incomplete. By knowing the form and the structure of the road markings, a morphological operation is used to remove noises and extract complete road markings. The morphological operations rely only on the relative ordering of pixel values, rather than on their numerical values, and therefore are especially suited to process binary images. The morphological operation to be use is closing, that is, dilation and erosion. A dilation operation is first employed to remove noises and fill out holes in the extracted road markings. Subsequently, an erosion operation is used to shrink the image from both the inner and outer boundaries of the road markings.

The morphological techniques probe the road markings with a small shape or template called a structuring element; the structuring element is a small binary image, that is, a small matrix of pixels. The structuring element is related to the *size (T)*, *origin*, and *shape*. The structuring element examples include square, cross, diamond, horizontal and vertical shaped. A common practice is to have odd dimensions of the structuring matrix and the *origin* defined as the centre of the matrix. Although there are many types of road markings such as crosswalks, characters, words, symbols, and arrows, most of them are linearly shaped. To simplify convolution, a horizontally linear shaped structuring element is used to dilate and erode the road markings. The linear structure with length l and direction θ is denoted by $K_{line\theta}(l)$. The direction θ is determined by the vehicle trajectory, that is, the direction in which the vehicle is moving. A range of the length l from 3 to 11 is researched to determine $K_{line\theta}(l)$ for the road markings. This

thesis picks up $l = 3$ pixels for extracting road markings. Figure 5.7 shows the results of road-marking extraction for Huandao and ICEC datasets by the morphological operations.

5.2 Validation

By comparing the extracted road markings with the manually interpreted ground-truth, the results of the road markings were quantitatively evaluated with the following three measures: completeness (*cpt*), correctness (*crt*), and F-measure. *cpt* describes how complete the extracted road markings are, while *crt* means to what percentage the extracted road markings are valid. The *cpt* is expressed as $cpt = C_p/Rf$ and *crt* is defined as $cpt = C_p/E_p$, where C_p denotes the number of pixels belonging to the actual road markings, Rf is the ground-truth collected by the manual interpretation method, and E_p represents the number of pixels extracted by the proposed algorithm. *F-measure* is an overall score, defined as $F = 2 \times \dfrac{(cpt \cdot crt)}{(cpt + crt)}$.

5.3 Experiments

From the generation of the GRF image to the extraction of the road markings, there are several parameters involved, such as (1) the weight coefficients (α and β), (2) the image resolution (r_g), (3) the number of bins to be sliced (N_s), (4) segmentation thresholds (T_i, i=1,2, 3, …, N_s), (5) the kernel size (l), and (6) the direction (θ). These parameters are detailed in Table 5.1. Among these parameters, the number of bins is determined by the point density, and the segmentation thresholds (T_i) are automatically calculated by Otsu's method; the direction (θ) of the linear structuring element depends on the trajectory.

Table 5.1: Parameters used in the road-marking extraction method.

Stage	Name	Definition	Value
The generation of the GRF image	α	Distance weight	0.5
	β	Intensity weight	0.5
	r_g	Image resolution	To be decided
The extraction of the road markings	N_s	Number of bins	Automatically determined by the point density
	T_i	Segmentation thresholds	Automatically determined by Otsu's method
	l	Structuring element size	To be decided
	θ	Structuring element direction	Automatically determined by the trajectory

5.3.1 Generation of GRF Images

The weight coefficients α and β are used to control the contributions of both the distance and intensity to the gray value of a grid cell during implementation of the extended IDW interpolation. The following different groups were tested on weight coefficients α and β : (0.0,1.0), (0.2, 0.8), (0.4,0.6), (0.6,0.4), (0.8,0.2), and (1.0, 0.0). Accordingly, Figure 5.8 shows the generated six GRF images, ranging from A1 to A6. For example, the comparative results of B1 (Image A1 minus Image A2) and C1 (Image A5 minus Image A6) show that both the intensity and distance information contribute to the gray values of the GRF image. In Figure 5.8, Images A2 to A5 (see row 1) and Images B1 to B4 (see row 2) demonstrate that the quality of the GRF images is relatively stable when the weight coefficient α changes from 0.2 to 0.8, and the weight coefficient β from 0.8 to 0.2, accordingly. To investigate the changes among the GRF images, the pixel-level difference ($P_{pld} = \sum G_i / N_{change}$) is used to describe the difference between

two images (Yang et al., 2010), where $\sum G_i$ denotes the sum of gray values of the changed pixels, and N_{change} is the number of the changed pixels. The pixel-level-difference tables in Figures 5.8 (a) and (b) confirm that there is no improvement or change among the four images (A2, A3, A4, A5) with weight coefficients α and β as (0.2, 0.8), (0.4,0.6), (0.6,0.4), (0.8,0.2). As a result, in the following experiments, the weight coefficients α and β of (0.5, 0.5) is applied to the road points for generating GRF images.

In Eq. (5.3), the intensity weight $W_{k,ij}^{I}$ includes the following two parts: $W_{k,ij}^{I1}$ and $W_{k,ij}^{I2}$ for the local and global information, respectively. The global weight $W_{k,ij}^{I2}$ functions as an equalizer that stretches the gray values of the GRF image for contrast adjustment, thus allowing for areas of lower contrasts to gain higher contrasts. Figure 5.9 shows a comparison of images with and without the global weights (images *A2* and *a2*). Image *A2-a2* is the result of image *A2* minus image *a2,* indicating that the use of the global weight contributes to contrast enhancement. The vertical profiles *B* and *B'* also confirm that the contrasts between the background and foreground in image *A2* are greater than those in image *a2*. Through this global adjustment, the intensities can be better distributed for road-marking extraction.

image No	A1	A2	A3	A4	A5	A6
A1		4.19	4.19	4.19	4.19	4.71
A2	4.19		0.00	0.00	0.00	1.14
A3	4.19	0.00		0.00	0.00	1.14
A4	4.19	0.00	0.00		0.00	1.14
A5	4.19	0.00	0.00	0.00		1.14
A6	4.71	1.14	1.14	1.14	1.14	

(a)

| | α=0.0 ß = 1.0 | α=0.2 ß = 0.8 | α=0.4 ß =0.6 | α=0.6 ß =0.4 | α=0.8 ß =0.2 | α=1.0 ß =0.0 |

image No.	A1	A2	A3	A4	A5	A6
A1		1.86	1.86	1.87	1.87	3.86
A2	1.86		0.03	0.05	0.05	3.40
A3	1.86	0.03		0.01	0.02	3.40
A4	1.87	0.05	0.01		0.01	3.40
A5	1.87	0.05	0.02	0.01		3.40
A6	3.86	3.40	3.40	3.40	3.40	
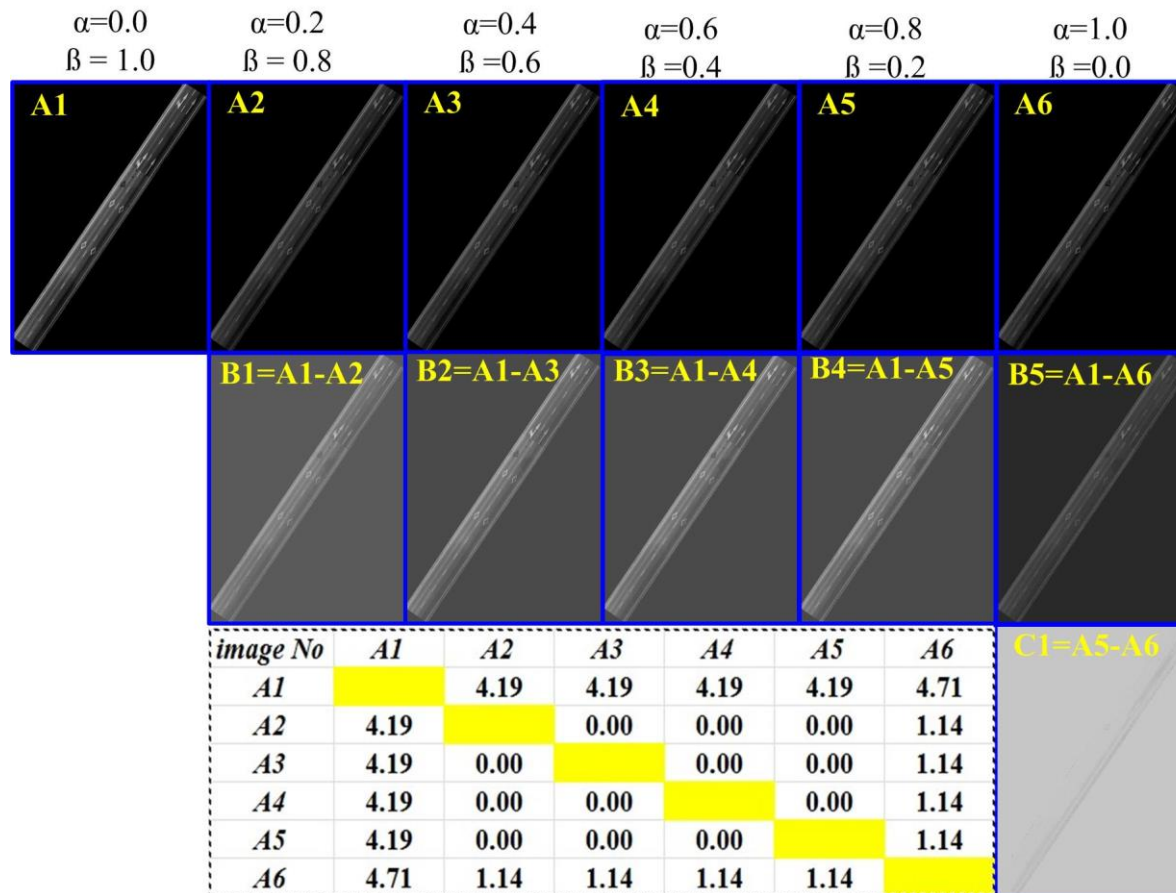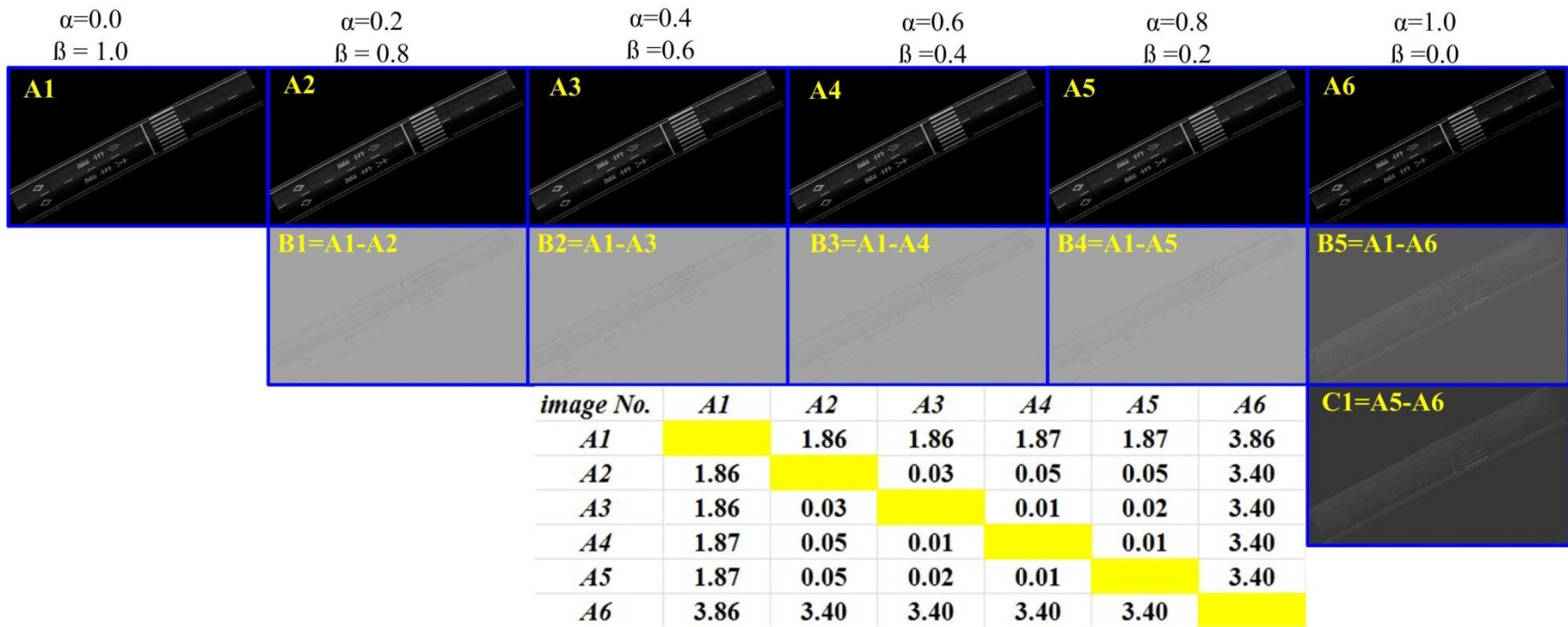
(b)

Figure 5.8: Sensitivity analysis of two coefficient parameters α and β with the grid size of 4 cm: (a) Huandao dataset, and (b) ICEC dataset.
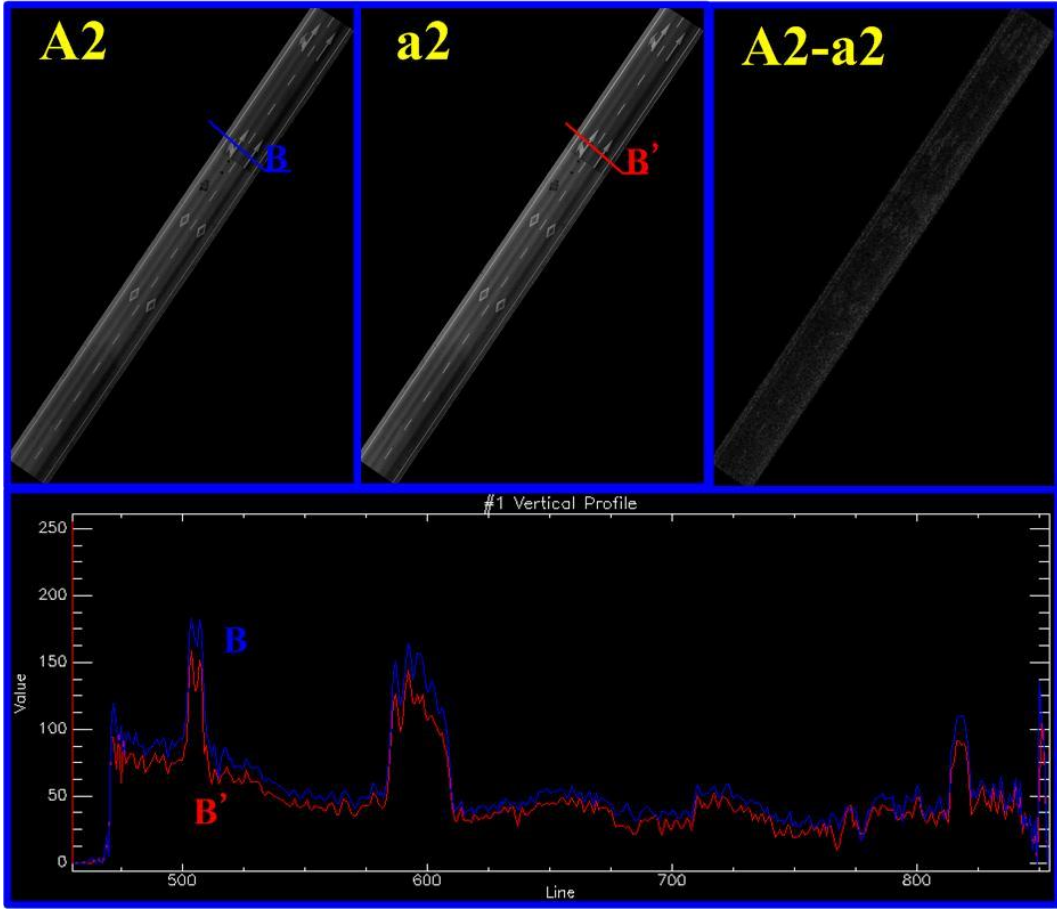
(a)
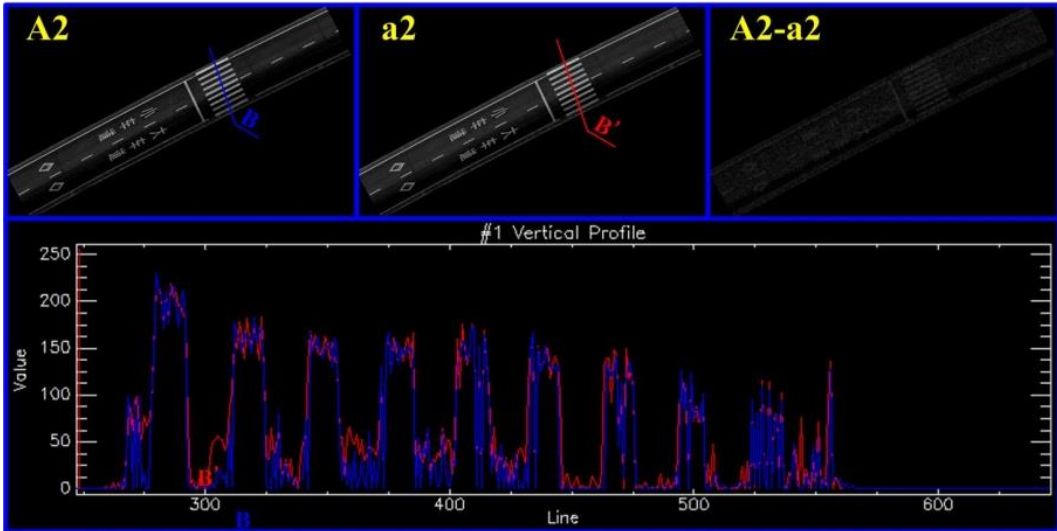
(b)

Figure 5.9: A comparison of intensity normalization between using global-and-local and global information alone: (a) Huandao dataset, and (b) ICEC dataset.

5.3.2 Road-marking Extraction

The performance of the proposed segmentation algorithm is tested by comparing it with the fixed threshold using eight road-marking images from two datasets. Table 5.2 summarizes the types of road markings; each road-marking image includes two or three types of road markings. To the best of our knowledge, currently there is no dataset that is designed for evaluating the performance of road-marking extraction from MLS systems.

Table 5.2: Types of road markings in eight GRF images.

Image Name	Types of road markings
Marking 1	arrow markings, solid edgeline and broken laneline markings
Marking 2	symbol markings, solid edgeline and broken laneline markings
Marking 3	word markings, solid edgeline and broken laneline markings
Marking 4	solid edgeline and broken laneline markings
Marking 5	crosswalk markings
Marking 6	arrow markings, symbol markings, solid edgeline and laneline markings
Marking 7	hatch markings
Marking 8	hatch markings and solid line markings

The proposed road-marking extraction algorithm keeps the weight coefficients at $\alpha = 0.5$, $\beta = 0.5$, and the image resolution at $r_g = 4$ cm for generating the GRF image. The eight road-marking examples are shown in Figure 5.10. The second row presents the segmentation results using the optimal single thresholds based on a histogram analysis, where noises emerge on one side of each of the roads, while a part of the road markings are missing on the other side. For example, the histogram of Marking 1 suggests that the gray value of 90 is the optimal threshold to separate the foreground (road markings) from

the background. The segmentation results, however, show that the straight-ahead arrow marking (at the bottom) is barely identified, although the turn-left-and-straight-ahead arrow marking (at the top) is almost completely detected with much noise. Therefore, it is difficult to keep a trade-off between correctness and completeness of road markings using a universal threshold.

However, compared to the results in the second row, all results in the third row indicate that all road markings, such as the word, hatch and arrow markings, can be correctly and completely identified. Note that the eight road-marking images generate their own three thresholds by Otsu's method, indicating that the proposed multi-threshold segmentation method can provide optimal local thresholds, regardless of the road materials and dimensions.

To explore the impact of structuring element size on road-marking extraction, a range of l (3,5,7,9,11) is searched for the eight road markings shown in Figure 5.10, while keeping $\alpha = 0.5$, $\beta = 0.5$, and $r_g = 4$ cm. Figure 5.11 displays the extracted road-markings on the eight examples with the five sizes of horizontal structuring elements. Visual inspection suggests that there was no significant change for most road markings when l was increased from 3 to 5. However, along the road edges, small areas of noise caused by the multi-threshold segmentation algorithm become larger after performing the morphological closing operation. In addition, the road markings are gradually dilated with increasing kernel size. Particularly, the word markings within Marking 3 are severely dilated since l increases from 5 to 11.
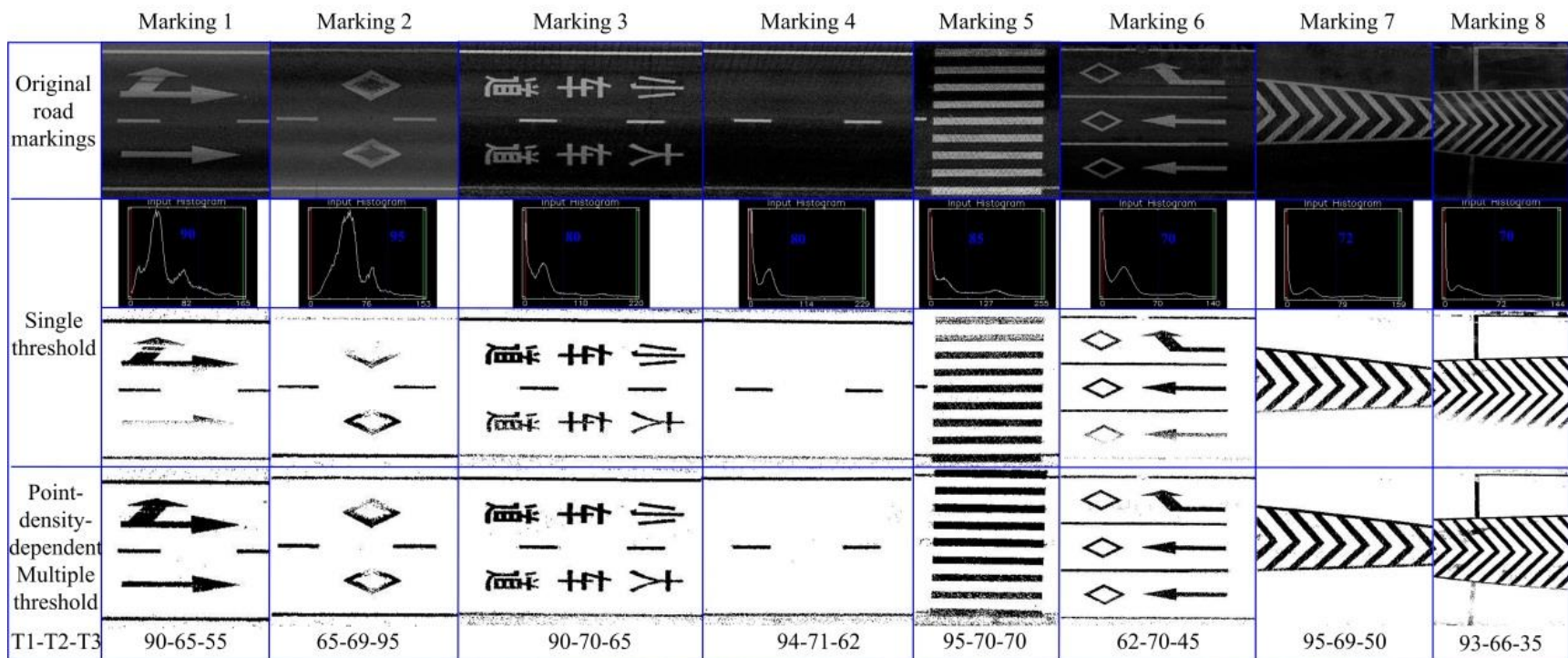
Figure 5.10: A comparison of the proposed method and the fixed segmenting threshold.
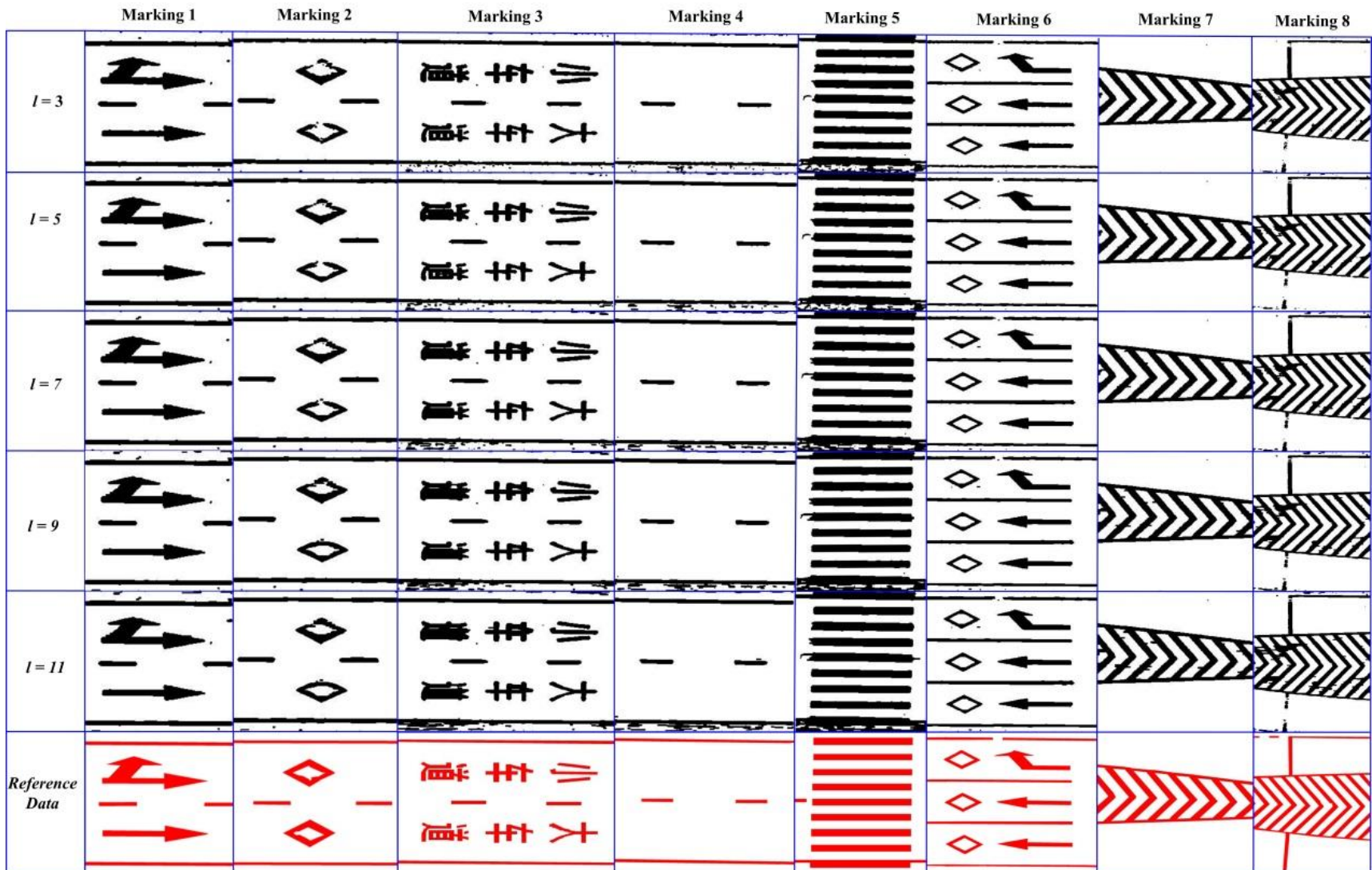
Figure 5.11: Sensitivity of structuring element size on the eight road markings.

Completeness of road markings

	3	5	7	9	11
Marking 1	0.98	0.98	0.98	0.99	0.99
Marking 2	0.88	0.89	0.90	0.92	0.93
Marking 3	0.97	0.98	0.99	0.99	0.99
Marking 4	0.99	0.99	0.99	1.00	1.00
Marking 5	0.92	0.92	0.93	0.94	0.94
Marking 6	0.96	0.97	0.97	0.98	0.98
Marking 7	0.97	0.98	0.98	0.98	0.99
Marking 8	0.94	0.94	0.95	0.95	0.95

Size of structuring kernel

(a)

Correctness of road markings

	3	5	7	9	11
Marking 1	0.82	0.81	0.80	0.79	0.78
Marking 2	0.87	0.86	0.85	0.83	0.82
Marking 3	0.84	0.82	0.79	0.76	0.73
Marking 4	0.82	0.80	0.75	0.72	0.69
Marking 5	0.89	0.87	0.85	0.84	0.84
Marking 6	0.93	0.92	0.90	0.89	0.88
Marking 7	0.95	0.94	0.93	0.92	0.91
Marking 8	0.91	0.90	0.88	0.87	0.85

Size of structuring kernel

(b)

F-Measure of road markings

	3	5	7	9	11
Marking 1	0.90	0.89	0.88	0.88	0.87
Marking 2	0.88	0.88	0.87	0.87	0.87
Marking 3	0.90	0.89	0.88	0.86	0.84
Marking 4	0.90	0.88	0.86	0.84	0.81
Marking 5	0.91	0.90	0.89	0.89	0.89
Marking 6	0.95	0.94	0.94	0.93	0.93
Marking 7	0.96	0.96	0.96	0.95	0.95
Marking 8	0.93	0.92	0.91	0.91	0.90

Size of structuring kernel

(c)

Figure 5.12: Sensitivity analysis of five structuring element sizes, ranging from 3 to 11: (a) completeness, (b) correctness, and (c) F-measure.

Figure 5.12 shows the measures of the road-marking extraction results on eight images with five different sizes of the structuring kernels. Results of all eight samples demonstrate that the completeness index *cpt* increases when the structuring-kernel size increases from 3 to 7, while the *cpt* remains stable when the structuring-kernel size is over 7. The correctness index *crt*, on the contrary, decreases with the increasing size of the structuring kernel. Particularly, the *crt* index of Marking 4 quickly declines, followed by Marking 3 (the word marking). The dilation operation causes this downward trend. As the structuring kernel increases in size, the dilation operation not only fills the holes in the road markings, but also merges small areas of noise into large areas of noise, and merges noise into the road markings. In this doctoral research, with an image resolution of $r_g = 4$ cm, the best size of the structuring kernel was gained at $l=3$.

5.3.3 Impact of Image Resolution

Because the road markings, under different image resolutions, will be presented with different details, the image resolution is one of the very critical parameters for extracting road markings. To evaluate the sensitivity of the image resolution relative to the performance of the road-marking extraction algorithm, one block data are selected from Huandao dataset and search a range of r_g (4 cm, 5 cm, 6 cm, 7 cm, 8 cm, 9 cm, and 10 cm) while keeping $\alpha = 0.5$, $\beta = 0.5$. The proposed road-marking extraction algorithm is applied to each test case.
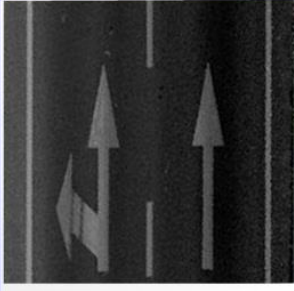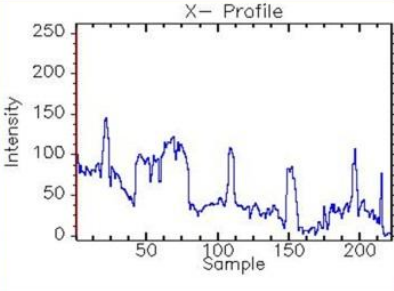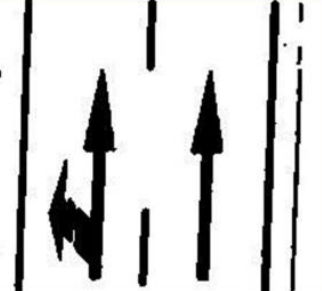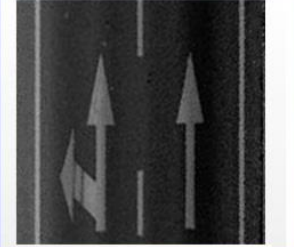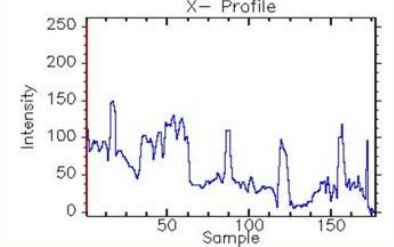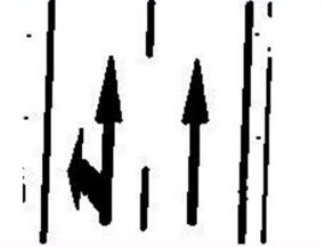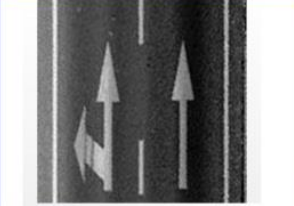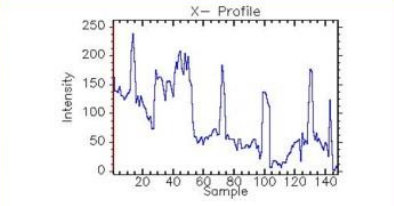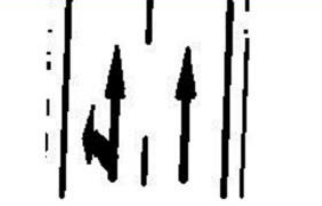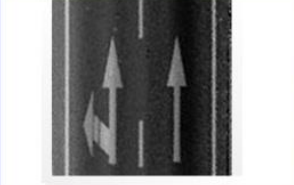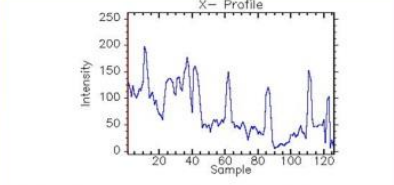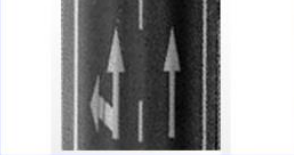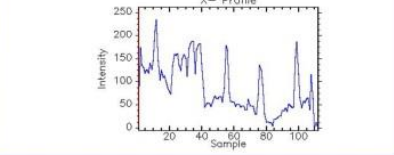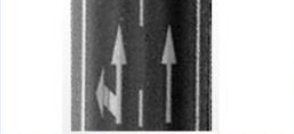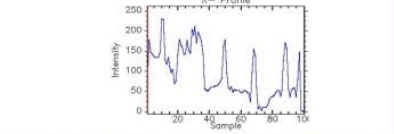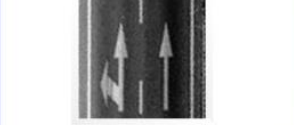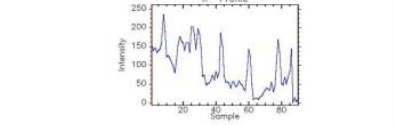
Figure 5.13 (a) shows the extracted road markings at seven image resolutions, ranging from 4 to 10 cm. The first column shows examples of the arrow-and-lane marking with seven image resolutions. Note that details of the arrow-and-lane marking are inversely proportional to image resolutions. The second column displays the X-profile

data of the arrow-and-lane marking. The horizontal axis represents the widths of the arrow-and-lane-marking image; the vertical axis represents the intensity values of pixels along the X-profiles. Note that the intensity values vary from one image to the other with the image resolution. Correspondingly, the segmentation thresholds are different from each other. Thus, the point-density-dependent multi-threshold method is suitable to automatically determine the segmentation thresholds for each image based on the weighted-intensity-difference (WID) method. As for the structuring element, $l = 3$ and $\theta = 28.46\,°$ calculated from the trajectory are applied to this case. The extracted road markings are shown in the third column. Visual inspection suggests that the shapes of the arrow-and-lane markings are preserved quite completely for seven test cases.

To assess the proposed road-marking extraction algorithm, a comparative analysis is carried out. The calculated *crt*, *cpt*, and *F-measure* indices are shown in Figure 5.13(b). For all the cases, the *crt* values are greater than 0.72, the *cpt* values are higher than 0.94, and the *F*-measure values range from 0.82 to 0.9. Note that there are slight changes in these three measure indices when the image resolution increases from 4 to 5 cm. However, the *crt*, *cpt*, and *F-measure* values slowly decrease when the image resolution is greater than 5 cm. Thus, the image resolution of either 4 or 5 cm is selected as the most applicable values to generate GRF images from RIEGL MLS data.

A complete assessment is conducted by comparing the differences between the extracted road markings and the actual measured road markings in length and width. To compare conveniently, four short lines were randomly selected from the broken lane markings. The actual length and width of the selected lane markings are measured and

checked with the official specification for road markings. Then, the measured is compared with the estimated by the proposed algorithm under seven image resolutions.

r_g(m)	Original road markings	X-profiles	Results
0.04			
0.05			
0.06			
0.07			
0.08			
0.09			
0.10			

(a)

116

Impact of image resolution on road markings

	0.04	0.05	0.06	0.07	0.08	0.09	0.10
cpt	0.98	0.97	0.95	0.95	0.96	0.94	0.94
crt	0.82	0.82	0.81	0.80	0.79	0.77	0.74
F	0.90	0.89	0.88	0.87	0.86	0.84	0.83
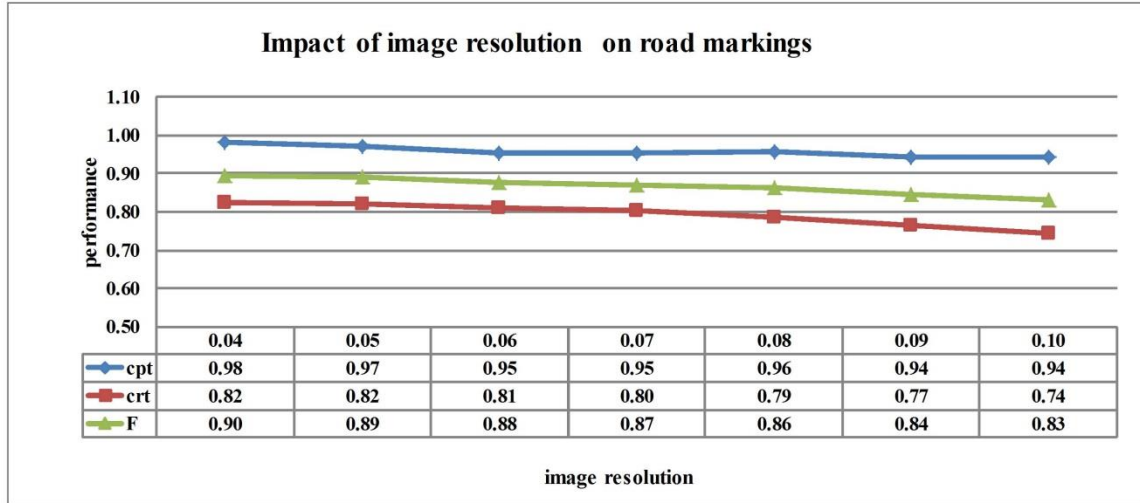
image resolution

(b)

Figure 5.13: Impacts of image resolution: (a) qualitative assessment, and (b) quantitative assessment using *cpt*, *crt*, and *F-measure*.

5.3.4 Overall Performance

Pursuant to a discussion of the sensitivity of parameters to the proposed algorithm, overall performance tests were conducted on Huandao and ICEC datasets. First, the proposed algorithm keeps R_g = 30 cm, S_p = 5 cm, S_g = 20 cm, G_{min} = 8 cm, and G_{max} = 30 cm, as listed in Table 5.1. Due to no sharp turns or curves of the roads in two cases, R_g is kept as 3.0 m. With R_g = 3.0 m, Huandao and ICEC datasets have 35 and 21 blocks and profiles, respectively. Afterwards, with local and global intensity information, this thesis uses α = 0.5, β = 0.5, and r_g = 4 cm to generate GRF images from MLS points belonging to the road surfaces.
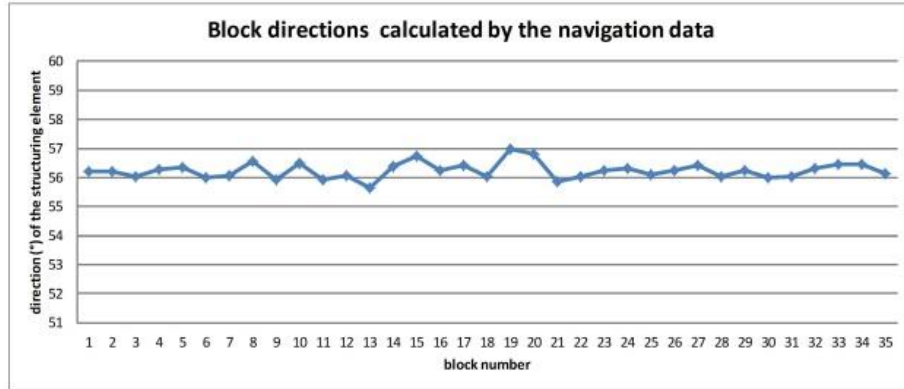
(a)
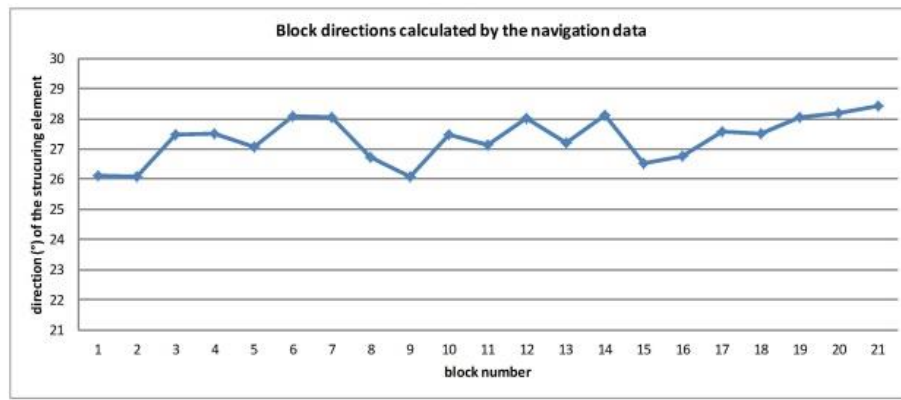
(b)

Figure 5.14: Orientations of the structuring element obtained by trajectory: (a) Huandao dataset, and (b) ICEC dataset.

In each block, the point-density-dependent segmentation method is employed to automatically obtain three thresholds for segmenting the possible road markings. For all blocks, the size of the structuring element l is 3, while θ is calculated by the trajectory. To simplify the task, a fixed value is provided for each block via the trajectory. Figure 5.14 shows the values of θ for the 35 blocks of Huandao and 21 blocks of ICEC datasets, respectively. After segmenting with multiple thresholds, a morphological closing operation is used to fill up the holes and remove the noise in the segmented road markings. The road markings extracted from the two cases are displayed and overlaid in the GRF image in Figure 5.15. Three samples are selected from two datasets as follows:

samples 1 and 2 from Huandao dataset and sample 3 from ICEC dataset to evaluate the proposed road-marking extraction algorithm. The close-up views of three samples show that the algorithm produces a completeness of road-marking extraction with less noise. The statistical results are listed in Table 5.3. Table 5.3 shows that the *F-measure* of the proposed method is consistently above 0.88. In addition, the *cpt*, *crt*, and *F-measure* do not change much among the three samples, indicating that the proposed method is robust to different types of road markings.
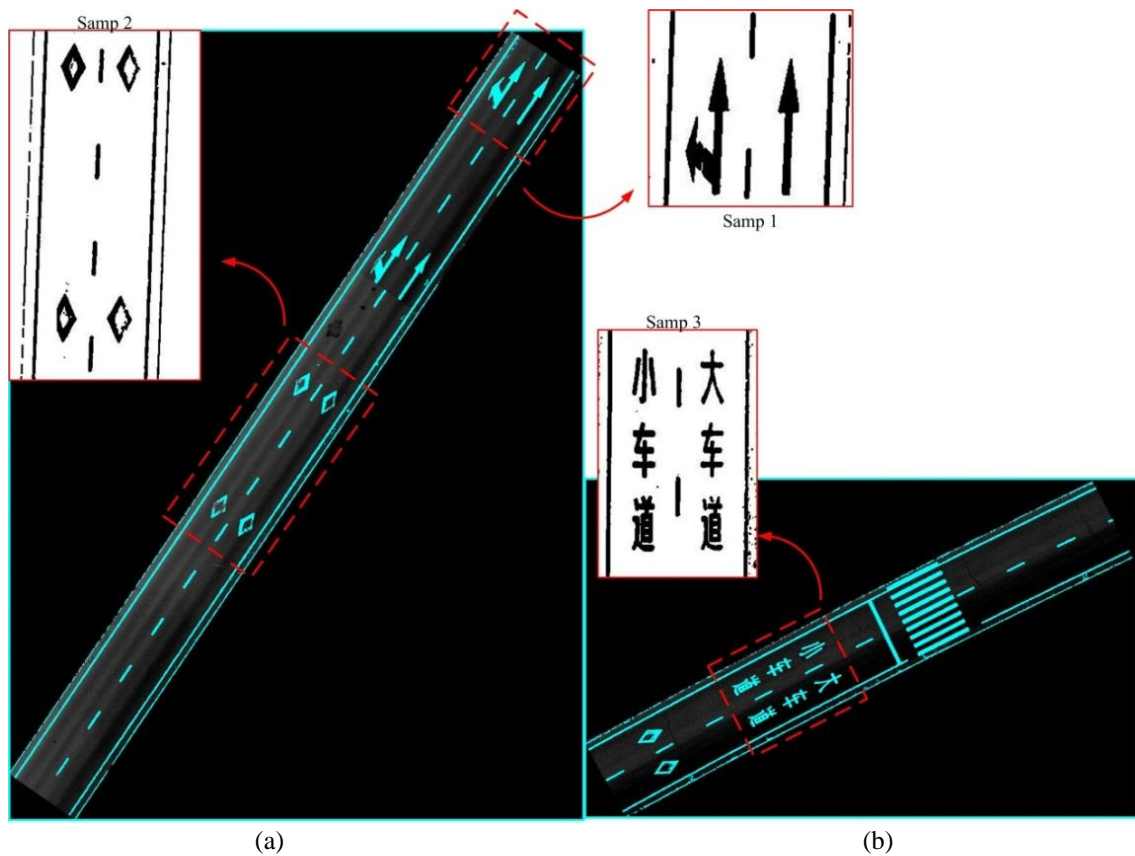
Figure 5.15: Extracted road-markings overlaid in the GRF images: (a) Huandao dataset, and (b) ICEC dataset.

Table 5.3: Performance of the proposed road-marking algorithm on two datasets.

		Sample	*cpt*	*crt*	*F-measure*
Huandao	Samp 1	0.98	0.82	0.89
	Samp 2	0.91	0.86	0.88
	All	0.94	0.83	0.88
ICEC	Samp 3	0.98	0.84	0.90
	All	0.97	0.82	0.90
Average		0.96	0.83	0.89

5.3.5 Computational Complexity

Through the use of a 3.30 Ghz Intel(R) Core(TM) i3-2120 CPU, the running time of the proposed method for processing the 8.4-million-point Huandao and 5.4-million-point ICEC datasets are about 1.11 and 0.89 seconds, respectively. The total running time does not include data profiling, which is the time of partitioning the raw data into a number of blocks and profiles. The reason is that the processing time of the data profiling is highly dependent on the reading-and-writing speed of the hard disk due to frequent data-interaction operations, as mentioned in Chapter 4. In this doctoral research, all extracting operations for road markings are performed in the GRF images, indicating that no data indexing structures need to be built for data querying and searching. Furthermore, the computation and processing time can be reduced if the stand-alone operation is replaced by a distributed processing system under a virtualization environment. Therefore, the reduced complexity, benefitting from the integration of the proposed road-marking processing algorithm and the affordable hardware, is a promising solution to computational efficiency of MLS data.

5.4 Discussion

This chapter presented an automated method for road-marking extraction from MLS data. The proposed method is based on the 2D GRF image that is interpreted from 3D road points using intensity information. The reason behind this is that road markings are painted on the road surfaces with high-reflectance material. In MLS data, road-marking points are attributed by high values of intensity, indicating that intensity thresholds can be used to segment and extract road markings from the 2D GRF image.

To this end, 3D road points that were extracted by the proposed curb-based road surface algorithm were first converted into a 2D GRF image. Different from ALS data, MLS data's point density drops perpendicular to the line of travel. The closer to the scanning centre, the higher the point density. Moreover, for some vertical structures such as building facades contains more points. MLS data cannot be generated into a 2D intensity image in a way that ALS data are usually interpreted into a range image. The point density is considered as an important factor for data interpolation. Thus, the IDW method was extended and improved for generating the 2D GRF image. The combination of local and global intensity information equalizes gray values of the image. Through this contrast adjustment, the intensity values were consistently distributed on the histogram. Experiments in Section 5.3.1 confirmed that (1) both intensity and distance contribute to the generation of the 2D GRF image, and (2) an integration of local and global intensity information improves the image contrast and equalization, benefiting road-marking extraction.

Second, although the proposed equalization strategy lessens intensity imbalance caused by point-density differences, the intensity values of road markings are not

consistent but gradually change from the scanning center to its two sides. This variation is because the reflected intensity values depend on (1) the scanning range from the laser sensor to the illuminated objects, (2) the incidence angle of the laser beam, and (3) the material properties of the illuminated objects. Thus, to successfully extract road markings, this chapter presented a point-density-dependent multi-thresholding method, where the road data are vertically sectioned into several bins according to the normal distribution function fitted by the point density data of a profile. With Otsu's method, a segmentation threshold is found for each bin. Rather than a universal threshold, multiple thresholds were applied to the 2D GRF image. Experiments in Section 5.3.1 showed that the threshold for each bin varies with each other. The use of a fixed threshold cannot obtain satisfactory thresholding segmentation results.

Moreover, the segmented road markings are incomplete and contain much noise. To remove noise and fill the holes, a morphological closing operation was used in the road markings. A linear structuring element was subsequently adapted for the shape of road markings. The direction θ of the selected linear structuring element was determined by the vehicle trajectory, and its size was determined empirically. The experiments in Section 5.3.2 showed that the best size of the structuring kernel was gained at $l=3$. With the morphological operation, the segmented road markings were improved by removing noise and filling holes.

The image resolution of the 2D GRF image is also a factor that affects the quality of the results of the road markings. In the perspective of image processing, the experimental results were validated using the measures, such as completeness, correctness, and F-measure. It can be found that, for all the cases, the *crt* values are greater than 0.72, the *cpt*

values are higher than 0.94, and the *F*-measure values range from 0.82 to 0.9. Moreover, the *crt*, *cpt*, and *F-measure* values slowly decrease when the image resolution is greater than 5 cm.

Through the use of a 3.30 Ghz Intel(R) Core(TM) i3-2120 CPU, the running time of the proposed method for processing the 8.4-million-point Huandao and 5.4-million-point ICEC datasets are about 1.11 and 0.89 seconds, respectively. Overall performance tests with empirically-selected parameters showed that the proposed road-marking extraction algorithm was able to extract road markings in a 0.96 completeness rate, a 0.83 correctness rate, and a 0.89 F-measure rate. The false detections occurred at the places of lane marking close to the curbs. The main reason could be the following factors: (1) the image resolution of the 2D GRF image, and (2) cracks that break the continuous and long road markings down into several short road markings, leading to be enlarged by the morphological closing operation. Thus, pavement cracks will be discussed and the algorithm for crack extraction will be presented in Chapter 6.

5.5 Chapter Summary

This chapter proposed a road-marking extraction algorithm from MLS data, which consists of (1) the extraction of road surfaces, (2) the generation of GRF images with a histogram equalization-like strategy, and (3) the extraction of road markings using point-density-dependent multi-thresholding segmentation and morphological closing operation.

The two datasets collected by RIEGL VMX-450 were used in this research for the validation of the proposed method. The two test datasets cover a total length of around 168 m of the road that contains at least eight types of road markings. The experimental

results demonstrated that the proposed method is able to extract road markings with a completeness of 0.96, a correctness of 0.83, and an F-measure of 0.89.

The proposed method for extracting road markings can deal with large volumes of MLS data because (1) no data indexing structures are involved for searching and querying, (2) the extracted road surface serves a prior knowledge that facilitates the road-marking processing and improves the correctness of road markings, (3) a combination of local and global intensity weights contributes to the generation of the 2D GRF image, and (4) the proposed algorithm overcomes inconsistent intensity values caused by the incidence angle of laser pulses, and the scanning range of the scanner center to the illuminated road surface.

Chapter 6 Pavement-crack Extraction[3]

This chapter details the algorithm for the automated extraction of pavement cracks from MLS data. The crack extraction algorithm applies ITV to high density point clouds. The crack extraction algorithm comprises (1) pre-processing, detailed in Chapters 4 and 5, (2) crack candidate extraction by a weighted intensity difference (WID) thresholding algorithm, (3) crack enhancement by ITV, and (4) crack extraction by a morphological thinning algorithm. These steps for crack extraction are presented in Section 6.1. Validation is presented in Section 6.2. Empirical and comparative experiments are described and analyzed in Section 6.3. Discussions are presented in Section 6.4. Section 6.5 provides a summary of this chapter.

6.1 Algorithm Description

The objective of this chapter is to develop a crack extraction algorithm, analyze its performance on a variety of crack types selected from MLS data and pavement images, and compare it with other algorithms. The proposed algorithm is seen as a stepwise procedure for interpreting MLS data, as shown in Figure 6.1. The algorithm mainly includes the following four steps:

---

[3] The main work presented in this chapter has been submitted by, Guan, H., Li, J., Yu, Y., Chapman, M., and Wang, C., 2013. Interactive tensor voting method for crack detection using mobile laser scanning data. *IEEE Transactions on Geoscience & Remote Sensing* (under the 3rd round review).
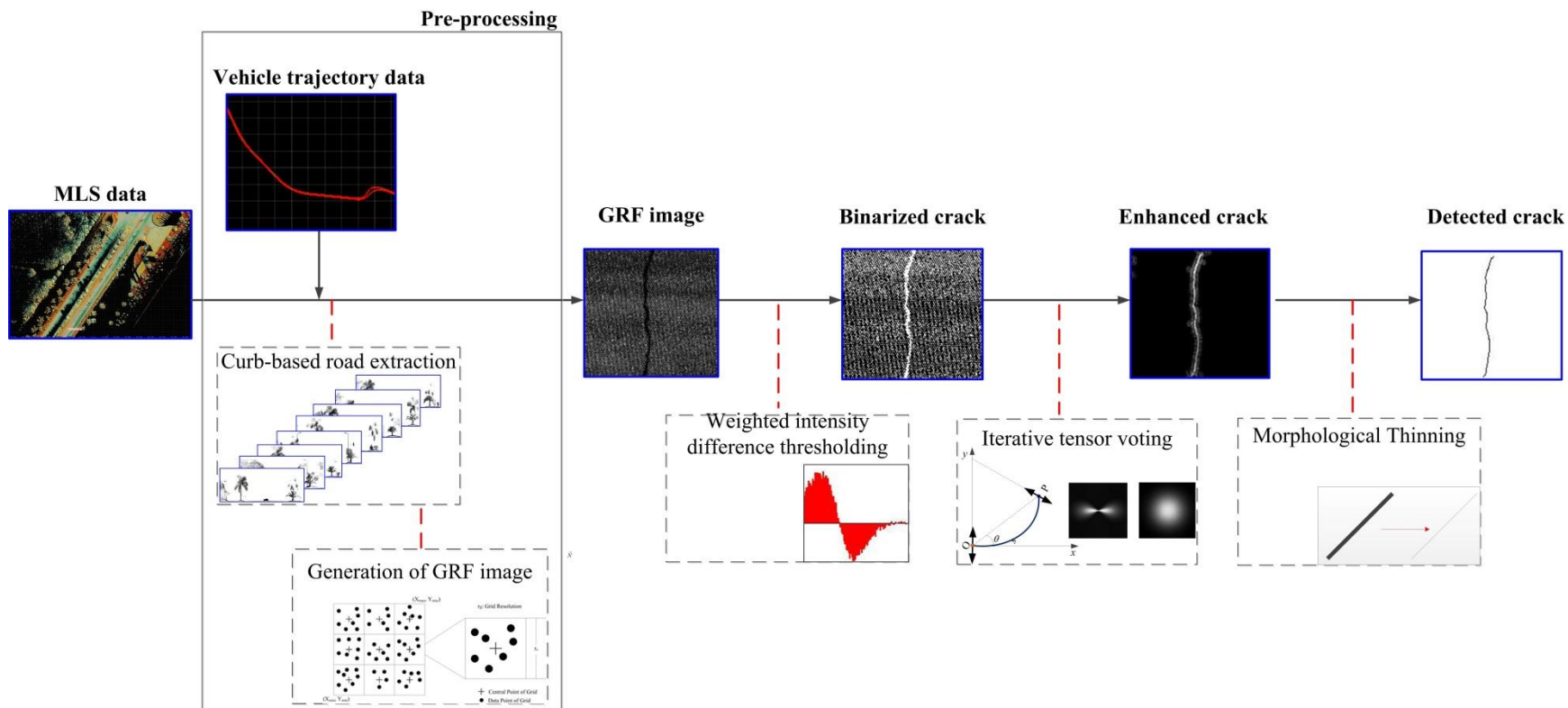
Figure 6. 1: An overview of the proposed ITV-based crack extraction algorithm.

(1) Pre-processing: Curb-based road-surface extraction and GRF generation are applied to MLS data.

(2) Thresholding: a weighted intensity difference (WID) method is applied to the generated GRF image for extracting crack candidates.

(3) Crack enhancement: ITV is applied to the noisy GRF image for enhancing cracks.

(4) Morphological thinning: a morphological thinning algorithm extracts the enhanced cracks from the background.

6.1.1 Pre-processing

The raw MLS data are partitioned, based on the vehicle trajectory, into blocks and their corresponding profiles, by which pseudo scan-lines are formed to detect small height jumps caused by road curbs. The segmented road points are interpolated into the GRF image via an extended IDW method that combines local-and-global elevation and intensity data, as shown in Figure 6.2. These algorithms for automatically extracting road surfaces and generating GRF images have been detailed in Chapters 4 and 5, respectively.

(a)   (b)
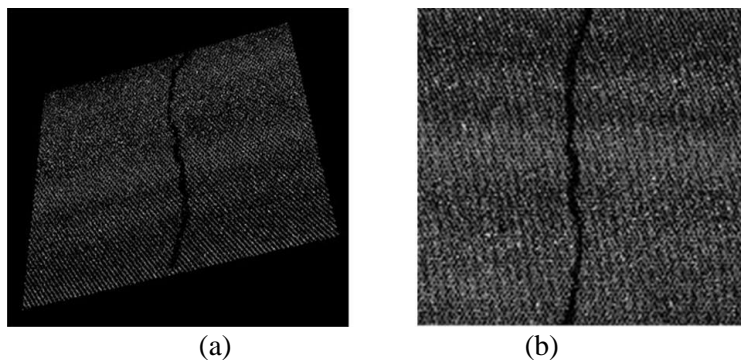
Figure 6. 2: The generation of GRF images: (a) 3D MLS data, (b) the generated GRF image.

6.1.2 Thresholding Segmentation

As asphalt pavement mainly contains (i) large aggregates that probably vary with geological regions, and (ii) asphalt mix that is made up of a variety of chemical components. Thus, the increasing surface roughness and shadows cause reflectance differences of up to 7-8 % in the near-infrared between the actual pavement and high severity cracks (Martin 2008). In addition, the concave-shaped cracks in the visible/near-infrared make non-cracked road brighter. Furthermore, compared to road surfaces, deeper layers exposed by cracks contains higher proportion of the original asphalt mix, leading to an increase of hydrocarbon absorption features that highlight their contrast spectral signals. Thus, the visual appearance of cracks in the near-infrared range is usually darker than that of the normal road surface. Based on this observation, the optimal threshold could be found to segment potential crack pixels from non-crack pixels by making use of image histograms and an objective function derived from information theory. Without noise, it would be successful to segment cracks from the background by means of a bimodal histogram structure. However, a huge amount of noise is scattered in the GRF image. Therefore, the image histogram in Figure 6.3 displays no obvious peaks and valleys, resulting in the issue of finding the optimal separation value (T_E). As a result, a WID method is adopted to detect crack candidates by maximizing the information measures between crack and non-crack pixels.
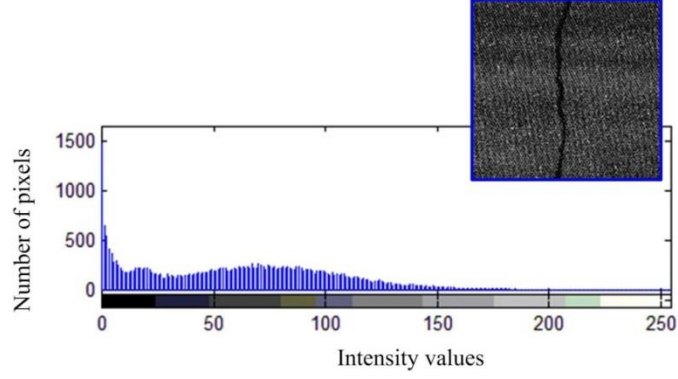
Figure 6.3: Histogram analysis for GRF image.

The WID method first computes the intensity difference of a pixel with its nearest neighbors to reflect the contrast of this pixel with its neighbors. Afterwards, WID sums up all the difference measures for each gray level to reflect the entire difference of a gray level in the image. With a weighted scheme, WID can avoid the effects of the noise and reflect a general difference measure.

The weighted intensity difference method is described as:

$$d(i,j) = \frac{\sum\limits_{m=-k}^{k} \sum\limits_{n=-k}^{k} \left[\left| G_{i+m,j+n}^{I} - G_{ij}^{I} \right| \cdot (G_{i+m,j+n}^{I} - G_{ij}^{I}) \right]}{\sum\limits_{m=-k}^{k} \sum\limits_{n=-k}^{k} \left| G_{i+m,j+n}^{I} - G_{ij}^{I} \right|} \qquad (6.1)$$

where, G_{ij}^{I} is the intensity value of pixel (i,j), and $d(i,j)$ is the weighted neighboring difference value of pixel (i,j). The neighborhood size selected for calculating $d(i,j)$ is $2k+1(k>0)$. Then, a WID function $H(l) = \sum\limits_{G_{ij}^{I}=l} d(i,j), l \in [0,255]$ is defined to reflect the total intensity-difference measure over all pixels with intensity l, and select the gray level corresponding to the maximal value of the WID function as an optimal segmentation threshold $T_i (i=1,2,3)$ to safely identify the possible road markings:

$$T = arg \max_{l} H(l) \qquad (6.2)$$

129

6.1.3 Iterative Tensor Voting Framework

Figure 6.4 shows the flow chart of the ITV-based crack extraction algorithm. After thresholding, we assume that $P = \{p_1, p_2, p_3..., p_i,...p_n\}$ is the crack candidate data set, where n is the number of crack candidates; p_i is the ith crack candidate. First, as crack candidate p_i has no orientation preference, it is initially encoded by a ball tensor with unit saliency, in the form of the 2×2 identity matrix. After the construction of the tensor space, the first round of sparse voting is performed using the ball voting field with σ_{ball}.
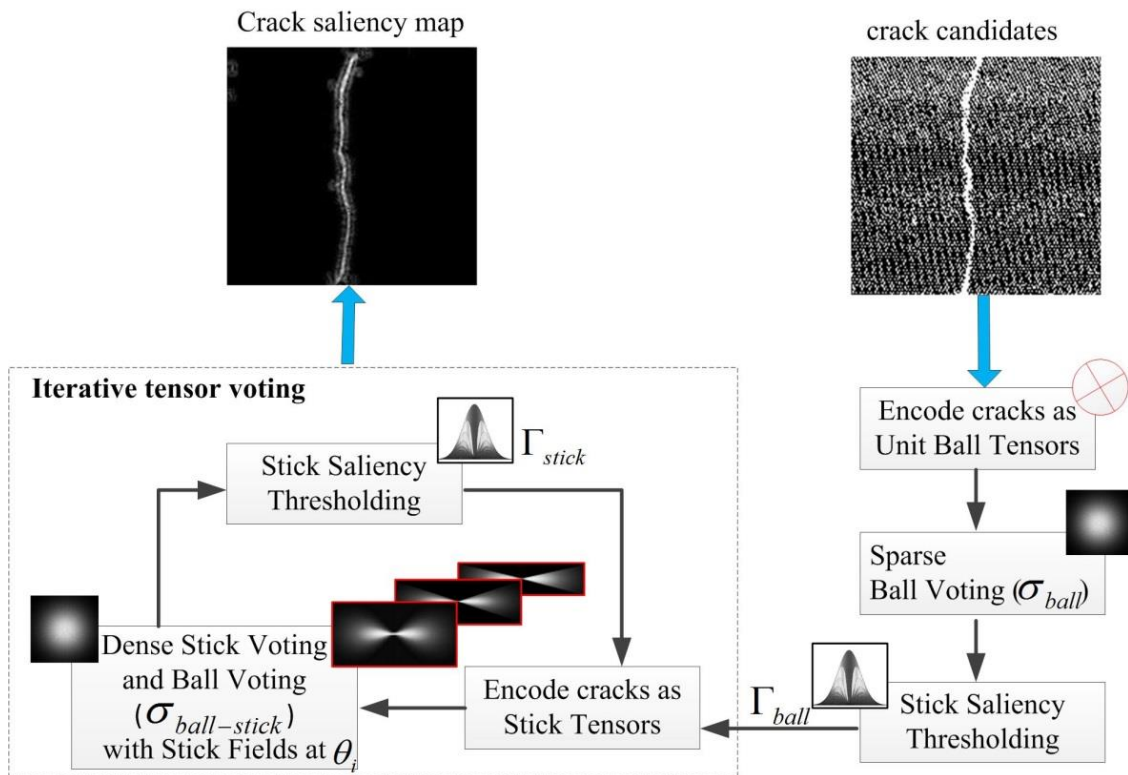
Figure 6. 4: The proposed ITV algorithm for crack enhancement.

After the large-scale sparse ball voting process, all the tensors corresponding to the crack candidates obtain rough orientations (e_1 and e_2) and magnitudes (λ_1 and λ_2).

130

However, the mapped cracks are inaccurate and lack saliency, a round of stick voting is required to refine the orientations and to obtain a saliency map of cracks. Curvilinear structures in tensor representation by nature should have high $\lambda_1 - \lambda_2$ values, which means crack candidates with $\lambda_1 - \lambda_2$ values that are smaller than the ball-saliency threshold Γ_{ball} are ruled out in this step. Eliminating the tensors with low stick saliencies can increase computational efficiency because fewer crack candidates will participate in ball-and-stick voting.

Each oriented crack candidate is further encoded as a stick tensor. A round of dense voting is then executed using the stick field. Note that, according to eigen-decomposition, although ball tensors have no orientation preferences, they can still cast meaningful information to other tensors, contributing to the concentration of saliency. For example, a potential curve could be influenced by two nearby ball tensors. Thus, we adopt both ball voting and stick voting using the stick voting field with $\sigma_{ball-stick}$ for the saliency map.

Usually, after the dense ball and stick voting process, curvilinear structures are enhanced on the resulting saliency map. However, the cracks of interest were presented with much noise and a low contrast with their surroundings. Only one round of dense ball-and-stick voting (namely, a combination of ball voting and stick voting) could not achieve a good saliency map for the cracks. An iterative scheme is thus proposed to gradually refine the previous results of the dense ball-and-stick voting.

For each iteration, dense ball-and-stick voting is employed using the stick voting field with $\sigma_{ball-stick}$. A stick saliency thresholding similar to the aforementioned ball saliency thresholding is subsequently used to remove the resultant tensors with low $\lambda_1 - \lambda_2$

values. That is, only the tensors with $\lambda_1 - \lambda_2$ values larger than the stick threshold Γ_{stick} will go to the next iteration. As such, each iteration refines the previous one. With the iterative scheme, the tensors with high $\lambda_1 - \lambda_2$ values seem to be concentrated and accurate with little disturbance and interference from the tensors with low $\lambda_1 - \lambda_2$ values; thus, we call this iterative tensor voting (ITV).

Using dense ball-and-stick voting, the curvilinear structure becomes gradually more concentrated and accurate as the number of iterations increases, which means the field aperture θ for the stick field can be correspondingly reduced to focus on the promising votes for enhanced results. For the stick field, let θ_{max} and θ_{min} denote the maximum and minimum field apertures, respectively, and $\Delta\theta$ the voting aperture step. The number of iterations can be calculated as: $N = (\theta_{max} - \theta_{min})/\Delta\theta + 1$. For example, for the ith iteration, we employ the stick field with the field aperture of θ_i ($\theta_i = \theta_{max} - (i-1)\Delta\theta$) for dense voting. Apart from assigning the voting aperture step for calculating the number of iterations, we can also empirically pre-define N to stop the iterative processing. Finally, with ITV, a refined crack probability map is generated to enhance the crack pixels; at the same time, suppressing the background and the noise.

6.1.4 Morphological Thinning

To further remove noise and obtain cracks in the crack probability map, a 4-pass-per-iteration morphological thinning algorithm was applied in this section (Parvin et al., 2007). The algorithm serves to thin a binary crack image down to its median axes, by peeling off boundary pixels of the crack. After the implementation of the algorithm

proposed in [35], the proposed algorithm produces a converged, 8-connected, one-pixel-thick skeleton.

6.2 Validation

To quantitatively evaluate the crack results, a buffered Hausdorff distance metric ($H(A, B)$) is used by comparing the detected cracks with the human labelled cracks (Tsai et al., 2010). $A = \{a_1, a_2, \cdots, a_p\}$ and $B = \{b_1, b_2, \cdots, b_q\}$ are the finite pixel sets corresponding to the same locations within the extracted crack image and the human labelled image, respectively. The Hausdorff distance metric is given by

$$H(A, B) = \max(h(A, B), h(B, A)) \tag{6.3}$$

where

$$h(A, B) = \max_{a \in A} \min_{b \in B} \|a - b\| \tag{6.4}$$

And $\|\bullet\|$ is a Euclidean norm on the pixel sets A and B. The function $h(A, B)$ is called the directed Hausdorff distance from A to B, describing the degree of difference between two shapes. $h(A, B)$ identifies the point $a \in A$ farthest from any points in B and measures the distance from a to its nearest neighbors in B. Essentially, $h(A, B)$ ranks each point in A based on its distance from the nearest point in B, and then uses the distance corresponding to the highest ranked point. A buffer of size L is used to create a searching region, within which the Hausdorff distance metric is adopted to evaluate the crack extraction performance based on the ground truth. The scoring measure (SM) is calculated for the evaluation of cracks as follows (Huttenlocher et al., 1993):

$$SM = 100 - \frac{H(A, B)}{L} \times 100. \tag{6.5}$$

The value of SM ranges from 0 to 100. The higher the value of SM, the better the crack extraction performance. Considering the cracks in the test datasets were not wider than 3 pixels, $L=5$ pixels is assigned for computing the values of SM.

6.3 Experiments

The stability and capability of the proposed algorithm were evaluated using synthetic data, pavement images, and GRF images. To objectively evaluate the performance, the manual interpretations of the crack curves in these images were used as the ground truth.

6.3.1 Synthetic Data Tests
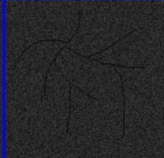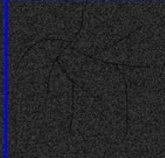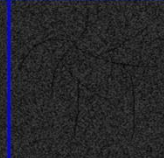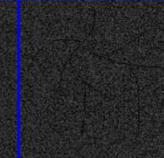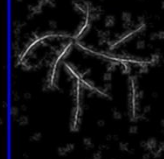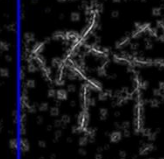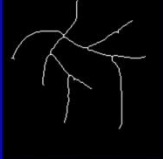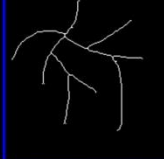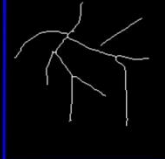
To evaluate the applicability of the proposed algorithm, two groups of synthetic data were created with different noise models. The first group was generated with the standard additive white Gaussian noise (AWGN) model, while the second group was created with the multiplicative Gamma noise model. In many cases, noise in pavement images is found to be additive in nature with uniform power in the whole bandwidth following the Gaussian probability distribution. In addition, multiplicative Gamma noise, in the form of speckles, normally appears in laser-based images, thus degrading the quality of the images and affecting the performance of the image processing techniques (Hawwar and Reza, 2002). All synthetic images are 200×200 pixels.

Figures 6.5 (a) and (b) show two groups of synthetic images corrupted with additive and multiplicative noise at different variances, respectively, with the parameters $\sigma_{ball} =10.0,$ $\sigma_{ball-stick} =3.0,$ $\Gamma_{ball} =0.4,$ $\Gamma_{stick} =0.05,$ and $\Delta\theta =20°$. All parameters were defined by visual inspection of the sample results, and were used for two groups of the synthetic image data sets as well as throughout the following comparative experiments.

As shown in Figure 6.5 (a), the synthetic data are corrupted by a set of additive noise following a zero-mean normal distribution ($m=0$) with five different variances ($\sigma=0.1, 0.2, 0.3, 0.4, 0.5$). In this group, the SM values of the detected curves are over 97 for all five values of σ, demonstrating that the developed crack extraction algorithm is noise robust and capable of preserving the details of curvilinear structures. In Figure 6.5(b), the synthetic data are corrupted by a set of multiplicative noise at five different variances ($\sigma=0.05, 0.10, 0.15, 0.20, 0.25$). The SM values of all five detected curves are over 95, again, indicating that the proposed algorithm can handle cracks, which have low contrasts with their surroundings (such as asphalt concrete-surfaced pavements) in the GRF image.

	Noise-free	$m=0$ $\sigma=0.1$	$m=0$ $\sigma=0.2$	$m=0$ $\sigma=0.3$	$m=0$ $\sigma=0.4$	$m=0$ $\sigma=0.5$
Synthetic data with noise						
Curve probability map						
Morphological thinning results						
SM	99.21	99.20	99.19	98.95	98.09	97.21

(a)

	Noise-free	$\sigma = 0.05$	$\sigma = 0.10$	$\sigma = 0.15$	$\sigma = 0.20$	$\sigma = 0.25$
synthetic data with noise						
Curve probability map						
Morphological thinning results						
SM	99.21	99.04	99.23	97.72	97.37	95.5

(b)

Figure 6. 5: Two groups of synthetic data: (a) synthetic data with additive Gaussian white noise, and (b) synthetic data with multiplicative gamma noise.

6.3.2 Overall Performance

To accurately and precisely detect these cracks in the GRF image, overall performance tests are conducted on Huandao dataset that contains small cracks with a few centimetres in width extending to large alligator cracks up to the size of 10 cm. Figure 6.6 shows the extraction results of Cracks 1 to 5 selected from the GRF image with the image resolution of 2 cm. Cracks 1, 2 and 5 have a size of 200×200 pixels, and Cracks 3 and 4 have a size of 250×150 pixels.

This overall performance test set σ_{ball}=10.0, $\sigma_{ball-stick}$=3.0, Γ_{ball}=0.4, Γ_{stick}=0.05, and $\Delta\theta$=20° for crack extraction. The row of the binary crack images suggests that simple threshoding methods or conventional edge detection algorithms are unable to extract the cracks with low SNRs and low contrasts with their surroundings. With the proposed algorithm, the curvilinear cracks are enhanced and their surrounding noise is

136

suppressed or removed, as shown in the row of curve probability map. The extracted cracks show that the curve probability map contributes to the extraction of the cracks via the morphological thinning algorithm. Visual inspection demonstrates that the extracted cracks are consistent with the original GRF images, as shown in the last four rows in Figure 6.6. Quantitatively, the SM values of around 95% for five cracks reveal that the proposed ITV-based crack extraction algorithm can handle complex cracks with low contrast and poor continuity.

	(a)	(b)	(c)	(d)	(e)
SM	97.32	95.64	94.14	96.64	95.79
Computational time (s)	340	435	1341	646	401

Figure 6. 6: Crack extraction results: (a) Crack 1, (b) Crack 2, (c) Crack 3, (d) Crack 4, and (e) Crack 5.

6.3.3 Sensitivity Tests with Parameters

There are five parameters used in the proposed ITV-based crack extraction algorithm: σ_{ball}, $\sigma_{ball-stick}$, Γ_{ball}, Γ_{stick}, and $\Delta\theta$. Among them, Γ_{ball} and Γ_{stick}, thresholds, are used to delete tensors with low stick saliencies and preserve tensors with high stick saliencies after the sparse ball voting and the dense ball-and-stick voting in the iterations, respectively. Empirical experiments present Γ_{ball}=0.4, Γ_{stick}=0.05 by histogram analysis. σ_{ball} and $\sigma_{ball-stick}$, scales of voting, control the neighborhood sizes for the sparse ball voting and the dense ball-and-stick voting in the iterations, respectively. Thus, they have a great impact on the performance of the proposed algorithm because they decide how many pixels can be used for tensor voting. Parameter σ_{ball} is generally given a larger value to decrease the influence of noise in the sparse voting, while in the iterative process, parameter $\sigma_{ball-stick}$ is given a small value to preserve crack details. In addition, the voting aperture step $\Delta\theta$ used to control the iterations importantly influences crack enhancement. Thus, three groups of experiments are designed by varying the values of the scale parameters σ_{ball}, $\sigma_{ball-stick}$, and the voting aperture step $\Delta\theta$.

The first group of tests kept $\sigma_{ball-stick}$=3.0, Γ_{ball}=0.4, Γ_{stick}=0.05, $\Delta\theta$=20° and varied σ_{ball} from 10.0 to 6.0 with an interval of 1.0. Figure 6.7 (a) shows the experimental results for these five cracks. As shown in Figure 6.7 (a), the SM values of detected cracks dramatically vary with the parameter σ_{ball}, which increases from 6.0 to 9.0. However, the SM values tend to be stable with the parameter σ_{ball} changes from 8.0 to 10.0. The reason behind this phenomenon might be that a large scale prefers long range interactions, leading to a higher degree of smoothness (that is, more noise is

removed), thus improving extraction performance. In fact, the best cracks could be obtained at $\sigma_{ball}=9.0$ or 10.0 for this research.
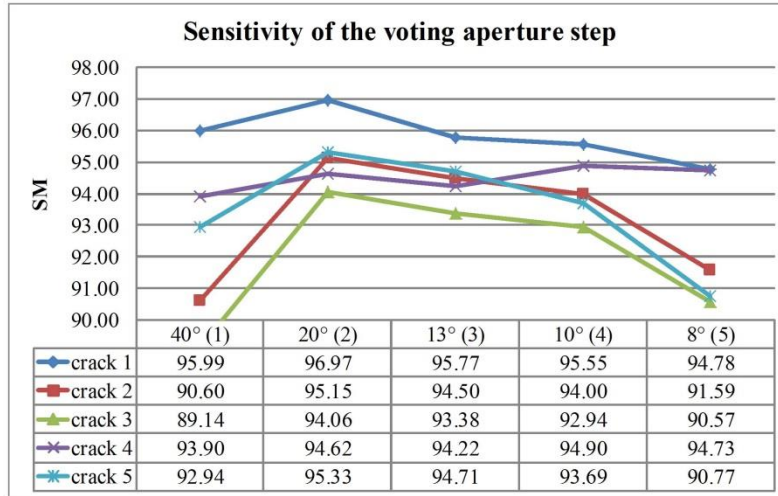
The second group of tests kept $\sigma_{ball}=10.0$, $\Gamma_{ball}=0.4$, $\Gamma_{stick}=0.05$, $\Delta\theta=20\,^{\circ}$ and varied $\sigma_{ball-stick}$ from 3.0 to 6.0 with an interval of 1.0. Figure 6.7 (b) shows the experimental results for these five cracks. As shown in Figure 6.7 (b), when $\sigma_{ball-stick}$ is 3.0, the proposed algorithm achieved a relatively stable performance, indicated by the SM values being higher than 95%. The values of SM quickly decreased with $\sigma_{ball-stick}$ increased from 4.0 to 7.0. This is because unlike σ_{ball} in the sparse voting, which is given a larger value to remove noise, $\sigma_{ball-stick}$ in the iteration process requires a smaller scale to preserve crack details. Due to the large amount of noise removal by σ_{ball} in the sparse voting process, iterative dense voting is able to enhance the cracks by preserving their details. In this study, the $\sigma_{ball-stick}$ value of 3.0 obtained the best crack extraction performance.

Sensitivity of sigma in the sparse ball voting process

	6	7	8	9	10
crack 1	96.98	97.17	95.57	97.37	97.32
crack 2	93.62	94.73	94.86	96.19	95.64
crack 3	93.53	92.38	94.47	93.80	94.14
crack 4	96.71	95.88	96.87	96.22	96.64
crack 5	96.04	95.02	95.83	94.94	95.79

(a)

Sensitivity of sigma in the dense voting process

	3	4	5	6	7
crack 1	97.32	95.96	93.10	88.86	88.25
crack 2	95.64	94.72	91.62	92.05	92.68
crack 3	94.14	92.29	90.81	90.11	88.82
crack 4	96.64	95.14	94.46	90.60	92.79
crack 5	95.79	94.77	93.72	92.45	91.01

(b)

Sensitivity of the voting aperture step

	40° (1)	20° (2)	13° (3)	10° (4)	8° (5)
crack 1	95.99	96.97	95.77	95.55	94.78
crack 2	90.60	95.15	94.50	94.00	91.59
crack 3	89.14	94.06	93.38	92.94	90.57
crack 4	93.90	94.62	94.22	94.90	94.73
crack 5	92.94	95.33	94.71	93.69	90.77

(c)

Figure 6. 7: Sensitivity tests with the parameters: (a) σ_1, (b) σ_2, and (c) $\Delta\theta$.

The last group of tests kept σ_{ball} =10.0, $\sigma_{ball-stick}$ =3.0, Γ_{ball} =0.4, Γ_{stick} =0.05 and

varied $\Delta\theta$ from 8° to 40° at 5 different $\Delta\theta$ settings (that is, 40°, 20°, 13°, 10°, 8°). This

group applied the maximum field aperture θ_{max} =45° and the minimum field aperture θ_{min}

= 5°. As the voting aperture step $\Delta\theta$ determines the number of iteration (N) in the

dense voting process, according to equation $N = (\theta_{max} - \theta_{min})/\Delta\theta + 1$, the proposed

algorithm is performed at 5 different iterations (1,2,3,4,5). As shown in Figure 6.7 (c),

when $\Delta\theta$ is between 10° and 15°, which entails 3 or 4 iterations, the SM values of all

five cracks indicate good performance. The philosophy behind this phenomenon is that, in the iterative dense voting process, each iteration refines the previous one by gradually reducing the diffusion of votes and focusing the votes on only promising curves. It has been found, however, that although the dense voting allows pixels to be interpolated for filling discontinuity, excessive number of iterative dense tensor voting (small $\Delta\theta$) would produce smoother crack curves due to over interpolation. Consequently, some details of cracks would be missed, resulting in a decrease of SM values.

6.3.4 Comparative Tests with Pavement Images

To further evaluate the performance of the proposed algorithm, it is compared with two newly proposed crack extraction methods, FoSA (F* seed growing) (Li et al., 2011) and CrackTree (Zou et al., 2012). Tsai et al. (2010) compared six image segmentation methods for crack extraction and suggested that dynamic optimization-based methods outperformed the other five methods for segmenting low SNR images. Thus, the dynamic optimization was selected for comparison (Huang and Tsai, 2011). In pursuance of the objectives of this study an experimental study was conducted by the author to compare the performance of various crack extraction methods developed to date. It is accepted that crack detectors will not be perfect and universally applicable. Although most of them can work under most situations and with most data types, they will fail under certain environmental conditions. Thus, two groups of comparative experiments are conducted for assessing these crack extraction methods. The first group is pavement image based comparative test, and the second one is GRF based comparative test. The two comparative experiments set $\sigma_{ball}=10.0$, $\sigma_{ball-stick}=3.0$, $\Gamma_{ball}=0.4$, $\Gamma_{stick}=0.05$, and $\Delta\theta=20°$, according to the discussion in Section 6.3.3.

The pavement images were taken by Canon IXUS 125HS, with the sizes of 1600 ×1200 pixels in this group study. Figure 6.8 shows the results obtained using each of the four existing crack extraction methods. Table 6.1 lists the SM values of the extracted cracks, in comparison with the crack truth. In the CrackTree method, the parameters were selected to be: the voting scale $\sigma=11$, the edge length threshold $L_e=10$, and the path length threshold $L_p=60$. The FoSA algorithm keeps the searching radius being 24. As shown in Table 6.1, given the high spectral and spatial resolutions of the pavement images, most algorithms achieve good performance in crack extraction. However, the FoSA algorithm achieves a lower SM value (76.09) for Image 2, compared to the other images. This might be spectral inconsistency around the crack in Image 2. Thus, this algorithm mistakenly identified the boundary of the slightly dark area as a crack, leading to a high rate of false alarm.
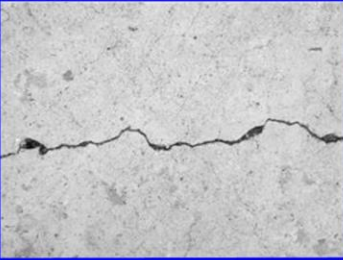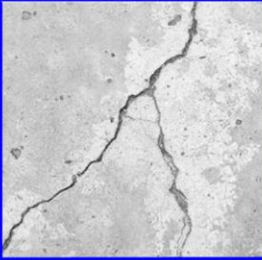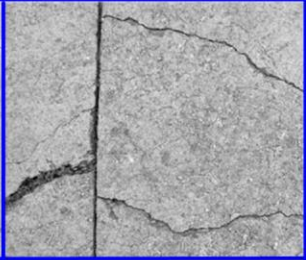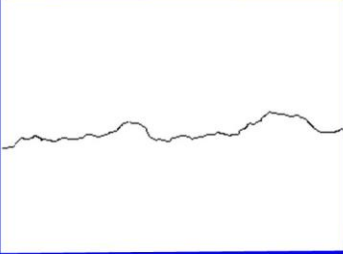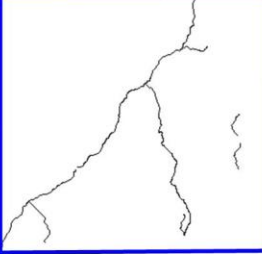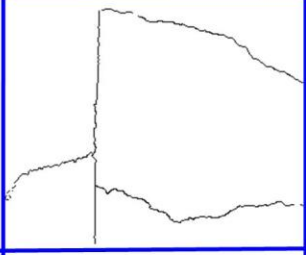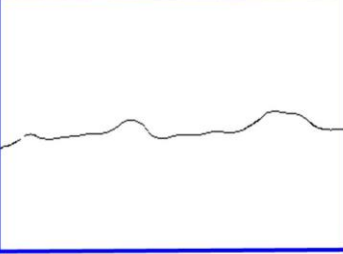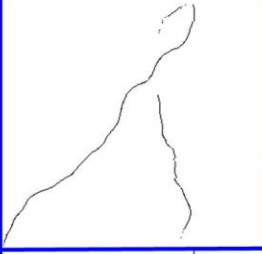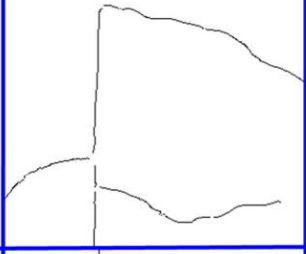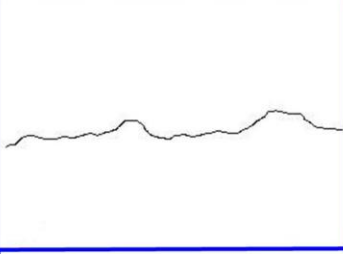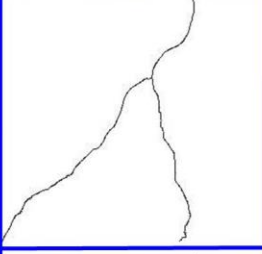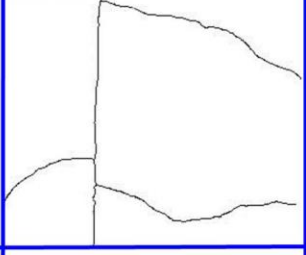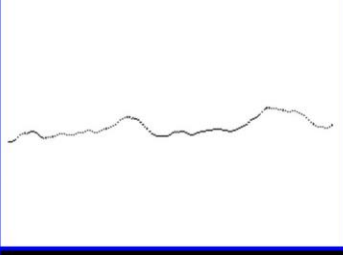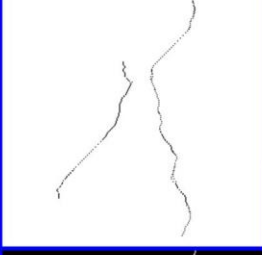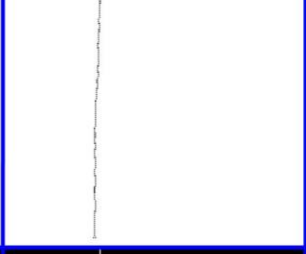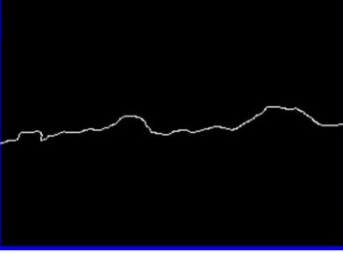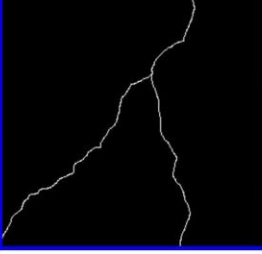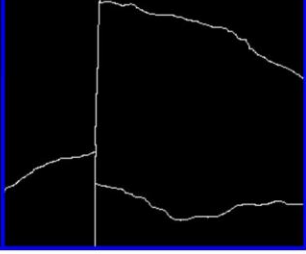
Figure 6. 8: A comparison of the proposed algorithm with the other algorithms using pavement images: (a) Image 1, (b) Image 2, and (c) Image 3.

Table 6.1: SM values of the four crack extraction methods using pavement images.

	Image 1	Image 2	Image 3
The proposed ITV-based algorithm	93.13	90.04	91.64
CrackTree	93.54	89.17	89.66
FoSA	92.98	76.09	92.75
Dynamic optimization	94.22	78.38	33.77

Similarly, the dynamic optimization deals poorly with Image 3, as indicated by the SM value of 33.77. This might be caused by a low contrast between the crack pixels and their surroundings. The dynamic optimization method using connected component analysis detects crack regions of interest from local crack information, such as density, relative area, bounding box, and line similarity. For this reason, low contrast in a local window might cause the algorithm to inadequately extract adequate crack information for connected component analysis. As expected, the proposed crack extraction algorithm attains a stable performance for all three crack images. Qualitatively, all cracks were extracted completely, as shown in Figure 6.8. Quantitatively, Table 6.1 suggests that proposed algorithm outperforms the other three algorithms, as indicated by the SM values being higher than 90.

6.3.5 Comparative Tests with GRF Images

The tests on the synthetic images and pavement images indicated that the proposed ITV-based crack extraction algorithm can extract all possible sharp curvilinear structures in the presence of severe noise. In comparison with the pavement images, cracks in the GRF images show lower contrast with their surroundings and lower SNRs with a huge amount of noise. In order to evaluate the effectiveness of the proposed

algorithm for these noisy and corrupted GRF images, it was compared with the aforementioned algorithms in this section.

Given the fact of low spectral resolution of the GRF image, the searching radius r in the FoSA algorithm has to be smaller to obtain a consistent window for seed growing. However, the small searching radius r make it difficult to represent the seed-growing path of cracks. Moreover, spectral inconsistency caused by point sampling pattern of MLS data leads to the failure of the FoSA algorithm to adequately extract cracks. This algorithm might work for cracks if relevant pre-processing procedures, such as filtering, are employed.

The comparison of the results of the other three methods is shown in Figure 6.9, and the quantitatively compared results are listed in Table 6.2. Notice that the proposed algorithm maintain a much more stable performance than those of CrackTree and the dynamic programming, since the SM values for the proposed algorithm range from around 94 to 97. In addition, visual inspection shows that the extracted cracks are quite complete. These quantitative and qualitative results demonstrate that the proposed algorithm achieves a stable performance for not only the pavement images but also the noisy GRF images. The dynamic optimization method achieves a poor performance for the complex shaped cracks in the GRF image. Due to the robustness of tensor voting under the conditions of low SNR and low spectral contrast, the tensor voting based CrackTree also outperforms the dynamic programming. However, compared to the CrackTree, the developed algorithm enhances promising, salient curvilinear cracks and suppresses surrounding noise by gradually reducing the voting aperture, following an

145

iterative processing pattern. Thus, the proposed ITV-based crack extraction algorithm can preserve much more details of cracks.
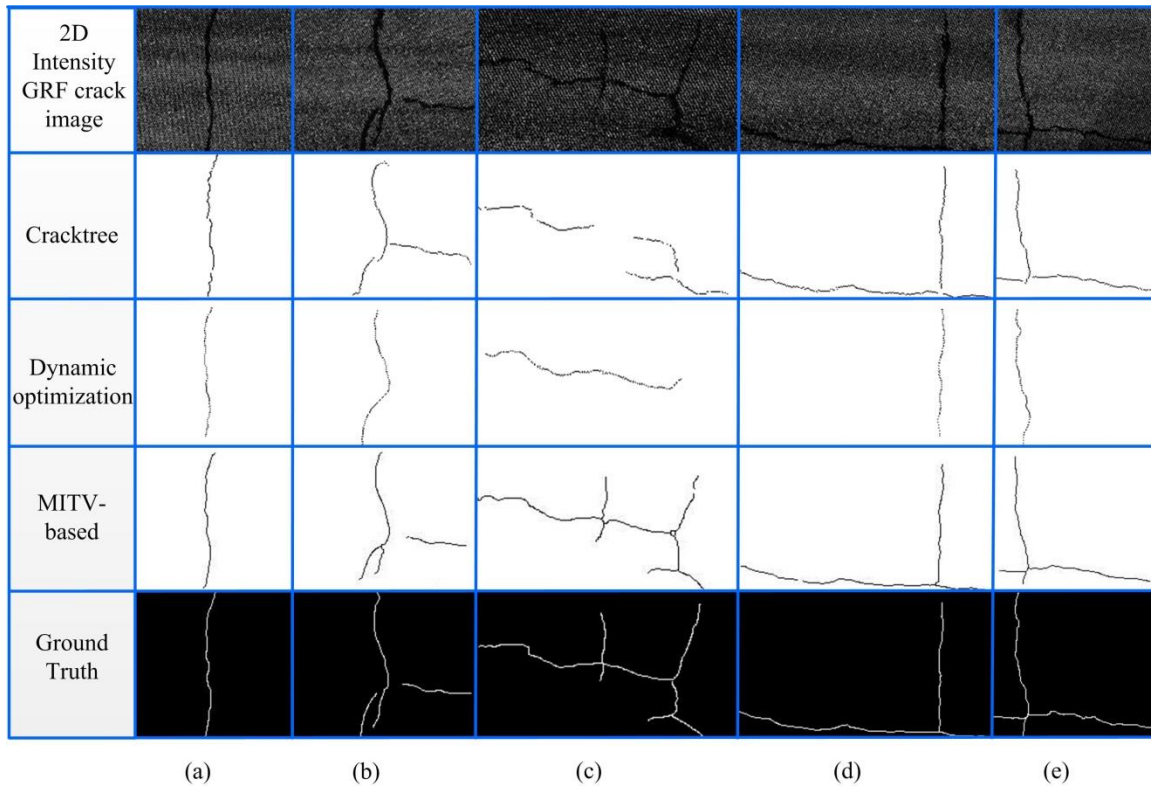

Figure 6. 9: A comparison of the proposed algorithm with the other approaches using GRF images: (a) Crack 1, (b) Crack 2, (c) Crack 3, (d) Crack 4, and (e) Crack 5.

Table 6.2: SM values of the three crack extraction methods for GRF images.

	Crack 1	Crack 2	Crack 3	Crack 4	Crack 5
The proposed ITV-based algorithm	97.32	95.64	94.14	96.64	95.79
CrackTree	92.08	65.15	49.62	94.02	77.37
Dynamic optimization	84.08	51.76	46.60	31.90	43.60

6.3.6 Computational Efficiency

The analysis indicates that the proposed algorithm is capable of enhancing cracks from the noisy and corrupted GRF data because it gradually concentrates on the promising crack curvilinear structures by refining previous results. However, iteration

146

increases computation time. Figure 6.10 shows the runtime for eight cracks, including five GRF images and three pavement images. Observed from Figure 6.10 and Table 6.3, the runtime grows as the number of iterations increases. However, for all cracks, the growth rates of the runtime are slow. The reason is that the proposed algorithm employs a saliency thresholding scheme to delete pixels with low saliency and gradually focuses the votes on only promising curves. It is the first round of dense ball-and-stick voting, ball voting in particular, that occupies the majority of processing time. Compared to the five GRF images, the runtime for the three pavement images is much shorter in spite of their larger sizes. This is because the GRF images contain much more noise than the pavement images, and the proposed ITV-based algorithm takes considerable time to concentrate the promising cracks.

Processing time

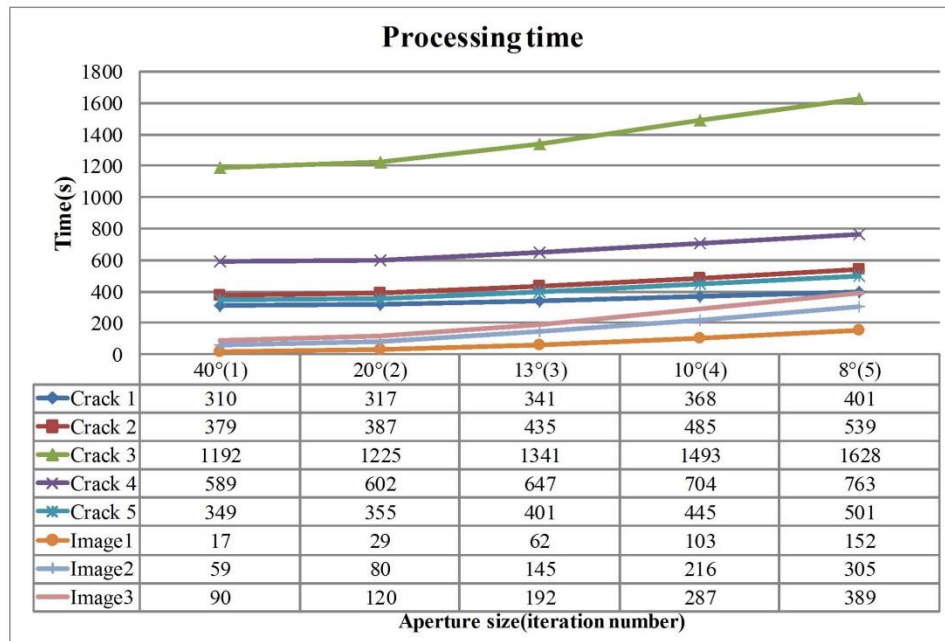|	40°(1)	20°(2)	13°(3)	10°(4)	8°(5)
Crack 1	310	317	341	368	401
Crack 2	379	387	435	485	539
Crack 3	1192	1225	1341	1493	1628
Crack 4	589	602	647	704	763
Crack 5	349	355	401	445	501
Image1	17	29	62	103	152
Image2	59	80	145	216	305
Image3	90	120	192	287	389

Aperture size(iteration number)

Figure 6.10: Processing time for all eight cracks at 5 different iterations.

Table 6.3: Computational efficiency and SM values for all eight cracks at 5 different iterations.
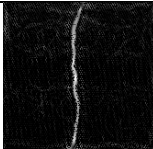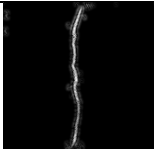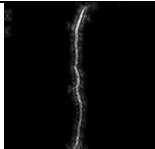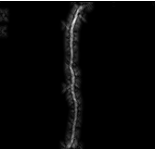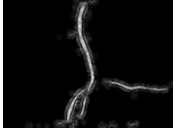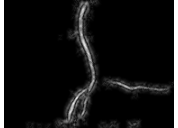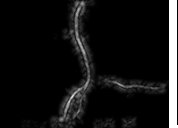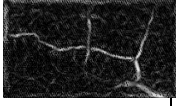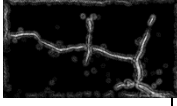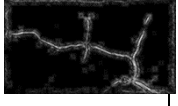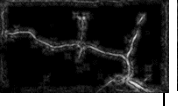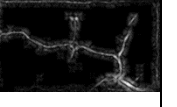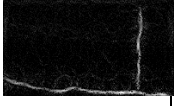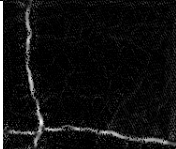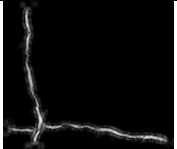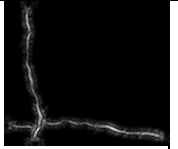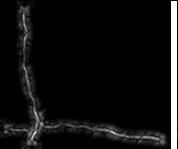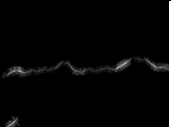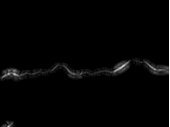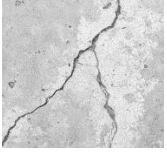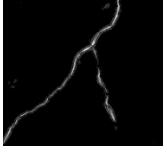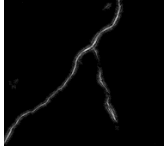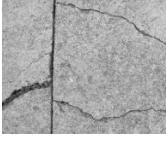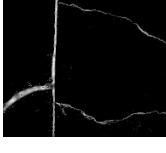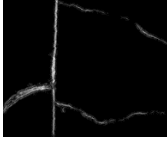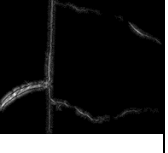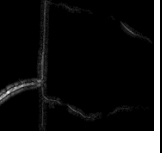
Crack 1	Original data	1	2	3	4	5
	SM	95.99	96.97	95.77	95.55	94.78
	Runtime (s)	310	317	341	368	401
Crack 2						
	SM	90.60	95.15	94.50	94.00	91.59
	Runtime (s)	379	387	435	485	539
Crack 3						
	SM	89.14	94.06	93.38	92.94	90.57
	Runtime (s)	1192	1225	1341	1493	1628
Crack 4						
	SM	93.90	94.62	94.22	94.90	94.73
	Runtime (s)	589	602	647	704	763
Crack 5						
	SM	92.94	95.33	94.71	93.69	90.77
	Runtime (s)	349	355	401	445	501
Image 1						
	SM	92.55	94.69	91.84	88.02	87.93
	Runtime (s)	17	29	62	103	152

Image 2					
SM	92.67	93.72	88.79	87.66	87.72
Runtime (s)	59	80	145	216	305
Image 3					
SM	92.75	94.54	94.41	93.11	92.38
Runtime (s)	90	120	192	287	389

Rather than all pixels, only the crack candidates binarized from the GRF images are the input to be encoded as ball tensors, with the result of the computational cost being reduced by 10%-25% for all five GRF images, yet the values of SM dramatically growing by 5% - 40%, as shown in Figures 6.11 (a) and (b). With little interference from non-crack pixels, the proposed algorithm concentrates on crack candidates, thus improving its performance and stability for crack extraction, as shown by the SM values being around 95. Traditional tensor voting algorithms generally use a dense stick voting process for gradually concentrating on curvilinear structures. However, as we mentioned, a ball tensor contains implicit stick information after ball voting according to eigen-decomposition. Figures 6.12 (a) and (b) show the comparative results between dense stick voting and dense ball-and-stick voting in each iteration. We found that the algorithm using only stick voting dramatically reduced the computational cost by 90%. However, the accuracy of the extracted cracks is unstable as the SM value ranged from 75.93 to 94.50. On the other hand, ball-and-stick voting preserves many subtle curvilinear crack details, entailing a higher degree of accuracy; although it leads to the disadvantage of an increase in computational costs.
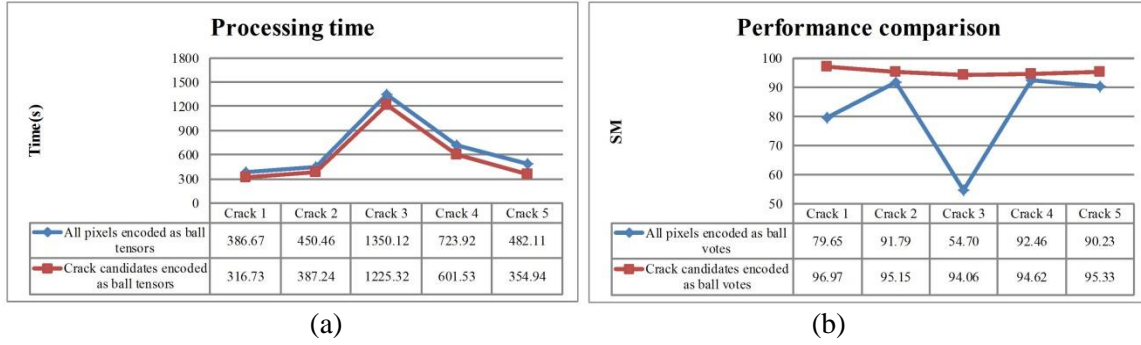
Figure 6.11: Quantitative comparisons between the methods using all pixels and crack candidates encoded as ball tensors: (a) processing time, and (b) SM values.
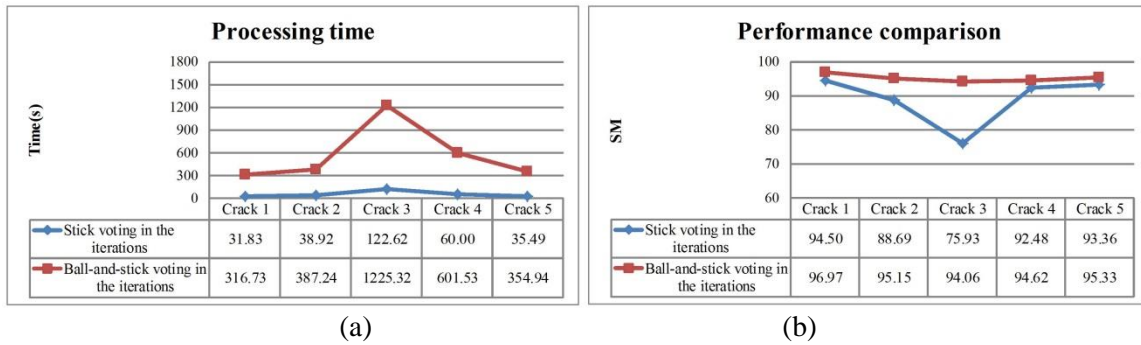
Figure 6.12: Quantitative comparisons between the methods using stick voting alone and ball-and-stick voting, in the iterations: (a) processing time, and (b) SM values.

6.3.7 Overall Tests with a Large MLS Dataset

The performance of the proposed ITV-based algorithm was tested on a road section covered by a number of cracks, as shown in Figure 6.13. The selected road is a two-lane road with a length of 75.4 m and a width of around 8 m (see Figure 6.13 (a)). The number of the road-surface points is 2,547,020. The GRF image resolution is 2 cm, which means that the width of cracks shown in the GRF image is larger than 2 cm, indicating these cracks are desperately needed to be repaired, such as sealing or filling operations. Figures 6.13 (b) and (c) show the extracted cracks, and the extracted cracks overlaid in the GRF image, respectively. As shown in Figure 6.13, almost all cracks with the widths over 2 cm were extracted. In order to accelerate the extraction procedure, the 75-m-long road is segmented into a series of small images with a size of 200×125 pixels.

150
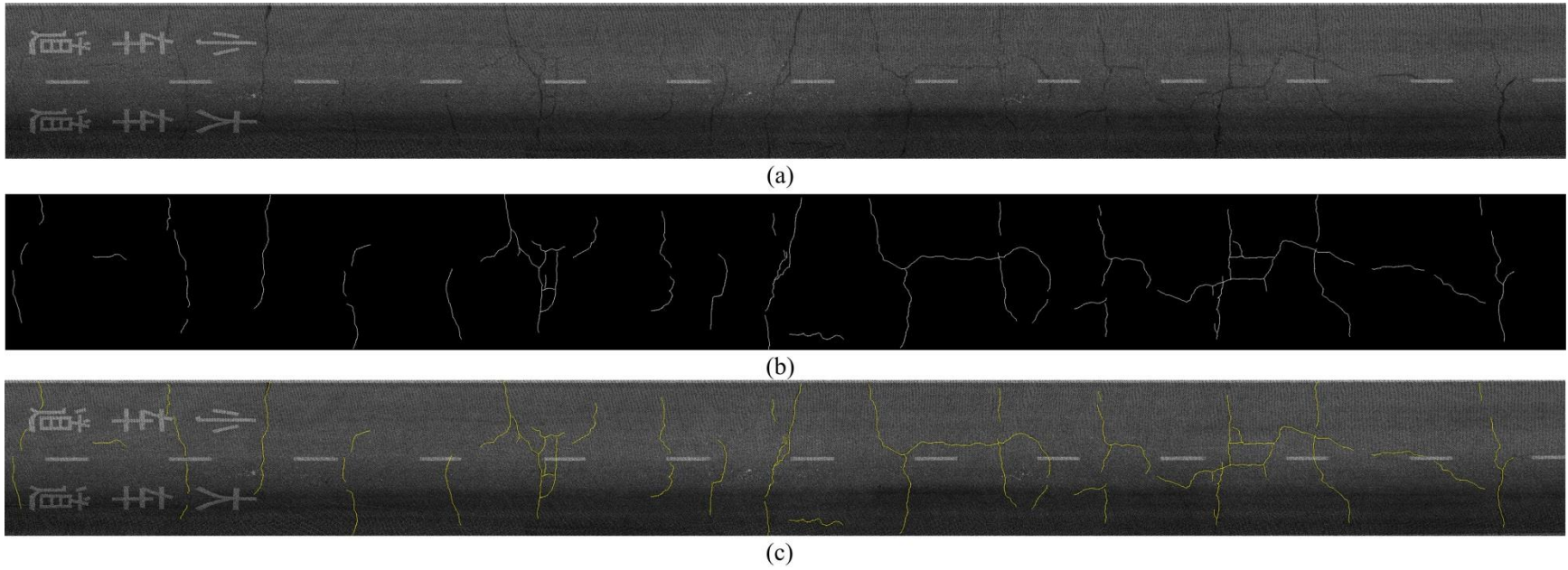
Figure 6.13: Extracted cracks on a 75.4-m-long road surface: (a) GRF image, (b) extracted cracks, and (3) extracted cracks overlaid in the GRF image.

The total processing time for all small images is approximately 5995 seconds, computationally intensive due to the iteration operation involved in the tensor voting process. However, it could be solved in the recent research of distribution computation because the voting process of each tensor is independent. In the parallel environment or a multi-thread scheme, the computation burdens can be distributed to each parallel procedure, indicating that the computational performance will be obviously improved and the time complexity will be greatly reduced. In addition, although the current MLS data resolution limits to the extraction of pavement cracks over 2 cm, the hardware advancement in the foreseeable future will allow cracks at mm-level to be extracted.

6.4 Discussion

This chapter presented an ITV framework for identifying pavement cracks from MLS data. The proposed algorithm is based on the assumption that cracks to be detected in the GRF intensity image are darker than their neighboring non-crack pixels because of the following reasons: (1) the concave-shaped cracks in the visible/near-infrared make non-cracked road pavements brighter, (2) compared to pavement surfaces, deeper layers exposed by cracks contain higher contents of the original asphalt mix, leading to an increase of hydrocarbon absorption features that highlight their contrary spectral signals. However, compared to high-spectral-resolution digital images, the generated GRF image contains a high amount of noise. In addition, curvilinear cracks in the generated GRF image are presented by non-uniform intensity, low contrast with their surroundings, and low SNR owing to particle materials of asphalt concrete-surfaced roads, leading to most existing traditional perceptual grouping algorithms ineffective to crack extraction. Thus, two challenges exist in developing the crack extraction algorithm.

152

The first challenge is to develop a segmentation algorithm that can automatically determine an optimal threshold for extracting crack candidates. The developed WID algorithm can first compute the intensity difference of a pixel with its nearest neighbors to reflect the contrast of this pixel with its neighbors. Afterwards, the method can sum up all the difference measures for each gray level to reflect the entire difference of a gray level in the image. By using weighted scheme, the algorithm for finding the optimal segmentation threshold can avoid the effects of the noise and reflect a general difference measure.

The second challenge is to develop a crack extraction algorithm that can enhance the crack candidates from the noisy background by incorporating perceptual cues of proximity and continuity. The tensor voting was applied to the noisy GRF image. The algorithm starts by encoding every pixel in the image as an unoriented ball tensor. Through the ball tensor voting, all the tensors obtain their preferred orientations, which indicate the potential curvilinear structures. A set of consecutive stick tensor voting procedures is imposed after thresholding out tensors with small saliencies. Each iteration aims at refining the previous one at gradually reduced scales. Thereby, this iterative operation gradually enhances the concentration of the votes over promising, salient curvilinear structures. However, given that cracks in the GRF images show the diffused and heterogeneous curvilinear structures, an iterative tensor voting was adapted to improve crack grouping and reference by enhancing the concentration of the votes over promising curvilinear structures at different scales. The proposed algorithm has two distinctions: (1) Prior to the voting in a sparse basis, crack candidates are segmented and encoded as unit ball tensors. Due to the use of crack candidates rather than all the pixels

153

on the image, the processing complexity is dramatically reduced. (2) Each iteration considers both stick and ball voting, rather than stick voting alone, in a dense voting form for refining salient curvilinear structures by gradually reducing the aperture of the stick voting field. The introduction of the ball voting in the dense voting assists in preserving much subtle curvilinear crack details.

Sseveral large-scale experiments were conducted to evaluate the stability and capability of the ITV-based crack extraction framework. First, the tensor voting was applied to two groups of the synthetic data corrupted by the additive Gaussian white noise and multiplicative gamma noise. The experiment results show that the tensor voting is noise robust and capable of preserving the details of curvilinear structures. The second experiment is the ability of the proposed iterative tensor voting framework to different types of cracks and small cracks with a few centimeters in width extending to large alligator cracks up to the size of 10 cm. The measure scores show that the proposed algorithm can accurately and precisely detect those cracks in the GRF image. A series of experiments were also conducted to test the sensitivity of parameters used in the proposed algorithm. There are five parameters used: σ_1, σ_2, Γ_b, Γ_s, and $\Delta\theta$. Empirical experiments present Γ_b =0.4, Γ_s =0.05 by histogram analysis. Note that the best cracks could be obtained at σ_1 = 9.0 or 10.0, σ_2 = 3.0, and $\Delta\theta = 10°\sim 15°$.

For most MLS systems, digital cameras have become conventional components. Also, digital image-based mobile mapping systems have been widely used for crack extraction. Thus, the proposed crack extraction algorithm was extended to extract cracks from digital images by comparing it with two newly proposed crack extraction methods. The comparative experiments show that the developed algorithm is better than others by

an average measure score over 90. Moreover, the GRF images, much noisy data, were used for algorithm comparison. The experiments suggest that the proposed algorithm is stable for detecting cracks from the noisy intensity data with the average measure score over 94.

6.5 Chapter Summary

This chapter presents an ITV-based crack extraction framework, which is based on tensor voting for curvilinear structure in clutter backgrounds. To detect cracks from the asphalt concrete-surfaced pavements, the proposed framework includes four stages: (a) pre-processing including curb-based road extraction and crack image generation, (b) thresholding segmentation, (c) ITV-based crack enhancement, and (d) morphological thinning.

The performance of the ITV-based crack extraction framework was validated quantitatively and qualitatively by the synthetic data and real crack images. In synthetic data test, the framework achieved SM values of over 97 and 95 for curvilinear structures corrupted with different-variances additive and multiplicative noise, respectively. Experiments on the real cracks in the GRF image, the proposed algorithm is shown to be superior to other crack extraction methods. One limitation is computationally intensive due to the iteration operation involved in the tensor voting process. However, it could be solved in the recent research of distributed computation. In the parallel environment, the efficiency of crack extraction can be improved.

The ITV-based crack extraction method has two contributions. First, the method explores intensity information of MLS data for crack extraction. Current MLS systems capture both high-accurate geometric information and strong reflective information of

155

objects; therefore, it is intuitive to research intensity, as a complementary data feature, for specialist road network asset inventory tools. Another contribution is to extend ITV to solve the problem of crack extraction in a noisy GRF image.

Chapter 7 Conclusions and Recommendations

7.1 Conclusions

MLS is being used at a rapidly increasing rate for many types of transportation-related as-built surveys because of the following advantages: improved safety, efficiency, flexibility, data reusability, data confidence, coverage, and cost saving. One of the biggest strengths of mobile mapping is its ability to capture highly dense datasets, but this also presents one of its biggest challenges. Datasets collected by MLS systems are very large and require extensive network storage space, as well as network and workstation processing capabilities. Point clouds have to be post-processed to provide the deliverables due to no attribute information. Current CAD package or other software packages are incapable of modelling and utilizing point clouds for design. Feature extraction will require new software and high-end workstations.

This dissertation offers a RoadModeler prototype with three computerized algorithms: (1) road-surface extraction, (2) road-marking extraction, and (3) pavement-crack extraction. This doctoral research on RoadModeler using MLS data explores and prototypes a system of extracting road information for all levels of transportation agencies, and opens a window to advanced MLS technologies for road surveying.

A curb-based road-surface extraction algorithm is proposed to extract road surfaces from large volumes of MLS data. The algorithm explores the vehicle trajectory for estimating road curvatures and facilitating data profiling, and extracts road surfaces by detecting curbs from data profiles. The results presented in this dissertation show the proposed algorithm was successfully used on RIEGL VMX-450 data.

Subsequently, a road-marking extraction algorithm and a crack extraction algorithm are proposed, respectively. It is important that the proposed algorithms assume that, on the road surfaces, road markings are painted with highly reflective materials, while pavement cracks are presented as darker curvilinear structures. As a result, the extracted 3D road-surface points are converted into 2D GRF images for the extraction of road markings and pavement cracks. Point density is explored to find the locally optimal thresholds for the segmentation of road markings from unevenly distributed GRF images. Experimental results in this dissertation demonstrate that the proposed algorithm achieves a good performance for many types of road markings and computational efficiency.

As for pavement cracks that present low contrast with their surroundings, low signal-noise-ratio, and a poor continuity caused by intensity inconsistency, the classic tensor voting framework is extended into the iterative tensor voting framework for the detection of curvilinear crack structures. The results presented in this dissertation show that the proposed algorithm is capable of extracting pavement cracks from both the GRF images and digital images.

7.2 Contributions

This dissertation presents four contributions to automated road-information extraction. Namely, the road-surface extraction algorithm, the GRF image generation algorithm, the road-marking extraction algorithm, and the crack extraction algorithm, following is a brief summary of these contributions.

1. **A curb-based road-surface extraction algorithm for the separation of road points from off-road points** of MLS data has been presented. A prior knowledge

of the vehicle trajectory facilitates to partition MLS data into a number of data blocks and profiles. Curbs, vertical surfaces that separate road surfaces from sidewalks, are detected from the partitioned profile data. This algorithm is computationally efficient as the calculation is performed within the pseudo scan-lines generated from a large volume of MLS data via a profiling strategy as discussed in Chapter 4. In addition, this algorithm that detects curbs from a sequence of profile images using slope and elevation difference can be adaptive to the complexity of road surroundings. Furthermore, this algorithm is used in this research as a pre-processing step to provide the road-surface data for road-surface or off-road information extraction.

2. **A 2D GRF image generation algorithm** of MLS data has been presented. The classified road-surface data are interpreted into a 2D raster data, termed as GRF image, in order to further improve computational efficiency. This algorithm combines local and global intensity weights to overcome unevenly distributed intensity data caused by the incidence angle, the scanning range, and the characteristics of target surface.

3. **A road-marking extraction algorithm** of MLS data has been presented. This algorithm applies the point-density attribute of MLS data to the 2D GRF images. The approximate normality of point-density dynamically determines multiple thresholds for segmenting road markings. The morphological closing operation is subsequently employed for incompleteness and noise removal. This algorithm is computationally efficient because all operations are implemented in the 2D GRF image.

4. **An ITV-based crack extraction algorithm** of MLS data has been presented. This algorithm identifies and extracts road pavement distresses, that is, pavement cracks, from the interpreted road-surface data. Similar to the proposed road-marking extraction algorithm, the proposed algorithm extracts pavement cracks from 2D GRF images. Tensor voting, a well-known algorithm for extracting curvilinear structures from noisy and corrupted data, was adapted and applied to the 2D GRF images. The developed algorithm encodes crack candidates rather than all pixels in the GRF images as unit ball tensors to dramatically reduce computational complexity. In addition, this algorithm uses ball-and-stick voting, rather than stick voting alone, in a dense voting form for refining salient curvilinear structures by gradually reducing the aperture of the stick voting field. The dense ball-and-stick tensor voting preserves much subtle curvilinear crack details.

7.3 Recommendations for Future Studies

This doctoral research has made four contributions to the field of mobile mapping technology in the aspects of the automated extraction of road surface, road markings, and pavement cracks, respectively, from the point clouds acquired by the state-of-the-art mobile laser scanning systems. This section discusses the future work that will be directed towards improving each individual components of the RoadModeler prototype, and also towards system-related and conceptual improvements. An interesting challenge will be to integrate more automated algorithms into RoadModeler.

7.3.1 Road-surface Extraction

(1) Considering working principles of MLS

Curbs were detected from each pseudo scan-line generated from each profile with a certain width. Although a certain width of profile data can guarantee adequate points to the presence of curbs, too many points would decrease the accuracy of the extraction of road edges.

Given the MLS scanning principle that a laser scanner is triggered by a high precision timer and rotates at a fixed frequency, points extracted from returned pulses are sequentially recorded using a unique time marker. Thus, the consecutive points could be justified using criteria such as elevation difference and slope.

Point density would be another criterion that justify whether a point belongs to a curb because the curb surface is nearly vertical and contain more points than its neighboring road surface. Multiple rules would be helpful to the extraction of curbs from MLS data.

(2) Automated extraction of road edges using active contour model

In image-based road extraction systems, snakes or active contour models have been widely used to outline road edges from a possibly noisy image because snakes are explicitly presented as a controlled spline curve based on computed energy. The snake framework attempts to minimize the energy associated with the current contour as a sum of an internal and external energy. The internal energy controls the curve's elasticity and rigidity, while the external energy guides the snake toward the boundary of interest.

When the snake energy reaches the minimum, the boundaries of an object such as road could be outlined. The popularity of this method could be attributed to its ability to assist in the estimation of object boundaries with a priori knowledge and user interaction.

The proposed curb-based road-surface extraction algorithm is limited to urban roads with curbs and incapable of extracting road edges of rural roads without curbs. Thus, snakes could be extended to a general road extraction framework. For example, integrating digital images with GRF images could be a promising solution to precise extraction of road edges.

(3) Improving extraction of road surfaces with other ancillary information

The vehicle trajectory records the precise time-stamped geometric information of the vehicle running along the road. Although the vehicle trajectory is applied to the data partition and provide a constraint to the generation of road edges. Further research is needed to explore the applicability of the vehicle trajectory. For example, the vehicle trajectory could be a prior knowledge to be integrated into the active contour model for the automated extraction of road edges.

This thesis first extracts road surface and then identifies road makings on the extracted road surface. An inverse scheme could be used to first identify road markings and extract road surfaces in light of a prior knowledge of road markings. Multiple data sources and relevant road features could not only facilitate road extraction, but also improve the quality of road extraction.

(4) Algorithm extension

The main extension of the proposed algorithm is to develop a GIS-related road inventory asset library that stores road-related information, such as road width, length, roughness, direction, and other geometric attributes.

7.3.2 Road-marking Extraction

(1) Improving intensity quality

Intensity values faded towards the edges of the road are caused by the longer distance from the laser scanner and the larger incidence angle. Calibrated intensity could give added value for laser scanning data processing, for example, in making object recognition and classifying easier and more reliable. Although the road-marking extraction algorithm equalizes intensity using local-and-global information when converting 3D road data into GRF images, unevenly distributed intensity still exists in the GRF image, more or less, decreasing the quality of the extracted road markings. A universal threshold for segmenting road markings is impossible to achieve a good result. In order to solve this problem, the point density was used to section the road surface into a number of bins, perpendicularly to the line of travel. An optimal threshold for each bin was calculated by Otsu's method. With this scheme, road markings were dynamically segmented. However, the segment range determined by the point density could be a little questionable without the constraint of the vehicle trajectory.

Thus, radiometric correction for distorted intensity data is required. The radiometric correction for MLS intensity data in the future research could focus on the

much modifications of the radar range equation. The corrected intensity data can be used in the applications such as feature extraction, segmentation, and classification.

(2) Improving extraction of road markings

The extracted road markings by Otsu's method contain much noise and are incomplete. Noise removal is very critical for road-marking extraction because noise could be enlarged by morphological dilation operation and cannot be removed by morphological erosion operation. The size of the structuring element is behind this. Moreover, the shape of the structuring element is another factor that plays an important role in noise removal and road-marking completeness. Future research is required to investigate the proper structuring elements, or to provide a tool for adaptively selecting structuring elements with different sizes and shapes based on accuracy evaluation.

(3) Accuracy validation

In the task of road-marking extraction, the extracted road-marking results were evaluated by comparing with the manual interpretation using three measures: correctness, completeness, and F- measure. These measures may have a limitation to the evaluation of road markings because of some interpretation errors during converting 3D MLS data into 2D GRF images. Thus, an improved validation is required to examine the accuracy of road-marking extraction.

(4) Algorithm extension

One extension for the developed algorithm is to develop a road-marking model library, a model-based road marking classification system. Our team has developed a

shape-context-based light-pole extraction algorithm which can be modified and employed to extract road markings.

7.3.3 Pavement-crack Extraction

(1) Improving the quality of thresholding

GRF images contain noise and uneven illumination, leading to curvilinear cracks presented by non-uniform intensity, low contrast with their surroundings, and low SNR owing to particle materials of asphalt concrete-surfaced roads. Before the tensor voting framework is implemented for crack extraction, a thresholding algorithm is required to search crack candidates as input. Traditional thresholding methods including Otsu's method somewhat fail to segment crack pixels from the noisy and low-contrast image. Although the proposed WID method achieved a greater performance by computing intensity difference of a pixel with its nearest neighbors to reflect the contrast of this pixel with its neighbors, the segmented cracks are required to improve for noise removal and preserving much crack details.

(2) Improving computational efficiency

The segmented cracks by using the proposed WID method were input to the iterative tensor voting for crack enhancement. In order to remove noise and preserve crack details, the tensor voting framework was used to iteratively refine the previous crack results using an iterative scheme, thereby leading to intensive computation burdens. However, the voting process of each tensor is independent. Therefore, the iterative tensor voting can be carried out using a parallel computation or a multi-thread scheme. The

computation burdens can be distributed to each parallel procedure. The computational performance will be obviously improved and the time complexity will be greatly reduced.

(3) Crack classification

The developed ITV-based crack extraction algorithm can detect multiple types of curvilinear cracks, but crack classification is not included in this thesis. Thus, two tools are required to improve the algorithm: (1) a crack classification tool and (2) a crack attribute report tool. Tensor voting will be extended to detect the intersection points among curvilinear cracks. As a result, intersection points and curvilinear cracks will be grouped to a topology table, in which the algorithm can tell what types of the detected cracks will belong to. Moreover, the algorithm can tell not only the types of cracks, but also provide detailed information of the detected cracks, such as length and width, as a reference for transportation agencies.

(4) Algorithm extension

According to the specification of RIEGL VMX-450, the average interval between points is around 3 cm to 6 cm at the speed of 30 km/h, which means the detect cracks are only at cm-level, rather than mm-level required by most transportation agencies. Although the proposed algorithm has been tested on digital images that record cracks at mm-level, the algorithm is needed to extend for extracting mm-level cracks from MLS data.

7.3.4 Extension of RoadModeler

This doctoral study focused on the extraction of road surfaces, road markings, and pavement cracks, three models of the RoadModeler prototype developed for transportation-related applications. As for the applications in road traffic safety, the RoadModeler package should include the models of not only road-surface related information (e.g., road surfaces, road centre-lines, road markings, manholes, and pavement cracks) but also off-road-related information (e.g., traffic signs, tunnels, light-poles, and trees). The main extension of RoadModeler is to develop models that extract off-road features and other road-related features for the completion of this transportation-related software package.

References

Ayenu-Prah, A. and Attoh-Okine, N., 2008. Evaluating pavement cracks with bidimensional empirical mode decomposition, *EURASIP Journal on Advances in Signal Processing*, vol. 2008, pp. 1-7.

Babic, L., Pribicevic, B., and Dapo, A., 2012. Mobile laser scanning (MLS) in transport infrastructure documentation and research, *Hrčak*, vol. 15, pp. 96-99.

Barber, D., Mills, J., and Smith-Voysey, S., 2008. Geometric validation of a ground-based mobile laser scanning system, *ISPRS Journal of Photogrammetry and Remote Sensing*, vol. 63, pp. 128-141.

Beraldin, J., Blais, F., and Lohr, U., 2010. Laser scanning technology. In: Vosselman, G. and Mass, H. (eds.), *Airborne and Terrestrial Laser Scanning*, pp. 1-42.

Bertozzi, M., Broggi, A., Conte, G., and Fascioli, A., 1997. Obstacle and lane detection on the ARGO autonomous vehicle, *Proceedings of IEEE Conference on Intelligent Transportation Systems (ITSC'97)*, Boston, MA, U.S.A., 09-12 November 1997, pp. 1010-1015.

Boyko, A. and Funkhouser, T., 2011. Extracting roads from dense point clouds in large scale urban environment, *ISPRS Journal of Photogrammetry and Remote Sensing*, vol. 66, no. 6, pp. S2-S12.

Bray, J., Verma, B., Li, X., and He, W., 2006. A neural network based technique for automatic classification of road cracks, *Proceedings of the International Joint Conference on Neural Networks (IJCNN06)*, Vancouver, BC, Canada, 16-21 July 2006, pp. 907-912.

Bruton, A. M., 2000. Improving the accuracy and resolution of SINS/DGPS airborne gravimetry, Ph.D. Thesis, University of Calgary, UCGE Report #20145.

Canny, J., 1986. A computational approach to edge detection, *IEEE Transactions on Pattern Analysis and Machine Intelligence*, vol. 8, no. 6, pp. 679-698.

Carnaby, B., 2005. Poor road markings contribute to crash rates, *2005 Australasian Road Safety Research, Policing, and Education Conference*, Wellington, New Zealand, 14-16 November 2005, (CD-ROM, CD401).

Charbonnier, P., Diebolt, F., Guillard Y., and Peyret, F., 1997. Road markings recognition using image processing, *Proceedings of IEEE Conference on Intelligent Transportation Systems (ITSC'97)*, Boston, MA, USA. 09-12 November 1997, pp. 912-917.

Chehata, N., Guo, L., and Mallet, C., 2009. Airborne LiDAR feature selection for urban classification using random forest, In: Bretar F., Deseilligny M., and Vosselman, G. (eds.), Laser Scanning 2009, *ISPRS Archives*, vol. 36 (Part 3/W8), Paris, France, 1-2 September 2009.

Chen, X., Stroila, M., and Wang, R., 2009. Next generation map marking: geo-referenced ground-level LiDAR point clouds for automatic retro-reflective road feature extraction, *17th ACM SIGSPATIAL International Conference on Advances in Geographic Information System*, Seattle, WA, U.S.A., 4-6 November 2009.

Cheng, H., Chen, J., Glazier, C., and Hu, Y., 1999. Novel approach to pavement cracking detection based on fuzzy set theory, *Journal of Computing in Civil Engineering*, vol. 13, no. 4, pp. 270-280.

Clode, S., Rottensteiner, F., Kootsookos, P., and Zelniker, E., 2007. Detection and vectorization of roads from LiDAR data, *Photogrammetric Engineering & Remote Sensing*, vol. 73, no. 5, pp. 517-535.

Cuhadar, A., Shalaby, K., and Tasdoken, S. 2002. Automatic segmentation of pavement condition data using wavelet transform, *Proceedings of IEEE Canadian Conference on Electrical and Computer Engineering*, New York, U.S.A., 28 April -2 May 2002, vol. 2, pp. 1009-1014.

Dal Poz, A. P. and Do Vale, G. M. 2003. Dynamic programming approach for semi-automated road extraction from medium- and high-resolution images, *ISPRS Archives*, vol. 34 (Part 3/W8), pp. 87-91.

Danescu, R. and Nedevschi, S., 2010. Detection and classification of painted road objects for intersection assistance applications, *Proceedings of IEEE Conference on Intelligent Transportation System*, Funchal, Portugal, 19-22 September 2010, pp. 433-438.

Darmawati, A. T., 2008. Utilization of multiple echo information for classification of airborne laser scanning data, Master's Thesis, ITC, Enschede, Netherlands.

Dickmanns, E., and Mysliwetz, B., 1992. Recursive 3D road and relative ego-state recognition, *IEEE Transactions on Pattern Analysis and Machine Intelligence*, vol. 14, no. 2, pp. 199-213.

Dinh, T. N., Park, J., and Lee, G.S., 2010. Voting based text line segmentation in handwritten document images, *10th IEEE International Conference on Computer and Information Technology (CIT 2010)*, Bradford, UK, 29 June - 1 July 2010, pp. 529- 535.

Dougherty E. and Lotufo, R., 2011. *Hands-on Morphological Image Processing*, Bellingham, Wash, U.S.A., SPIE Publications.

Gavilán, M., Balcones, D., Marcos, O., Llorca, D. F., and Sotelo, M. A., 2011. Adaptive road crack detection system by pavement classification, *Sensors*, vol. 11, pp. 9628-9657.

GIM, 2013. Mobile LiDAR mapping focus for international LiDAR mapping forum, http://www.gim-international.com/news/id4330.html, Data accessed: 17 Nov 2013.

Glennie, C., 2007. Rigorous 3D error analysis of kinematic scanning LiDAR systems, *Journal of Applied Geodesy*, vol. 1, pp. 147–157.

Glennie, C., Brooks, B., Ericksen , T., Hauser, D., Hudnut, K., Foster, J., and Avery, J., 2013. Compact multipurpose mobile laser scanning system-initial tests and results, *Remote Sensing*, vol. 5, pp. 521-538.

Gordon P., 2010. 3D scanning: high-definition mobile mapping, *Professional Surveyor Magazine*, Data accessed: August 1, 2013.

Gruen, A. and H. Li, 1997. Semi-automatic linear feature extraction by dynamic programming and LSB-Sankes, *Photogrammetric Engineering & Remote Sensing*, vol. 63, no. 8, pp. 985-995.

Guan, H., Li, J., Yu, Y., and Wang, C. 2013. Geometric validation of a mobile laser scanning system for urban applications, *MMT 2013*, Taiwan, China, 1-3 May 2013.

Guy, G. and Medioni, G., 1996. Inferring global perceptual contours from local features, *International Journal of Computer Vision*, vol. 20, no. 1-2, pp. 113-133.

Guy, G. and Medioni, G., 1997. Inference of surfaces, 3D curves, and junctions from sparse, noisy, 3D data, *IEEE Transactions on Pattern Analysis and Machine Intelligence*, vol. 19, no. 11, pp. 1265-1277.

Haala, N., Peter, M., Cefalu, A. and Kremer, J., 2008. Mobile LiDAR mapping for urban data capture, In: Loannides, M., Addison, A., Georgopoulos, A., and Kalisperis, L. (eds.), *14th International Conference on Virtual Systems and Multimedia*, pp. 95-100.

Hawwar, Y. and Reza, A., 2002. Partially adaptive multiplicative noise image denoising technique, *IEEE Transactions on Image Processing*, vol. 11, no. 12, pp. 1397-1404.

Huang, Y. and Tsai, J., 2011. Enhanced pavement distress segmentation algorithm using dynamic programming and connected component analysis, *Journal of the Transportation Research Record*, vol. 2225, pp. 89-98.

Huttenlocher, D. P., Klanderman, G. A., and Rucklidge, W. J., 1993. Comparing images using the hausdorff distance, *IEEE Transactions on Pattern Analysis and Machine Intelligence*, vol. 15, no. 9, pp. 850-863.

Hutton, J., 2008. Aerial perspective: paradigm shift in mobile mapping technology, *Professional Surveyor Magazine*, Data accessed: August 1, 2013.

Iavarone, A., 2007. Feature: terrestrial LiDAR goes mobile, *Professional Surveyor Magazine*, Data accessed: August 1, 2013.

Jaakkola, A., Hyyppä, J., Hyyppä, H., and Kukko, A., 2008. Retrieval algorithms for road surface modelling using laser-based mobile mapping, *Sensors*, vol. 8, pp. 5238-5249.

Jacobs G., 2005. Uses in transportation in high-definition surveying: 3D laser scanning, *Professional Surveyor Magazine*, vol. April.

Jang, B. K. and Chin, R. T., 1990. Analysis of thinning algorithms using mathematical morphology, *IEEE Transactions on Pattern Analysis Machine Intelligent*, vol. 12, pp. 541-551.

Kaul, V., Tsai, J., and Mersereau, R., 2008. A quantitative performance evaluation of pavement distress segmentation methods, G*eorgia Tech Technical Report*, Georgia Institute of Technology, Atlanta, 2008.

Kheyrollahi, A. and Breckon, T. P., 2010. Automatic real-time road marking recognition using a feature approach. *Machine Vision and Applications*, vol. 23, no. 1, pp. 123-133.

Kim, T., Seung-Ran Park, Moon-Gyu Kim, SooJeong, and Kyung-Ok Kim, 2004. Tracking road centerlines from high resolution remote sensing images by least squares correlation matching, *Photogrammetric Engineering & Remote Sensing*, vol. 70, no. 12, pp. 1417-1422.

Kittler, J. and IUingworth, J., 1986. Minimum error thresholding, *Pattern Recognition*, vol. 19, no. 1, pp. 41-47.

Koutsopoulos, H. N., El Sanhouri, I., and Downey, A. B., 1993. Analysis of segmentation algorithms for pavement distress images, *Journal of Transportation Engineering*, vol. 119, no. 6, pp. 868-888.

Kukko, A., Karritine, H., Hyyppa, J., and Chen, Y., 2012. Multiplatform mobile laser scanning: usability and performance, *Sensors*, vol. 12, pp. 11712-11733.

Kumar P., McCarthy, T., and McElhinney, C., 2010. Automated road extraction from terrestrial based mobile laser scanning system using the GVF snake model, *Proceedings of the European LiDAR Mapping Forum (ELMF 2010),* Hague, Netherlands, 30 November-1 December 2010.

Langley, R. B., 1999. Dilution of precision, *GPS World*, vol. 10, no. 5, pp. 52-59.

Lee, H., 1992. Standardization of distress measurements for the network-level pavement management system, pavement management implementation, *ASTM STP 1121*, In: Frank B. Holt and Wade L. Gramling (eds.), American Society for Testing and Materials, Philadephia, pp. 424-436.

Lemmens, M., 2011. Geo-information: Technology, Applications and the Environment, *Geotechnologies and the Environment Series*, Springer, vol. 5, pp. 101-121.

LiDAR News, 2013, StreetMapper cuts cost of highway surveying projects by 50 per cent, Data accessed: August 1, 2013.

Li, Q., Zou, Q., Zhang, D., and Mao, Q., 2011. FoSA: F* seed-growing approach for crack-line detection from pavement images, *Image and Vision Computing*, vol. 29, pp. 861-872.

Li, Y., He, K., and Jia, P., 2007. Road markers recognition based on shape information, *IEEE International Symposium on Intelligent Vehicles*, Istanbul, Turkey, 13-15 June 2007, pp. 117-122.

Li, B., Li, Q., Shi, W., and Wu, F., 2004, Feature extraction and modeling of urban building from vehicle-borne laser scanning data, *ISPRS Archives*, Istanbul, Turkey, 12–23 July 2004, pp. 934-940.

Lim, S., Thatcher, C. A., Brock, J. C., Kimbrow, D. R., Danielson, J. J., and Reynolds, B. J., 2013, Accuracy assessment of a mobile terrestrial LiDAR survey at Padre Island National Seashore, *International Journal of Remote Sensing*, vol. 34, no. 18, pp. 6355-6366.

Lichti, D.D., 2010, Terrestrial laser scanner self-calibration: correlation sources and their mitigation, *ISPRS Journal of Photogrammetric and Remote Sensing*, vol. 65, pp. 93–102.

Liu Z., Wang, J., and Liu, D., 2013. A new curb detection method for unmanned ground vehicles using 2d sequential laser data, *Sensors*, vol. 13, pp. 1102-1120.

Loss, L. A., Bebis, G., and Parvin, B., 2011. Iterative tensor voting for perceptual grouping of ill-defined curvilinear structures, *IEEE Transactions on Medical Imaging*, vol. 30, no. 8, pp. 1503-1513.

Lowe, D. G., 1985. *Perceptual Organization and Visual Recognition*, Kluwer Academic Publishers.

Mallat, S. and Zhong, S. 1992. Characterization of signals from multiscale edges, *IEEE Transactions on Pattern Analysis and Machine Intelligence*, vol. 14, no. 7, pp. 710-732.

Manandhar, D. and Shibasaki, R., 2001, Vehicle-borne laser mapping system (VLMS) for 3D GIS, *IEEE Geoscience and Remote Sensing Symposium*, vol. 5, pp. 2073–2075.

Martin, H., 2008. Spectral characteristics of asphalt road surfaces, In: Q. Weng (ed.), *Remote Sensing of Impervious Surfaces*, pp. 237-247.

Medioni, G., Lee, M.-S., and Tang, C.-K., 2000. *A Computational Framework for Segmentation and Grouping*, Elsevier Science Inc.

McCall, J. C. and Trivedi, M. M., 2006. Video based lane estimation and tracking for driver assistance: survey, system, and evaluation, *IEEE Transactions on Intelligent Transportation Systems*, vol. 7, no. 1, pp. 20-37.

Mena, J. B. 2003. State of the art on automatic method for road extraction for GIS update: a novel classification, *Pattern Recognition Letters*, vol. 24, pp. 3037-3058.

McCarthy, T., Fotheringham, A. S., Charlton, M., Winstanley, A., and O'Malley, V., 2007. Integration of LiDAR and stereoscopic imagery for route corridor surveying, *The 5th International Symposium on Mobile Mapping Technology (MMT'07)*, Padua, Italy, 28-31 May 2007.

McGhee, K. H., 2004. Automated pavement distress collection techniques: A synthesis of highway practice, *National Cooperative Highway Research Program (NCHRP) Synthesis 334*, Washington, DC, 2004.

MTO, 1989a. *Manual for condition rating of surface-treated pavements*, SP-021, Distress Manifestations, published by the Research and Development Branch, Ministry of Transportation of Ontario, Canada.

MTO, 1989b. *Flexible pavement condition rating - guidelines for municipalities*, SP-022 Research and Development Branch, Ministry of Transportation of Ontario, August 1989.

MTO, 1989c. *Manual for condition rating of flexible pavements*, SP-024, Distress Manifestations, Research and Development Branch, Ministry of Transportation of Ontario, Canada.

MTO, 1995. *Manual for condition rating of rigid pavements*, SP-026 Concrete Surfaces and Composite Distress Manifestations, Research and Development Branch, Ministry of Transportation of Ontario, Canada.

MTO, 2008. *Improving Network Level Pavement Management through Rationalization and Utilization of Automated/Semi-Automated Technologies*. Highway Infrastructure Innovation Funding Program 2007, Ministry of Transportation Ontario, Downsview, Ontario, Canada.

Nguyen, T., Begot, S., Duculty, F., and Avila, M., 2011. Free-Form anisotropy: a new method for crack detection on pavement surface images, *18th IEEE International Conference on Image Processing (ICIP 2011)*, Brussels, Belgium, 11-14 September 2011, pp. 1069-1072.

Oliveira, H. and Correia, P.L., 2008. Identifying and retrieving distress images from road pavement surveys, *Proceedings of International Conference on Image Processing (ICIP'08)*, San Diego, California, U.S.A., 12-15 October 2008, pp. 57-60.

Otsu, N., 1979. A threshold selection method from gray-level histogram, *IEEE Transactions on Systems, Man, and Cybernetics*, vol. 9, no. 1, pp. 62-66.

Park, M. K., Lee, S. J., and Lee, K. H., 2012. Multi-scale tensor voting for feature extraction from unstructured point clouds, *Graphical Models*, vol. 74, no. 4, pp. 197-208.

Parvin, B., Yang, Q., Han, J., Chang, H., Rydberg, B., and BarcellosHoff, M. H., 2007. Iterative voting for inference of structural saliency and characterization of subcellular events, *IEEE Transactions on Image Processing*, vol. 16, no. 3, pp. 615–623.

Peng, T., Jermyn, I., Prinet, V., and Zerubia, J., 2010. Extended phase field higher-order active contour modelsfor networks: its application to road network extraction from VHR satellite images, *Journal of Computer Vision*, vol. 88, no. 1, pp. 111-128.

Petrie, G. and Toth, C., 2008. Introduction to laser ranging, profiling, and scanning, In: J. Shan and C. K. Toth (eds.), T*opographic Laser Ranging And Scanning: Principles and Processing*, CRC Press, Taylor & Francis, pp. 1-27.

Petri, G., 2010. Mobile mapping systems: an introduction to the technology, *GeoInformatics*, vol. 13, no. 1, pp. 32-43.

Pomerleau, D. and Jochem, T., 1996. Rapidly adapting machine vision for automated vehicle steering, *IEEE Expert*, vol. 11 , pp. 19-27.

Pu, S., Rutzinger, M., Vosselman, G., and Elberink, S. O., 2011. Recognizing basic structure from mobile laser scanning data for road inventory studies, *ISPRS Journal of Photogrametry and Remote Sensing*, vol. 66, pp. s28-s39.

Puente, I., Gonz ález-Jorge, H., Mart ínez-S ánchez, J., and Arias, P., 2013. Review of mobile mapping and surveying technologies, *Measurement*, vol. 46, pp. 2127-2145.

Rebut, J., Bensrhair, A., and Toulminet, G., 2004. Image segmentation and pattern recognition for road marking analysis, *IEEE International Symposium Industrial Electronics*, vol. 1, no. 4-7, pp. 727-732.

Rieger, P., Studnicka, N., Pfennigbauer, M., and Zach, G., 2010. Boresight alignment method for mobile laser scanning systems, *Journal of Applied Geodesy*, vol. 4, no. 1, pp. 13-21.

Road Talk, 2013. A new tool for engineering surveys mobile terrestrial LiDAR scanning (MTLS), *Ontario's Transportation Technology Transfer Digest*, Ministry of Transportation.

Rybka, R., 2011. Autodesk and Bentley systems talk about mobile LiDAR, *LiDAR*, vol. 1, no. 2, pp. 41-44.

Saar, T. and Talvik, O., 2010. Automatic asphalt pavement crack detection and classification using neural networks, *Proceedings of the 12th Biennial Baltic Electronics Conference (BEC10)*, Tallinn, Estonia, 4-6 October 2010.

Schrock, G., 2013. Accessible mobile mapping, *Professional Surveyor Magazine*, Data accessed: August 1, 2013.

Schwarz, K.P. and El-Sheimy, N., 2007. Digital mobile mapping systems - state-of-the-art and future trends, In: V. Tao and J. Li (eds.), *Advances in Mobile Mapping Technology*, Taylor & Francis, pp. 3-18.

Shu, Z. and Guo, Y., 2010. Algorithm on contourlet domain in detection of road cracks for pavement images, *Proceedings of the 9ᵗʰ International Symposium on Distributed Computing and Applications to Business, Engineering and Science*, Hong Kong, 10-12 August 2010.

Smadja, L., Ninot, J., and Gavrilovic, T., 2010. Road extraction and environment interpretation from LiDAR sensors. *ISPRS Archives*, vol. 38, pp. 281–286.

Stauth, D. and Olsen, M., 2013. Mobile LiDAR technology expanding rapidly, http://oregonstate.edu/ua/ncs/archives/2013/mar/mobile-lidar-technology-expanding-rapidly, Data accessed: August 23, 2013.

Subirats, P., Dumoulin, J., Legeay, V., and Barba, D., 2006. Automation of pavement surface crack detection using the continuous wavelet transform, *Proceedings of International Conference on Image Processing (ICIP'06)*, pp. 3037-3040.

Takashi, O. and Kiyokazu, T., 2006. Lane recognition using on-vehicle LiDAR, *IEEE Intelligent Vehicles Symposium*, Tokyo, Japan, 13-15 June 2006, pp. 540-545.

Tanaka, N., 1998. A crack detection method in road surface image using morphology, *Proceedings of IAPR Workshop on Machine Vision Applications (MVA'98)*, Chiba, Japan, 17-19 November 1998.

Tao, V. and Li, J., 2007. *Advances in Mobile Mapping Technology*, Taylor & Francis, London.

Tang, C. K. and Medioni, G., 1998. Inference of integrated surface, curve, and junction descriptions from sparse 3D data, *IEEE Transactions on Pattern Analysis and Machine Intelligence*, vol. 20, no. 11, pp. 1206-1223.

Tang, C.K. and Medioni, G., 2002. Curvature-augmented tensor voting for shape inference from noisy 3D data, *IEEE Transactions on Pattern Analysis and Machine Intelligence*, vol. 24, no. 6, pp. 858-864.

Tong, W. and Tang, C., 2005. Robust estimation of adaptive tensors of curvature by tensor voting, *IEEE Transactions on Pattern Analysis and Machine Intelligence*, vol. 27, no. 3, pp. 434-449.

Toth, C., Paska, E., and Brzezinska, D., 2008. Using road pavement markings as good control for LiDAR data, *ISPRS Archives*, vol. 37 (B1), pp. 189-196.

Toth, C. K., 2009. R&D of mobile LiDAR mapping and future trends, *Baltimore*, Maryland, U.S.A., 9-13 March 2009.

Tsai, Y., Kaul, V., and Mersereau, R. M., 2010. Critical assessment of pavement distress segmentation methods, *Journal of Transportation Engineering*, pp. 11-19.

Tsogas, M., Floudas, N., Lytrivis, P., Amditis, A., and Polychronopoulos, A., 2011. Combined lane and road attributes extraction by fusing data from digital map, laser scanner and camera. *Information Fusion*, vol. 12, pp. 28-36.

Ussyshkin, V., 2009. Mobile laser scanning technology for surveying application: from data collection to end-products, *FIG Working Week 2009-Surveyors Key Role in Accelerated Development*, Eilat, Israel, 3-8 May 2009.

Vosselman, G., 2009. Advanced point cloud processing, *Photogrammetric Week'09*, Heidelberg, Germany, 7-11 September 2009, pp. 137-146.

Vosselman, G. and Knecht, J.D., 1995. Road tracing by profile matching and kalman filtering, *Automatic Extraction of Man-Made Objects from Aerial and Space Images*, Birkhäuser, Basel, pp. 255-264.

Wang, N., Liu, W., Zhang, C., Yuan, H., and Liu, J., 2009. The detection and recognition of arrow markings recognition based on monocular vision, *Chinese Control and Decision Conference*, Guilin, China, 17-19 June 2009, pp. 4380-4386.

Wei, N., Zhao, X., Dou, X. Y., Song, H., and Wang, T., 2010. Beamlet transform based pavement image crack detection, *Proceedings of the International Conference on Intelligent Computation Technology and Automation (ICICTA10)*, Changsha, China, 11-12 May 2010.

Yang, B., Fang, L., Li, Q., and Li, J., 2012. Automated extraction of road markings from mobile LiDAR point clouds, *Photogrammetric Engineering & Remote Sensing*, vol. 78, no. 4, pp.331-338.

Yang B., Fang, L., and Li, J., 2013. Semi-automated extraction and delineation of 3D roads of street scene from mobile laser scanning point clouds, *ISPRS Journal of Photogrammetry and Remote Sensing*, vol. 79, pp. 80-93.

Yen, K. S., Ravani, B., and Lasky, T. A., 2011. LiDAR for data efficiency, *Washington State Department of Transportation (Online article)*, http://www.wsdot.wa.gov/research/reports/fullreports/778.1.pdf.

Ying, L. and Salari E., 2009. Beamlet transform based technique for pavement image processing and classification, *Proceedings of the International Conference on Electro/Information Technology (EIT09)*, Windsor, ON, Canada, 7-9 June 2009.

Yoshida, H. and Tanaka, N. 2009. A binarization method for crack detection in a road surface image with the fractal dimension, *Proceedings of IAPR Conference on Machine Vision Applications (MVA'09)*, Yokohama, Japan, 20-22 May 2009.

Yu, S., Sukumar, S. R., Koschan, A. F., Page, D. L., and Abidi, M. A., 2007. 3D reconstruction of road surfaces using an integrated multi-sensory approach. *Optics and Lasers in Engineering*, vol. 45, pp. 808-818.

Yuan, X., Zhao, C., and Zhang, H., Road detection and corner extraction using high definition LiDAR, *Information Technology Journal*, vol. 9, pp. 1022-1030.

Zarchan, P. and Musoff, H., 2009. *Fundamentals of Kalman Filtering: A Practical Approach*, third ed., American Institute of Aeronautics & Astronautics (AIAA), Reston, VA, pp. 854.

Zhang, W., 2010. LiDAR-based road and road-edge detection, *Proceedings of the IEEE Intelligent Vehicles Symposium*, San Diego, CA, U.S.A., 21–24 June 2010, pp. 845-848.

Zhao, H. and Shibasaki, R., 2002. Surface modelling of urban 3D objects from vehicle-borne laser range data, *ISPRS Archives*, vol. 34 (Part 3/WG III/7).

Zhou, L. and Vosselman, G., 2012. Mapping curbstones in airborne and mobile laser scanning data, *International Journal of Applied Earth Observation and Geoinformation*, vol. 18, pp. 293-304.

Zhou, J., Huang, P. S., and Chiang, F. P. 2006. Wavelet-based pavement distress detection and evaluation, *Optical Engineering*, vol. 45, no. 2, pp. 027007–027010.

Zou, Q., Cao, Y., Li, Q., Mao, Q., and Wang, S., 2012. CrackTree: automatic crack detection from pavement images, *Pattern Recognition Letters*, vol. 33, pp. 227-238.

Appendix A MTO Marking Standards

In order to invest in the future of Canada's Transportation Infrastructure, different levels of Canadian authorities have attempted to seek academic assistances in a number of areas including engineering materials, traffic operations, intelligent transportation systems, highway design, environmental, structures, geomatics, construction, and maintenance; for example, the Highway Infrastructure Innovation Funding Program (HIIFP) funded by MTO. In addition, a variety of road safety strategies such as road safety inspection, road traffic safety, and intelligent transportation systems, have been proposed to identify the elements of roads and monitor pavement performance for quantitatively evaluating road safety along federal, provincial, or municipal corridor routes.

Pavement Cracks

Pavement surface condition data is a key component of the MTO infrastructure asset management program. The crack information is used across a wide range of business processes, which include (1) monitoring the on-going performance of the provincial paved road work, (2) predicting future pavement conditions and assess long term needs, (3) planning strategic investment for the support of annual programming and decision making, (4) identifying rehabilitation and maintenance treatment options, (5) investigating causes of pavement deterioration and evaluating specific treatment options, and (6) supporting outsourced rehabilitation and maintenance service delivery. Usually, regular inspection of all paved road surfaces is carried out to ensure that all areas of pavement failures have been promptly identified, signed and repaired.

MTO performs pavement distress data surveys of their network using four different condition rating manuals for evaluating road surface condition (MTO 1989a, 1989b, 1989c, and 1995). 2012 pavement surface condition rating manual states that there are two practices: (1) high speed network level (HSNL) surveys that are conducted on a cyclical basis for the provincial road network, and (2) project level manual (PLM) surveys that are routinely conducted during the detailed evaluations that are carried out for candidate rehabilitation projects.

The HSNL surveys measure (1) the severity and density of several surface distress types within each surveyed lane, (2) rut depth and roughness measurements in both wheel paths, and (3) digital images of the right-of-way. The HSNL surveys detect the following distress types: longitudinal wheel path cracking, longitudinal joint cracking, pavement edge cracking, transverse cracking, meandering longitudinal cracking, alligator cracking, bleeding, and potholes. The HSNL surveys are conducted every two years on the primary highway system, on a two or four year cycle for secondary highways depending on significance, and on a four year cycle for selected paved side roads (MTO, 2008).

In addition to distress surveys, the PLM surveys can include geotechnical investigations, strength testing, coring, and laboratory testing. The purpose of the PLM surveys is to provide a more accurate and detailed investigation of the pavement deterioration in order to assist in determining appropriate rehabilitation treatments.

Road Markings

Road markings, painted on the road surfaces with high-reflectivity materials deteriorate over time because these road markings are susceptible to damage from snow

plows, winter sand, and traffic. Thus, periodically managing and maintaining road markings is often required to ensure that they are clearly visible at night.

As the retro-reflectivity of road markings is an essential performance indicator for ensuring that drivers can effectively see and respond to changing roadway geometry, particularly, for how they will perform at night or in wet weather. Thus, the minimum acceptable pavement marking retro-reflectivity performance levels were specified.

MTO conducts and monitors the retro-reflectivity of pavement markings by first visually assessing the retro-reflective performance of road markings and identifying areas of concern at night, and a handheld retro-reflectometer is used to measure the road marking retro-reflectivity for these areas of concern during the day.

Appendix B List of Publications during PhD Thesis Work

Refereed Journal Papers

- **Guan, H.,** Li, J., Yu, Y., Chapman, M., and Wang, C., 2014. Automatic road-feature extraction for road traffic safety using mobile laser scanning data. *IEEE Transactions on Intelligent Transportation Systems* (2012 Impact Factor: 3.064, under the 2nd round review).

- **Guan, H.,** Li, J., Yu, Y., Chapman, M., and Yu, J., 2014. Interactive tensor voting method for crack detection using mobile laser scanning data. *IEEE Transactions on Geoscience & Remote Sensing* (2012 Impact Factor: 3.467, under 3rd round review).

- **Guan, H.,** Li, J., Yu, Y., Wang, C., Chapman, M., and Yang, B. 2014. Using mobile laser scanning data for automated extraction of road markings. *ISPRS Journal of Photogrammetry & Remote Sensing*, 87:93-107 (2012 Impact Factor: 3.313).

- Yu, Y., Li, J., Yu, J., **Guan, H.,** and Wang, C., 2014. Pairwise 3D shape context for partial object matching and retrieval on mobile laser scanning data, *IEEE Geoscience and Remote Sensing Letters*, 11(5): 1019-1023 (2012 Impact Factor: 1.823).

- Yu, Y., Li, J., **Guan**, H., and Wang, C., 2014. Automated detection of road manhole and sewer well covers from mobile LiDAR point clouds, *IEEE Geoscience and Remote Sensing Letters*, doi.10.1109/LGRS.2014.2301195 (2012 Impact Factor: 1.823).

- **Guan, H.,** Li, J., Yu, Y., and Zhong, L., 2014. Generating digital terrain models in wooded mountain areas from airborne lidar point clouds by a cross-section plane approach, *International Journal of Remote Sensing*, 35(3):27-948 (2012 Impact

Factor: 1.138).

- Yu, Y., Li, J., **Guan, H.,** and Wang, C., 2013. A marked point process for automated building detection from LiDAR point-clouds, *Remote Sensing Letters*, 4(11):1127-1136 (2012 Impact Factor: 1.615).

- **Guan**, **H.,** Li, J., Zhong, L., Yu, Y., and Chapman, M., 2013. Process virtualization of large-scale lidar data in a cloud computing environment, *Computer & Geoscience*, 60: 109-116 (2012 Impact Factor: 1.834).

- **Guan, H.,** Li, J., Chapman, M., Ji, Z., and Deng, F., 2013. Integration of orthoimagery and lidar data for object-based urban feature mapping using random forests, *International Journal of Remote Sensing,* 34(14): 5166–5186 (2012 Impact Factor: 1.138).

- **Guan, H.,** Ji, Z., Zhong, L., Li, J., and Ren, Q.,2013. Partially supervised hierarchical classification for urban features from lidar data with aerial imagery, *International Journal of Remote Sensing*, 34 (1): 190-210 (2012 Impact Factor: 1.138).

- **Guan, H.,** Li, J., and Chapman, M., 2011, Urban thematic mapping by integrating lidar point cloud with colour imagery, *Geomatica*, 65(4): 375-385.

Refereed Conference Papers

- **Guan**, **H.,** Li, J., and Yu, Y., 2013. Rapid update of road surface databases using mobile LiDAR, *IEEE Proceedings on GiT4NDM*, Mississauga, Ontario, Canada, October 9-11, 2013.

- Li, J., Yu, Y., **Guan, H.,** and Wang, C., 2013. Automated detection of manhole covers using a mobile LiDAR system, *IEEE Proceedings on GiT4NDM*, Mississauga, Ontario, Canada, October 9-11, 2013.

- **Guan**, **H.,** Li, J., and Yu, Y., 2013. 3D urban mapping using a Trimble MX8 mobile laser scanning system: a validation study, *MMT 2013*, Tainan, Taiwan, May 1-3, 2013.

- Li, J., **Guan**, **H.,** and Yu, Y., 2013. Extraction of tree crowns from mobile laser scanning data using a marked point process model, *MMT 2013*, Tainan, Taiwan, May 1-3, 2013.

- Yu, Y., Li, J., and **Guan**, **H.,** 2013. Detection of road surface cracks from mobile laser scanning data, *MMT 2013*, Tainan, Taiwan, May 1-3, 2013.

- Xiang, Q., Li, J., Yang, B., and **Guan**, **H.,** 2013. Extraction of power lines from mobile laser scanning data, *MMT2013*, Tainan, Taiwan, May 1-3, 2013.

- **Guan**, **H.,** Yu, J., Li, J., and Luo, L., 2012. Random forests-based feature selection for land-use classification using lidar data and orthoimagery, *ISPRS Achieves*. Melbourne, Australia, Aug. 25 - Sept. 1, 2012.

- Yu, Y., Wang, C., Li, J., and **Guan**, **H.,** 2012. Terrestrial mobile laser scanning for urban infrastructure mapping: road marking extraction results, *ISPRS Achieves*. Melbourne, Australia, Aug. 25 - Sept. 1, 2012.

- Li, J., Li, G., Wang L., and **Guan**, **H.,** 2012. Terrestrial mobile laser scanning for 3D urban infrastructure mapping, *ISPRS Achieves*. Melbourne, Australia, Aug. 25 - Sept. 1, 2012.

- **Guan**, **H.,** Li, J., and Chapman, M., 2011. Support vector machine for urban land-use classification using lidar point clouds and aerial imagery, *International Symposium on LiDAR and RADAR mapping: Technologies & Applications*. Hohai University, Nanjing, China, May 26-29, 2011.